On the microstructure of active cellular processes

Martin Lenz

On the microstructure of active cellular processes

Thèse d'Habilitation à diriger les recherches
de l'Université Paris-Sud

présentée par
Martin Lenz

Soutenue le 19 juin 2015 devant le jury composé de:

Laurent Blanchoin	Rapporteur
Giuseppe Foffi	Président
Erwin Frey	Examinateur
Jean-François Joanny	Invité
Tom C. Lubensky	Rapporteur
Jacques Prost	Invité
Thomas A. Witten	Examinateur
Peter G. Wolynes	Rapporteur

Abstract

Eukaryotic cells use a multitude of protein machines to regulate their own structure. In this thesis, we study how the geometrical arrangement of these interacting microscopic active elements sculpt the cell's own internal microstructure and its membrane enclosure.

We first focus on the mechanisms generating actomyosin contractility, a crucial driver of cell motion and organization. We question the current position of highly organized, sarcomeric contractility as the only possible mechanism to drive contractility. We propose an alternative mechanism, and show that only it can account for the observed contractility of disordered actomyosin assemblies. It moreover yields qualitatively new effects in intracellular force transmission, including stress reversal and amplification, consistent with experimentally observations in fiber networks.

We next elucidate some of the mechanisms through which the cell deforms and cuts its own membrane, thus enabling exchanges with the extracellular medium as well as between its internal compartments. We find that the function of the proteins responsible for this remodeling is strongly influenced by the mechanics of the membrane, and use these effects to elucidate the modes of operation of proteins clathrin and dynamin, as well as of protein complex ESCRT-III.

To Claire, Diane and Eve

Contents

Chapter 1

Foreword

This thesis summarizes my contributions to my two main research interests over the period 2010-2014, namely active stress generation in the cytoskeleton and protein-membrane interactions. In both cases, my approach has focused on a mesoscopic scale that can be described without a perfect knowledge of molecular details, but at which the geometrical structure of subcellular constructs still yields crucial insights into biological processes.

My interest in the first topic, described in Chapter 2, has revolved around understanding how the large-scale behavior of actomyosin emerges from its microscopic dynamics. While this behavior has been well characterized experimentally, we demonstrate that in some systems the microscopic and macroscopic behaviors of actomyosin are seemingly incompatible for symmetry reasons. New mechanisms thus need to be invoked to connect them, and we make significant progress towards characterizing them theoretically. In Chapter 3, we turn to the nanometer-scale physical mechanisms through which specialized proteins deform and remodel the cell membrane. Unlike in the actomyosin case, the microscopic underpinnings of these processes are not well understood. In this setting, theory is a powerful way to connect the dots between disparate experimental results, validating hypothetical mechanisms by quantitatively predicting the results of an experiment from data acquired in unrelated ones. Chapter 4 then presents my research plans, to be carried out in my two-year-old research group in Orsay.

The theoretical work presented here is deeply rooted in experimental observations, and I have been extremely fortunate to work with the groups of Margaret Gardel (University of Chicago) and Aurélien Roux (University of Geneva), with whom I have had a very fruitful back-and-forth between theory and experiments. The presentation of this thesis reflects the format of these exchanges, and blends general theoretical results, more involved modeling and experimental tests. While I believe that this presentation is the most efficient to convey our ideas, it might be to the detriment of identifying contributions—to clarify this point, I performed none of the experiments, while virtually all theoretical work was conducted either by me or by students under my direct supervision. This thesis is selective in its presentation, focusing on simple theoretical ideas and scaling reasonings, and covers only two of my research interests. The reader interested in more rigorous theoretical, experimental or bibliographical discussions as well as in other projects will find a list of original articles as well as hyperlinks in Appendix A.

Chapter 2

Contractility in disordered actomyosin

The structure and motion of living cells is largely controlled by the continuous remodeling of their cytoskeleton, which crucially involves the contractility of networks of actin filaments (F-actin) and myosin molecular motors. How macroscopic motion emerges from the protein-scale interactions between these components was first understood in the context of striated muscle [1]. There, individual myosins are assembled into so-called "thick filaments", bottlebrush-shaped clusters of myosin capable of binding several actin filaments and of sliding along them for long distances. The motion of these assemblies of motors is powered by the hydrolysis of adenosine triphosphate (ATP) into adenosine diphosphate (ADP); for brevity, we refer to them simply as "motors" in the following. In striated muscle, F-actin and motors are strongly organized into a periodic array of so-called sarcomeres, contractile units where the sliding action of the motors is harnessed to produce contraction through F-actin's geometrical arrangement [Fig. 2.1(a)].

However, in many biological situations contractile F-actin and myosin assemblies—be they one-dimensional bundles or two- or three-dimensional networks—lack the organization found in sarcomeres [2, 3, 4, 5, 6, 7, 8] (Fig. 2.2). While the biochemical processes inducing the relative motion of the motors and filaments are similar to the ones involved in striated muscle, here the geometrical mechanisms used to convert this relative motion into contraction in the absence of organization are less clear. Indeed, the filaments and motors do not have an intrinsic propensity towards contraction, and can *a priori* yield extension just as easily. Figure 2.1(b) illustrates this property in a simple one-dimensional example. Most theoretical models of disordered actomyosin contractility circumvent this question by assuming from the onset that motors either induce an average contractile stress in the actomyosin medium [9] or, in more detailed descriptions, that they give rise to localized contractile force dipoles [10]. These studies then typically move on to consider the macroscopic consequences of such mesoscopic behaviors. In the work presented in this chapter, we adopt a different focus and ask how the contractility emerges from the networks' microscopic components in the first place.

We first discuss this question in one-dimensional actomyosin assemblies, *i.e.*, actomyosin bundles. In these systems, we present *in vitro* experiments demonstrating that sarcomere-like organization is not necessary

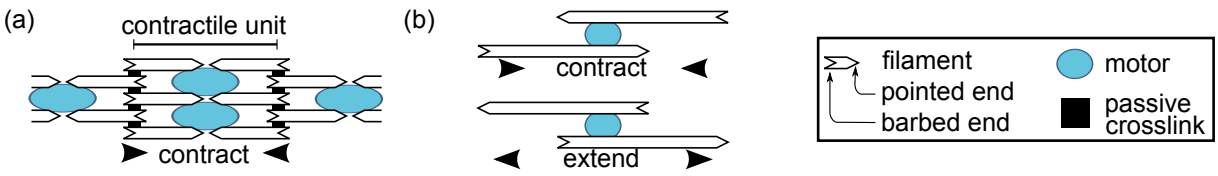

Figure 2.1: Geometrical foundations of contractility. Motors bound to filaments slide towards their "barbed ends", as for myosin II thick filaments. (a) In striated muscle, motors are localized close to the filaments' pointed ends. When activated, every motor pulls in the neighboring filaments and thus induces local contraction. (b) If filament polarities are not carefully selected, striated muscle-like locally contractile configurations (*top*) are just as likely as extensile ones (*bottom*), and the overall behavior of the actomyosin assembly is unclear.

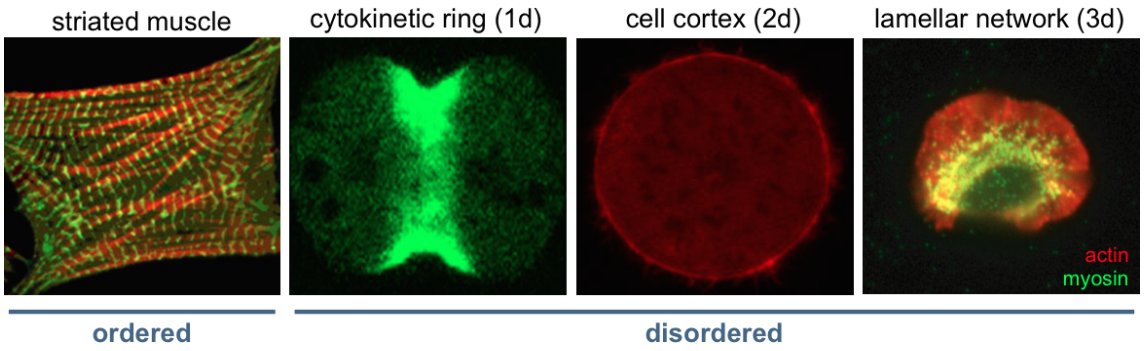

Figure 2.2: Four examples of *in vivo* contractile actomyosin, showing the contrast between the very organized striated muscle and more disordered structures in one, two and three dimensions. Images respectively taken from the Lappalainen lab website, and Refs. [11, 12, 13].

for contraction (Sec. 2.1), and thus that the symmetry between contraction and extension illustrated in Fig. 2.1(b) is spontaneously broken. Because geometry in one dimension is very simple, there are strong geometrical constraints on the type of mechanisms that can lead to such symmetry-breaking, which we discuss in Sec. 2.2. Combining these theoretical constraints with further experiments, we then show that F-actin buckling under longitudinal compression enables contraction by favoring local filament collapse in the absence of sarcomere-like organization (Sec. 2.3). This mechanism significantly differs from the canonical sarcomeric contraction, resulting in qualitatively different predictions for the contraction force and velocity. As discussed in Sec. 2.4, experiments validate our model to the exclusion of the sarcomeric mechanism, offering decisive evidence for non-sarcomeric contraction in disordered actomyosin bundles.

We next study the contractility of the large range of two- and three-dimensional contractile actomyosin networks found *in vivo*. Their physics is more complex than that of bundles, and warrants studying local and nonlocal effects separately. Accordingly, we first focus on the physics of the immediate surroundings of a motor in Sec. 2.5. We present the first comprehensive comparison of contractility-inducing mechanisms in disordered cytoskeletal networks, and find that filament deformation plays a crucial role in most relevant regimes. We then ask how these local forces propagate to larger scales, and introduce general theorems about this force transmission in linear viscoelastic networks in Sec. 2.6. Finally, Sec. 2.7 describes ongoing work about force transmission in nonlinear two- and three-dimensional elastic networks, suggesting a surprisingly strong tendency of filamentous actin networks to generate strong large-scale contraction from comparatively weak locally contractile *and* extensile forces, yielding unprecedented insights into the robustness of actomyosin contractility.

2.1 Ordering is not required for bundle contraction

While many intracellular actomyosin structures generate contraction in the absence of *apparent* ordering, our knowledge of their microscopic organization is far from perfect. As a result, we are not able to determine with certainty whether the local configurations represented in Fig. 2.1(b) are indeed present in equal quantities in these systems, or if their microscopic structure favors contractile over extensile configurations as in sarcomeres. In order to establish whether contractility is indeed possible in fully disordered actomyosin systems, we develop a novel *in vitro* reconstituted assay, where preformed biotinylated actin filaments and ADP-associated (*i.e.*, inactive) smooth muscle myosin thick filaments are left to aggregate and associate with streptavidin-coated polystyrene beads bound to the surface of a deformable hydrogel. This aggregation process, illustrated in Fig. 2.3, results in a two-dimensional network of long actomyosin bundles. In the absence of motor activity, the motors are not expected to preferentially associate with either the barbed or pointed end of the actin filaments, and therefore we do not expect the bundles to display any polarity ordering. In other words, filaments within the bundle do not preferentially choose one polarity over the other. No crosslinks are introduced in the system.

To determine whether such disordered actomyosin bundles are able to contract, we next flow ATP into the

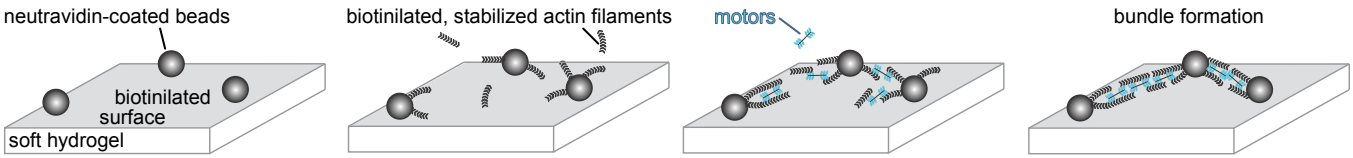

Figure 2.3: Assembly of polarity-disordered actomyosin bundles on a polyacrylamide gel substrate performed in the following four steps. 1) Neutravidin beads are bound to a biotinylated-BSA-coated polyacrylamide gel surface. 2) Biotinylated F-actin binds to the beads, forming F-actin asters. 3) Myosin thick filaments are introduced in the absence of ATP. 4) After $\simeq 30\,\mathrm{min}$ incubation, actomyosin bundles form near the surface and span between beads. Free myosin filaments in solution are washed out, followed by perfusion of 1 mM ATP, which induces motor activity and allows bundles to contract

experimental chamber, which activates the sliding motion of individual motors. As a result, the initially floppy bundles all quickly become taut, evidencing contraction. In many cases, contractile stresses induce the rupture of the bundles, which is followed by a retraction to $\simeq$ 60-80% of their initial length over a few tens of seconds. The contraction speed is found to be proportional to the length of the bundles, a phenomenon known as "telescopic contraction". Its occurrence demonstrates that contraction occurs throughout the bundles, as opposed to constituting an end-effect possibly induced by the specifics of their attachment to the beads. We take advantage of cases where rupture does not occur to measure the contractile force exerted by a single bundle. To this end, we analyze the deformation of the soft substrate onto which the beads are grafted and find that it amounts to several hundreds of picoNewtons. As a single myosin head may generate forces of the order of a picoNewton, this is evidence that despite their lack of polarity ordering these bundles are able to make hundreds of myosin heads work in concert to systematically generate contractile force. This is in apparent contradiction with the expected symmetry between contraction and extension illustrated in Fig. 2.1(b).

Reference: *Reconstitution of Contractile Actomyosin Bundles.*
Todd Thoresen, **Martin Lenz**, Margaret L. Gardel, *Biophys. J.* **100**, 2698 (2011)

2.2 Disordered bundle contraction requires actin nonlinearity

To understand under which condition the contraction/extension symmetry can be broken, we develop a semi-microscopic model of contractile actomyosin networks. In the model, polar filaments aligned along a single direction are linked together by undeformable (but not necessarily point-like) motors at discrete attachment points. Filament "sections" comprised between two attachment point may deform longitudinally according to an unprescribed force-extension relation, which may be a function of their resting length. The attachment points are able to slide along the filaments according to an also unprescribed, motor-dependent, possibly nonlinear force-velocity relationship. This very general mathematical description can accommodate the presence of actin crosslinkers, which may simply be described as motors whose velocity is zero irrespective of the force applied on them. We assume force balance throughout the system, although the addition of viscous drag forces (which are negligible in practice) does not modify our conclusions. No specific assumption is made about either the geometry or the topology of the bundle.

In a first approach to our question, we investigate whether such a bundle may display telescopic contraction in a situation where all its motors are identical, as appears to be the case in the above-described experiments. More precisely, we investigate a bundle where all motors have the same unloaded velocity. Denoting this velocity by v_0, we prove that in such bundles all motors are motionless with respect to one another. Filaments whose pointed end is directed to the right on the diagram of Fig. 2.4(a) move to the right with velocity $+v_0$, while left-pointing filaments move to the left with $-v_0$. In such a pattern of motion, all motors slide at their preferred (unloaded) velocity, and there is no filament tension build-up within the network, implying that the filament force-extension relationships are irrelevant. Moreover, we note that the velocities of the bundle extremities must lie in the interval $[-v_0, v_0]$, and therefore telescopic contraction cannot take place in such a setting. As telescopic contraction is indeed observed in the above-

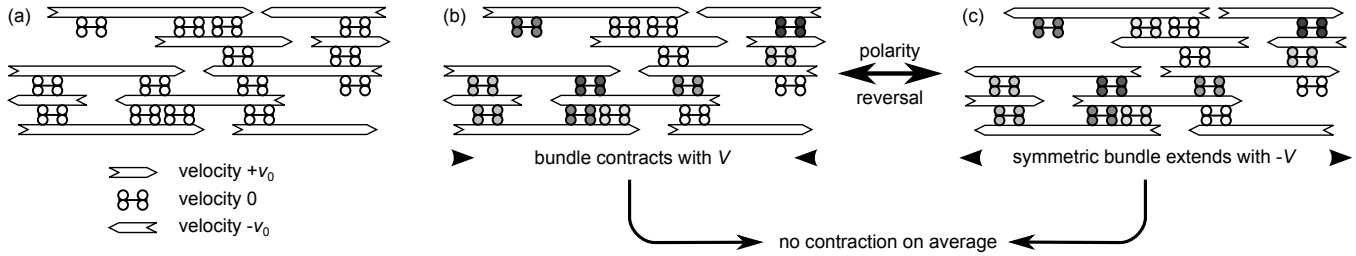

Figure 2.4: Theoretical investigations into the requirements for actomyosin bundle contraction though general symmetry arguments. (a) Identical motors generate a pattern of motion whereby filaments are transported at a constant velocity according to their polarity. Such a motion is incompatible with telescopic contraction. (b) A bundle with nonidentical motors (*shades of grey*) may display some amount of contractility, denoted here by V. (c) If the filaments are stiff, the polarity-reversed image of such a motor has an equal and opposite contraction velocity $-V$. In cases where the two configurations are equally likely, no contractility can occur on average.

described experiments, we conclude that even though the filaments of Sec. 2.1 are all bound by thick filaments of smooth muscle myosin prepared under identical experimental conditions, there must exist some variability in their unloaded velocities. This is not unreasonable from an experimental standpoint, as electron microscopy reveals that the fluctuations in the number of myosin head per thick filament are comparable to its mean. Moreover, despite experimental efforts to the contrary, it is likely that some of the myosin heads my be inactive or that their phosphorylation state might fluctuate.

Now considering a situation where motors do not have identical unloaded velocities, as is the case for *in vivo* bundles comprising crosslinks, we find that individual bundles may display telescopic contractility depending on their specific geometry and motor attachment topology. The contractile sarcomeric structure shown in Fig. 2.1 is one such example, which relies on a strong form of polarity organization. Indeed, in this structure crosslinks ("immobile motors") are localized at the filament barbed ends, while functional motors are systematically located at their pointed ends. Were the polarities of the filaments to be reversed, as might happen in some regions of a polarity disordered bundle, these structures would become extensile.

More generally, we show that the two tendencies compensate on average for a collection of polarity-disordered bundles where filaments behave as rigid rods, reflecting the symmetry of Fig. 2.1(b). To prove this statement, we consider a generic filament-motor bundle as illustrated in Fig. 2.4(b). As the motors slide along the filaments, locally ordered regions of this bundle may either contract or extend. Moreover, the stresses resulting from the conflict between the velocities prescribed by different motors might deform the filaments and induce local compression or stretching in the bundle. As a result, the bundle of Fig. 2.4(b) has a non-vanishing contraction velocity, which we denote by V. We next consider the bundle of Fig. 2.4(c), which is rigorously identical to the previous one, except for the fact that the polarities of its filaments are reversed. If the filaments within this bundle behave as rigid rods, they can be described using linear elasticity. In such a situation, reversing the polarity of the filaments is equivalent to reversing all filament tensions and all velocities in the system. As a result, the polarity-reversed bundle contracts with velocity $-V$, implying extension in cases where $V > 0$. Since in a polarity reversal-invariant ensemble of bundles the two configurations of Figs. 2.4(b) and (c) are equally likely, we conclude that linearly elastic, polarity reversal-invariant bundles do not contract on average.

In summary, actomyosin contractility requires:

1. Nonidentical motors

   and

2. *Either*

   (a) Polarity organization in the initial condition

   or

   (b) Nonlinear filament elasticity

Interestingly, this statement is valid irrespective of the bundle's internal geometry and topology, as well as of the (possibly nonlinear) form of the motor force-velocity relationships. Moreover, we note that assumption 2(a) only regards the bundle's initial state. Indeed, our detailed proof shows that a polarity organization emerging from an initially disordered ensemble of bundles as a result of their internal dynamics is not sufficient to generate contraction. In conclusion, our reasoning allows for two possible modes of actomyosin contractility:

- 1+2(a): This is the well-known sarcomeric contraction mode, where nonidentical motors (in practice, a combination of crosslinks and active motors) generate contraction.
- 1+2(b): This constitutes a new hypothetical mode of contraction, where nonidentical motors induce stresses within the filaments. While compressive and extensile stresses are present in equivalent amounts, individual filaments respond nonlinearly to these stresses, for instance collapsing under compression more than they stretch under extension. In such an example, the overall response of the bundle is dominated by filament collapse, leading to an overall shortening of the bundle, *i.e.*, contractile behavior.

Thus within the general set of assumptions used in our model, disordered bundles can only contract according to mechanism 1+2(b). Note that the model considered here does not consider the possibility for motors to detach from the filaments and then reattach elsewhere. While such events are negligibly rare in the experiments described in Sec. 2.1, they might play an important role in other systems, and are further discussed in the research project of chapter 4.

Reference: *Requirements for contractility in disordered cytoskeletal bundles.*
Martin Lenz, Margaret L. Gardel, Aaron R. Dinner, *New J. Phys.* **14**, 033037 (2012)

2.3 Actin buckling acts as a contractility-inducing nonlinearity

Using the reasonings of the previous section as a guide to understand disordered bundle contraction as observed in Sec. 2.1, we hypothesize that the nonlinear actin response in these experiments stems from the well-characterized phenomenon of actin buckling. As a consequence of buckling, an inextensible filament resists extension, while it collapses under sufficient longitudinal compression, much like a piece of rope. The resulting contractility mechanism is schematized in a simple setting in Fig. 2.5(a), which suggests that buckling typically occurs over distances of the order of the spacing between two motors.

As the experiments of Sec. 2.1 use motors that are too closely packed for the resulting buckles to be visible under our imaging conditions, we reason that buckles should be observable under conditions where motors are less dense. By measuring the actin and myosin densities inside the bundle, we establish experimentally that varying the myosin concentration between $1\,\mu$M and $0.1\,\mu$M allows us to tune the average distance ℓ_0 between myosin thick filaments along individual F-actin between 390 nm to $5.3\,\mu$m. For ℓ_0 equal to 540 nm or larger, we observe visible actin buckles, whose appearance is moreover very well synchronized with both ATP injection and bundle contraction [Fig. 2.5(b)]. Lowering the myosin concentration further, however, abrogates contraction as shown in Fig. 2.5(c), even though the myosin concentration is still well above the minimal concentration required to maintain bundle integrity. This observation is somewhat surprising, as we would expect that for low myosin concentration the filament sections separating two motors are long and therefore easy to buckle, implying strong contraction. Conversely, this reasoning suggests that for high myosin concentrations, bundle crosslinking by myosin becomes so extensive that buckling should be suppressed.

To account for this discrepancy regarding the qualitative effect of motor spacing on concentration, we add one important element to our bundle contraction picture, namely that motors intermittently detach from the filaments, thus allowing local stress relaxation. Our two other main assumptions are that motors have a dispersion in their unloaded velocities as required by the reasoning of Sec. 2.2, and that a section of filament between two motors buckles above a certain threshold force F_B. We thus consider a bundle of

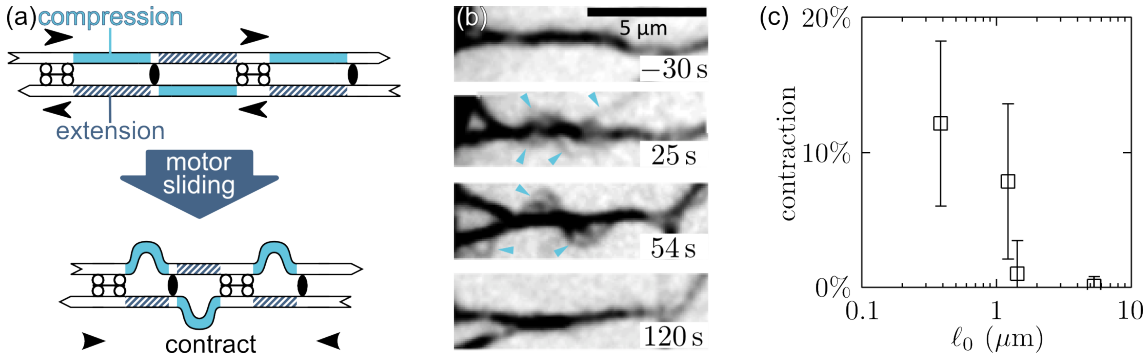

Figure 2.5: Buckling in nonsarcomeric contractile actomyosin bundles. (a) In our hypothesized mechanism, the simultaneous presence of motors and crosslinks (or fast and slow motors) generically induces compressive (*light blue*) and extensile (*hatched dark blue*) stresses in filaments. Buckling of the compressed filaments leads to an overall shortening of the bundle. (b) Time-lapse images of fluorescent actin (inverted contrast) showing F-actin buckling (*arrowheads*) following the addition of 1 mM ATP at $t = 0$ s. (c) Bundle contraction as a function of the inter-motor distance ℓ_0, estimated from quantitative myosin fluorescence. Bars indicate standard deviation ($n \geqslant 25$).

weakly deformed filaments and ask whether the forces developing within it are sufficient to induce buckling [Fig. 2.6(a)].

We focus on a single filament of length ℓ_f and approximate its surroundings by an effective medium composed of evenly spaced point-like motors separated by a distance $\ell_0 \ll \ell_f$ [Fig. 2.6(b)]. This divides the filament into discrete sections, which we label by $i = 0, \ldots, \ell_f/\ell_0$. We take into account the possibility that the filaments are not straight, but bend away from the x-axis, implying that the contour length L_i of filament section i can be larger than ℓ_0. Defining f_i as the tension of filament section i ($f_i < 0$ for a compressed filament section), we expand its force-extension relationship for small deformations:

$$L_i = L_i(f_i = 0) - c f_i, \tag{2.1}$$

where $c > 0$ is the filament compliance. We refer to the motor flanked by filament sections $i-1$ and i as "motor i", and describe its operation by the simplified force-velocity relationship

$$f_{i-1} - f_i = F_i - \chi v_i. \tag{2.2}$$

Here v_i denotes the local velocity of the filament at the location of motor i and $\chi > 0$ is the motor susceptibility. Eqs. (2.1) and (2.2) yield a local relaxation time scale $\tau_r = \chi c/2$. The time-independent stall force of motor i is denoted by F_i in Eq. (2.2), and is drawn from a random distribution satisfying

$$\overline{F_i} = F_S \quad \text{and} \quad \overline{F_i F_j} - \overline{F_i}\,\overline{F_j} = \delta F_S^2 \delta_{ij}, \tag{2.3}$$

where bars denote averages over the motor distribution. As a result, different motors have different unloaded velocities F_i/χ, as required for contraction (Sec. 2.2). Owing to the conservation of filament mass:

$$\frac{\mathrm{d}L_i}{\mathrm{d}t} = v_i - v_{i+1}. \tag{2.4}$$

Finally, a motor bound to several filaments as in Fig. 2.6(a) can transiently detach from one while still holding onto the others. We thus let each motor i randomly detach from the filament with a constant rate $1/\tau_d$. Following detachment, local filament stresses relax instantaneously, yielding $f_i = f_{i-1} = (f_i + f_{i-1})/2$. The motor then reattaches after a time much shorter than τ_r and τ_d. Since a motor in a dense bundle is typically close to several filaments, the probability that it detaches from all filaments at the same time and leaves the bundle is negligible. We denote by $\langle \ldots \rangle$ the average over the Poisson process of motor detachment.

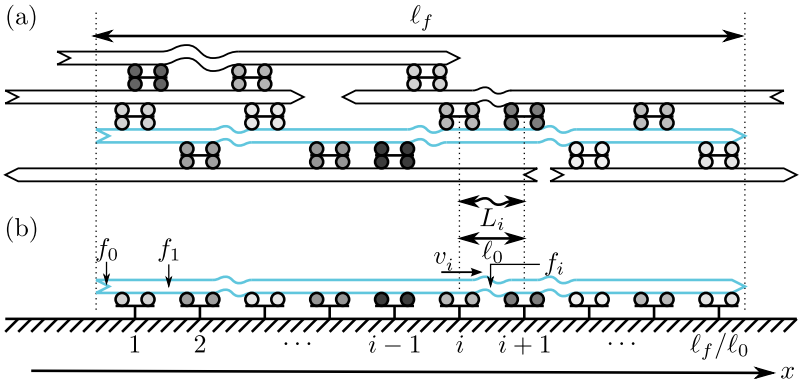

Figure 2.6: Stress build-up in bundles with non-identical motors. (a) In a bundle with motors having non-identical velocities (*shades of grey*), filaments of length $\ell_f \gg \ell_0$ are subjected to random motor forces at points $\approx \ell_0$ apart distributed throughout their length. (b) Prior to contraction, the environment of a filament of interest (*blue*) can be approximated by a collection of evenly spaced motors.

We obtain the space and time evolution of the filament tension $f(x,t)$ in the continuum limit $i \to x/\ell_0$ by combining Eqs. (2.1-2.4) and averaging over motor detachment:

$$\partial_t \langle f \rangle - D\partial_x^2 \langle f \rangle = (\ell_0/2\tau_r)\partial_x F, \tag{2.5}$$

where $D = \ell_0^2(\tau_r^{-1} + \tau_d^{-1})/2$. The right-hand-side of Eq. (2.5) involves the spatial gradient of the stall force $F(x)$, reflecting the fact that non-identical motors lead to force build-up. This effect competes with the relaxation of filament forces through motor detachment, which enters through the diffusion term $D\partial_x^2\langle f \rangle$.

An initially relaxed filament $[f(x,t=0)=0]$ experiences a vanishing average force $\overline{\langle f \rangle}(x,t) = 0$ throughout its dynamics. To quantify the magnitude of the motor-induced stress, we use Eqs. (2.1-2.4) and average over motor detachment to calculate the rms filament force in the continuum limit:

$$\left(\overline{\langle f^2 \rangle}\right)^{1/2} = f_\infty \left\{ \sum_{n \in \mathbb{Z}^*} \left[\frac{3}{n^2\pi^2} \left(1 - e^{-\frac{n^2 D t}{(2\pi\ell_f)^2}} \right)^2 \right] \right\}^{1/2}. \tag{2.6}$$

This force increases monotonically from zero at $t=0$ to $f_\infty = (\ell_f/12\ell_0)^{1/2} \times \delta F_S/(1+\tau_r/\tau_d)$ at $t=\infty$ [Fig. 2.7(a-b)]. We next estimate the dependence of the ratio τ_r/τ_d on the experimentally accessible parameter ℓ_0. A Worm-Like Chain model for filament elasticity yields $c \approx \ell_0^4/k_BT\ell_p^2$, where ℓ_p is the filament persistence length, and we approximate $\chi \approx F_S/v$, where v is a characteristic motor velocity. This implies $\tau_r/\tau_d \approx (\ell_0/\ell_0^*)^4$, with $\ell_0^* = (k_BT\ell_p^2 v\tau_d/F_S)^{1/4}$. We can thus distinguish two regimes for the steady-state force f_∞ [Fig. 2.7(a)]. For $\ell_0 \ll \ell_0^*$, detachment events are rare compared to the time τ_r needed for the force to recover from such an event, and f_∞ is not affected by them. For $\ell_0 \gg \ell_0^*$, f_∞ quickly decreases with increasing ℓ_0 as detachment becomes much faster than recovery.

Up to a prefactor of order one, contraction proceeds as in Fig. 2.5(a) if $f_\infty > F_B \approx k_BT\ell_p/\ell_0^2$ [14]. Comparing f_∞ to F_B as in Fig. 2.7(a), we find a threshold stiffness above which buckling cannot occur (as exampled by the *blue line*). Reasonable values for our actomyosin system are $\ell_p \simeq 10\,\mu$m, $v \simeq 200\,\text{nm}\cdot\text{s}^{-1}$, $\delta F_S \approx F_S \simeq 1\,$pN and $\tau_d \simeq 200\,$ms based on the typical time scales involved in the myosin mechanochemical cycle. Since $\tau_r \gtrsim \tau_d$ in our experiments and detached motors reattach in $\approx 1\,$ms [15], our previous assumption of fast motor reattachment is justified. These values put us in the soft filament regime defined by $\ell_p \ll \delta F_S^4 L_f^2 (v\tau_d)^{3/2}/k_BT^{5/2}F_S^{3/2} \simeq 20\,$cm (*red line*). In this regime, the lines representing F_B and f_∞ intersect at

$$\ell_0^- = (k_BT\ell_p/\delta F_S \ell_f^{1/2})^{2/3} \simeq 70\,\text{nm}, \tag{2.7a}$$

$$\ell_0^+ = (\ell_f^{1/2} v\tau_d \ell_p \delta F_S/F_S)^{2/5} \simeq 1\,\mu\text{m}, \tag{2.7b}$$

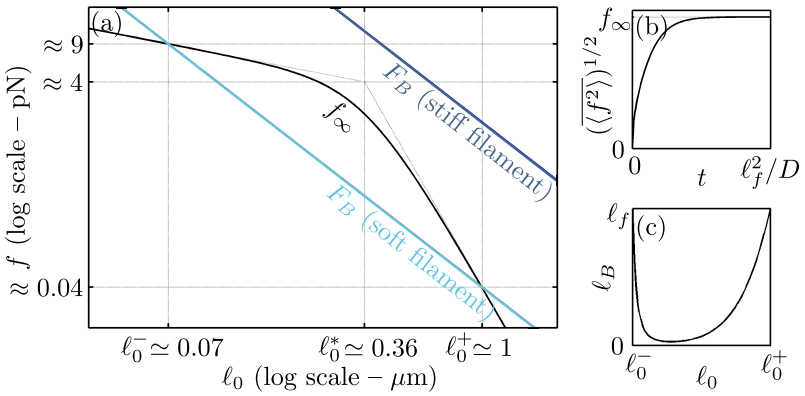

Figure 2.7: Model predictions for filament force build-up. (a) *Black line*: Steady-state filament force f_∞ as a function of motor spacing ℓ_0 [Eq. (2.6)]. For $\ell_0 \ll \ell_0^*$ and $\ell_0 \gg \ell_0^*$, $f_\infty \propto \ell_0^{-1/2}$ and $\ell_0^{-9/2}$, respectively. *Colored lines*: buckling force $F_B \propto \ell_0^{-2}$. (b) Typical filament force $(\overline{\langle f^2 \rangle})^{1/2}$ as a function of time [Eq. (2.6)]. (c) Contractile unit size ℓ_B as a function of ℓ_0 as in Eq. (2.8) ($\ell_f \simeq 5\,\mu$m).

meaning that buckling and contraction occur for $\ell_0^- < \ell_0 < \ell_0^+$. This range reflects the fact that strong cross-linking ($\ell_0 < \ell_0^-$) suppresses buckling while sparse motors ($\ell_0 > \ell_0^+$) are undermined by stochastic detachment. While the regime $\ell_0 \simeq \ell_0^-$ is not accessible experimentally, the predicted value for ℓ_0^+ is strikingly similar to the motor spacing at which the breakdown of contraction is observed in Fig. 2.5(c) ($1.3\,\mu$m), suggesting that the proposed mechanism is a good description of our experiments.

To characterize the contractile units resulting from this mechanism when $\ell_0^- < \ell_0 < \ell_0^+$, we turn to the transient regime leading up to filament buckling. The filament force profile as a function of x is initially flat, and subsequently coarsens into a random walk for $t = +\infty$. According to Eq. (2.5), this coarsening occurs diffusively with diffusion coefficient D. The typical filament forces at time $t \ll \ell_f^2/D$ are thus of order $f_\infty(\sqrt{Dt}/\ell_f)^{1/2}$. We denote the time that this force reaches the buckling threshold F_B by t_B, following which contraction proceeds as in Fig. 2.5(a) and the coarsening dynamics is interrupted. The distance between buckles at t_B thus yields the contractile unit size

$$\ell_B \approx \sqrt{Dt_B} \approx \frac{\ell_p^2}{\ell_0^3}\left(\frac{k_BT}{\delta F_S}\right)^2\left(1+\frac{\tau_r}{\tau_d}\right)^2. \tag{2.8}$$

As illustrated in Fig. 2.7(c), ℓ_B is typically in the micrometer range, in agreement with the observations of Fig. 2.5(c).

The order-of-magnitude agreement between theory and experiments with respect to the size of contractile units and the critical myosin concentration required for contraction suggests that our current analysis offers a good description of the onset of bundle contractility. Our conclusions are robust to inclusion of features such as inhomogeneous motor spacings ℓ_0 and force dependence of the motor detachment rate. Our mechanism is a general one and applies to any one-dimensional system of polar filaments and motors. It is also generalizable to any situation where filaments respond asymmetrically to compression and extension, even if buckling is not present. Addition of passive cross-linkers, which are formally equivalent to immobile motors, would reinforce a dispersion of motor velocities and promote contraction.

Reference: *Contractile units in disordered actomyosin bundles arise from F-actin buckling.*
Martin Lenz, Todd Thoresen, Margaret L. Gardel, Aaron R. Dinner, *Phys. Rev. Lett.* **108**, 238107 (2012)

2.4 Data show buckling-induced, not sarcomeric, contractility

To decisively discriminate between buckling-induced and sarcomeric contraction in disordered bundles, we next investigate the dependence of the maximum bundle contraction force and speed on the size of the

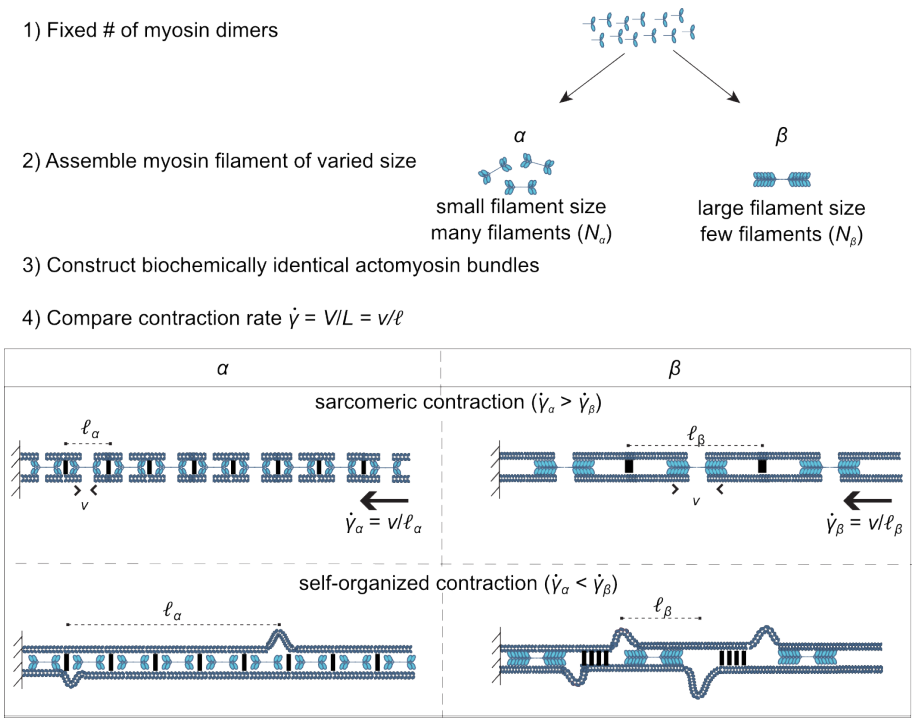

Figure 2.8: Contrasting predictions of the sarcomeric and buckling-induced contraction models regarding the bundle contraction rate.

number of myosin heads per motor. Here we report our result on the speed, which is most significant. In both sarcomeric and buckling-induced contraction, the rate of contraction is governed by the number of contractile units per length and the rate of contraction of each unit (Fig. 2.8). In sarcomeres, these two parameters are determined by the sarcomere size and the force-velocity relationship of skeletal myosin II motors. In disordered bundles, we expect more loosely defined contractile units of length ℓ_B to self-organize as described in Sec. 2.3.

To illustrate the contrasting regulation of sarcomere-like and buckling-induced contractility, consider two biochemically identical bundles consisting of the same number of myosin II motors and actin filaments with identical lengths and orientations (Fig. 2.8). The only distinguishing feature between the two bundles is that the myosin II motors are constructed into filaments of different sizes. In the first bundle (bundle α), the myosin filaments are small, but numerous, whereas bundle β has large, but sparse myosin filaments. Which of these bundles contracts at a faster rate? In a sarcomeric organization, the spacing of myosin II filaments determines the sarcomere size. As there are more contractile units per bundle length in bundle α, it will contract faster according to this mechanism. However, in the buckling-induced contractility model, internal stresses are needed to drive filament deformation, favoring the large motors of bundle β. Moreover, motor-mediated dense crosslinking prevents filament deformation in bundle α. Thus, according to the buckling-induced contractility model, the stronger internal forces but weaker crosslinking of bundle β promote contractile unit formation and thus faster contraction. Performing this experiment on the disordered actomyosin bundles described in Fig. 2.1, we find that the bundle contraction velocity increases with thick filament size, consistent with the buckling-induced contractility model and not with sarcomeric contraction (Fig. 2.8).

Reference: *Thick filament length and isoform composition determine properties of self-organized contractile units in actomyosin bundles.*
Todd Thoresen, **Martin Lenz**, Margaret L. Gardel, *Biophys. J.* **104**, 655 (2013)

2.5 Comparing local network contraction mechanisms

While disordered actomyosin contractility in one-dimensional bundles appears to be well described by our buckling mechanism, the situation in two- and three-dimensional actomyosin networks is more complex. There too, contraction arises in random-polarity, disordered *in vitro* networks [16, 17, 18]. From a theoretical standpoint, however, geometry in two or three dimensions is considerably richer than in one. As a result, several mechanisms can *a priori* give rise to contraction, and symmetry considerations are less easily exploited than in bundles. Accordingly, a range of mechanisms for the emergence of actomyosin contraction have previously been invoked in different levels of detail, ranging from cartoon pictures [10, 19] to more quantitative numerical [20] and analytical [21] approaches. However, there is no consensus regarding their relative roles in either *in vivo* or *in vitro* actomyosin contractility. Here we present the first comprehensive comparison of contractility-inducing mechanisms in disordered cytoskeletal networks.

The first part of this work consists in applying similar symmetry considerations to those of Sec. 2.2 in a two- or three-dimensional geometry. Similar to the one-dimensional situation studied there, each motor-filament configuration exerts either contractile or extensile forces on its surroundings. However, these opposing tendencies compensate and they are neither contractile nor extensile *on average* if the following assumptions are all realized simultaneously:

1. The motor stall force does not depend on its position
2. The motor is point-like
3. The motor is undeformable
4. Filaments behave as rigid rods.

Thus a model respecting these assumptions cannot reproduce the contractility observed in disordered actomyosin networks [16, 17, 22, 23], implying that it represents an oversimplification. As a result, one or several of the assumptions listed above must be violated in actual actomyosin systems. We successively relax each of these assumptions to systematically review all essential contraction mechanisms. We then predict and compare the magnitude of the associated contractile forces. Specifically, for each mechanism we consider a motor attached to two filaments crosslinked to a rigid external medium through four crosslinks [Fig. 2.9(a)], and compute the average local force dipole

$$D = \sum_i \boldsymbol{r}_i \cdot \boldsymbol{f}_i. \tag{2.9}$$

Here i indexes the four crosslinks. The position vector of a crosslink is denoted as $\boldsymbol{r}_i$ and $\boldsymbol{f}_i$ is the force exerted on it by filament i. A negative (positive) D denotes a contractile (extensile) system.

The first mechanism considered here consists in the violation of condition 1. above, and is reminiscent of early models of non-sarcomeric actomyosin bundles [24, 25] and networks [21]. These models propose that motors stop upon reaching the filament barbed ends, staying there for some time before eventually detaching. Although experimental evidence for this behavior in actomyosin is lacking, the resulting accumulation of immobile motors at the filament barbed ends would generate sarcomere-like crosslinking [Fig. 2.1(a)] and thus favor contraction. We compute the corresponding force dipole, but find it to be small compared to those studied below. Thus here we do not discuss this mechanism further.

The remaining three mechanisms are associated with violations of conditions 2., 3. and 4., respectively. They generate non-negligible local contractile forces through a common principle, which we illustrate for a simple symmetrical two-filament system in Fig. 2.9(b-c). This picture assumes that the motor is able to move away from the center of this system by a distance x—we defer the discussion of the specific mechanisms behind this motion for now. To understand how this leads to contraction, we draw an analogy between the motor and the slider of a zipper [Fig. 2.9(b)]. Assimilating the motor's propensity to slide along the filaments to a closing force applied on the zipper tab, we see that the motor pulls the filament barbed ends together as it progresses, just like the two sides of the zipper chain are pulled together as the zipper closes. This induces a predominantly contractile force dipole.

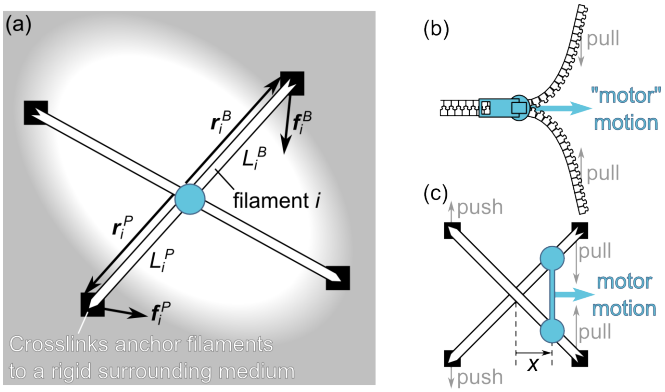

Figure 2.9: Principles of local force transmission in actomyosin networks. (a) Simplified one-motor, two-filament model. In this figure and the next, filament extremities may or may not be crosslinked to the surrounding medium. Even though this is not represented here, crosslinked filaments extend beyond the crosslinks and further into this medium and thus cannot freely rotate around these crosslinks. Thus, the barbed and pointed arrow ends on this schematic merely indicate filament polarity; the actual barbed and pointed ends of cross-linked filaments are typically further away inside the surrounding medium. (b) The contractility induced by a motor that is closer to the barbed than the pointed ends is analogous to the closing force (*thin gray arrows*) of a zipper when its slider is being slid shut (*thick cyan arrow*). (c) In practice, the zipperlike pulling forces exerted at the barbed end cross-links are partially compensated by pointed end pushing forces.

Importantly, the zipper effect induces contraction only if the motor is displaced from the intersection of the filaments. Indeed, while the motor pulls on the filaments' barbed end crosslinks, it also pushes out on the pointed end crosslinks as shown on Fig. 2.9(c). These two effects compensate exactly for a centered motor $x = 0$, suggesting that for small x, D is generically proportional to x. As D has units of energy, dimensional analysis suggests that it will also be proportional to f, the typical force exerted by the motor. We thus expect zipper-like contractility to scale as

$$D \approx -fx. \tag{2.10}$$

Let us now enumerate the three mechanisms allowing the motor to move away from the intersection of the filaments and towards their barbed ends. These mechanisms are illustrated in Fig. 2.10. above. Here we present scaling arguments to understand the magnitude of the associated force dipoles.

- A motor that has a finite size L_m moves away from the filament intersection by a quantity of order L_m, yielding

$$D_{\text{finite size}} \approx -f_s L_m, \tag{2.11}$$

  where f_s is the motor stall force.

- A deformable motor with a finite detachment rate k_{off} can be assimilated to a spring of rigidity k_m linking two motor units each moving with a maximal (unloaded) velocity v_m. As the motor units advance on the filaments, the spring becomes more tense and the motor units feel an increasing restoring force $\approx k_m x$, with $x \approx v_m t$ the motor displacement. The motor reaches stall when the opposing forces felt by the motor units become equal to the stall force f_s, which happens after a time $\tau_s \approx f_s/(k_m v)$. This occurs if the typical time during which the motor stays bound to the filament exceeds τ_s: $k_{\text{off}}\tau_s > 1$. In that case, the motor becomes stalled with a length $L_m \approx f_s/k_m$, and the contractile force dipole is given by Eq. (2.11). Conversely, if $k_{\text{off}}\tau_s < 1$, detachment typically occurs earlier than τ_m and $f \approx k_m x$ with $x \approx v_m/k_{\text{off}}$. Inserting these results into Eq. (2.10), we obtain

$$D_{\text{extensible}} \approx -k_m v_m^2/k_{\text{off}}^2. \tag{2.12}$$

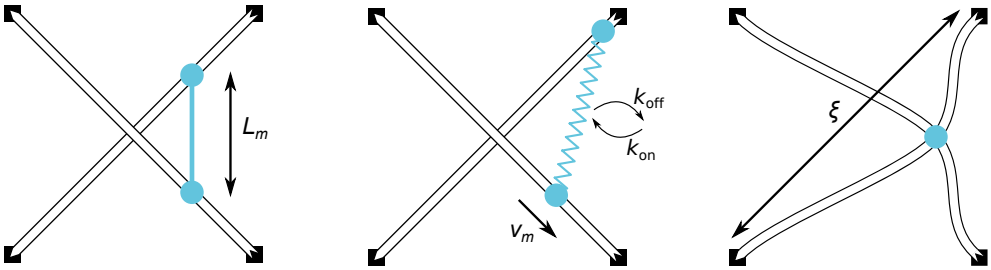

Figure 2.10: Several effects contribute to the motor being closer to the filament barbed ends than to their pointed ends on average, thus enabling zipper-like contraction as in Fig. 2.9(b-c): (a) the finite size of the motor (corresponding to relaxing assumption 2.), (b) the finite elastic compliance of the motor (corresponding to relaxing assumption 3.), and (c) the finite elastic compliance of the filaments (corresponding to relaxing assumption 4.)

- Deformable filaments bend when subjected to a transverse force, allowing the motor to move towards the filament barbed end. We consider filament sections of length ξ with bending energy $\int (k_B T \ell_p c^2/2)\, \mathrm{d}s$, where c is the filament curvature and s its arclength. In this case the restoring force associated with an infinitesimal transverse displacement of magnitude x is of order $k_B T \ell_p x/\xi^3$. Conversely, if the motor exerts a force f_s on the filament, its displacement will be of order $x \approx f_s \xi^3/(k_B T \ell_p)$. While a contribution to the force dipole of the form Eq. (2.10) exists in this case, an even larger contribution to the force dipole is found by estimating the filament tension needed to balance the motor force, namely $T \approx f_s \xi/x$. As this tension is applied to the crosslinking points, a distance $\approx \xi$ from the motor, the dominant contribution to the force dipole exerted is given through Eq. (2.9) by

$$D_{\text{deform}} \approx -T\xi \underset{f \ll k_B T \ell_p^{1/2}/\xi^{3/2}}{\approx} \frac{f^2 \xi^2}{k_B T}. \tag{2.13}$$

  While this expression is valid at low forces, for $f \gg k_B T \ell_p^{1/2}/\xi^{3/2}$ the restoring force is dominated by filament stretching, not bending. Applying a similar reasoning, we find

$$D_{\text{deform}} \underset{f \gg k_B T \ell_p^{1/2}/\xi^{3/2}}{\approx} f\sqrt{\xi \ell_p}. \tag{2.14}$$

To determine the dominant contraction mechanism among these three, we derive and compare the full analytical expressions corresponding to the approximative arguments presented above as a function of two experimentally controllable parameters: the number of myosin heads per myosin thick filament N [26] and the inter-crosslink length ξ. We consider actin filaments with persistence length $\ell_p = 10\,\mu$m. The myosin thick filaments have length $L_m = N l_m$ with $l_m = 3\,$nm, unloaded velocity $v_0 = 200\,\text{nm}\cdot\text{s}^{-1}$ and stall force $f_s = N f_0$. Since motor heads spend only a fraction of their time bound to actin, we estimate $f_0 = 0.1\,$pN on average. We use $k_m = \mu/L_m$ with $\mu = 45\,$nN a typical protein filament rigidity [27]. myosin II has a duty ratio $1 - p_d \simeq 4\%$ and a characteristic attachment-detachment time of $\tau_d = 3\,$ms [28], yielding a motor detachment rate $k_{\text{off}} = p_d^N/\tau_d$.

The colored domains in Fig. 2.11 indicate as a function of N and ξ which of the mechanisms enumerated above yields the largest dipole. The bottom-right half of the diagram is left blank as it involves very large motors ($L_m > \xi$) not captured by our current approach. The finite motor size mechanism tends to dominate in the vicinity of the diagonal where the motor size L_m is largest. The deformable motor mechanism dominates in the bottom left corner of the diagram. Filament deformability governs contractility in large-ξ regions where the filament sections are most flexible. As mentioned above, the position-dependent stall force mechanism is always negligible in front the finite size motor mechanism; thus it never dominates contractility. Detailed analysis reveals that this picture is remarkably insensitive on precise parameter values.

We next consider the total force dipole D, defined as the sum of the four force dipoles associated with the four contraction mechanisms. The magnitude of the total dipole per myosin head D/N is represented by

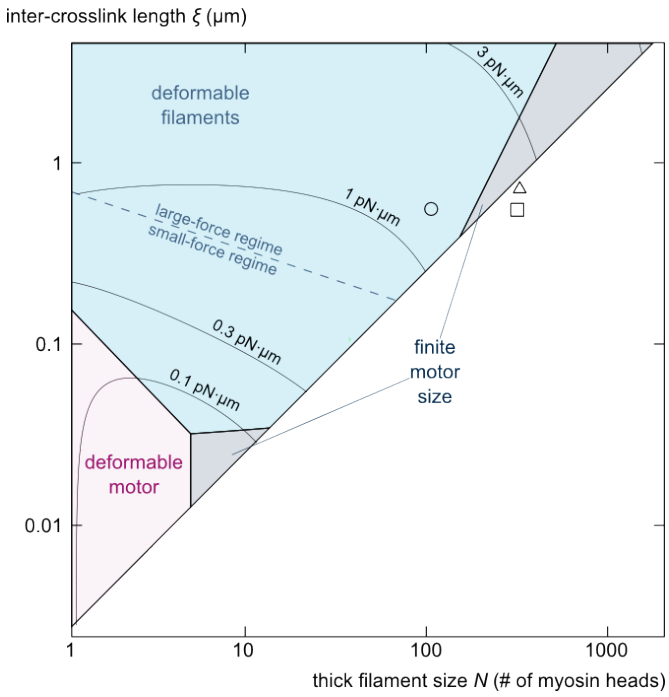

Figure 2.11: Contractile forces as a function of experimentally controllable parameters. Colors identify the dominant contraction mechanism in each parameter regime. Contours indicate the magnitude of the average contractile force dipole per myosin head $\langle D \rangle / N$. Symbols indicate the *in vitro* experimental regimes of Ref. [17] (*circle*), Refs. [18, 29] (*square*) and Ref. [30] (*triangle*).

contour lines in Fig. 2.11. In the $\xi \gtrsim 0.3\,\mu$m region, these forces compare with the force dipole exerted by a myosin head in striated muscle $D/N = (500\,\text{pN} \times 3\,\mu\text{m})/300 = 5\,\text{pN} \cdot \mu\text{m}$; filament deformation-based mechanisms dominate most of this parameter region. Conversely, for $\xi \lesssim 0.3\,\mu$m forces are much weaker, and possibly too small for experimental observation. Consistent with this, the typical network parameters used in *in vitro* experimental studies of actomyosin contractility are confined to the strong-contractility region (Fig. 2.11, symbols[1]). Interestingly, these symbols lie between the deformable filaments and the finite motor size contraction domains, suggesting that both mechanisms could play a role in these experiments.

Although we find that filament deformations dominate many significant regimes of actomyosin contraction, our focus on local actin deformation could still lead to an underestimate of their effect. Indeed, nonlocal deformations of the network over several mesh sizes could be more favorable than local deformations in heavily crosslinked networks or regimes where motors are larger than the inter-crosslink length. Collective effects could also be of importance, as stress propagation through the elastic filament network could lead to cooperativity between distant motors; we tackle these issues in the next two sections. We note that our weakly deformed network approach is only relevant for small motor forces or during the very early stages of larger-scale contraction. Further work is required to analyze strongly deformed or dynamically reorganizing networks and the corresponding synergies between several of the mechanisms described here (see Chapter 4). On such longer time scales, the microscopic interactions between filaments and motors considered here could furthermore shed light onto the self-organization of disordered actomyosin networks into more organized structures [7].

Reference: *Geometrical origins of contractility in disordered actomyosin networks.*
Martin Lenz, *Phys. Rev. X* **4**, 041002 (2014)

[1]The symbols' coordinates are computed by assimilating ξ to the networks' entanglement length $l_e = 620\,\text{nm}/c^{2/5}$, with the actin concentration c in units of mg/mL [31].

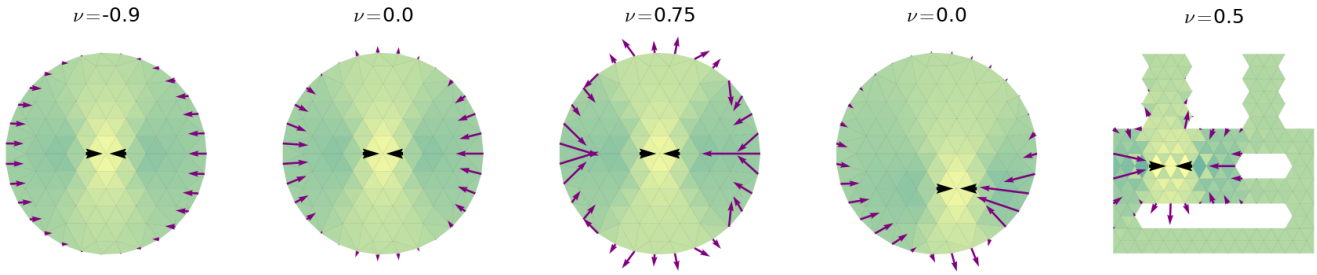

Figure 2.12: Boundary forces (*purple arrows*) transmitted by a two-dimensional homogeneous linear elastic medium under the influence of a localized force dipole (*black arrowheads*) computed using finite elements. The boundary force distribution is strongly influenced by both the medium's material properties (ν denotes the Poisson ratio) and the geometry of the problem. Nevertheless, in all cases the boundary dipole tensor is equal to the body forces' dipolar moment.

2.6 Ground rules for nonlocal linear force transmission

The local forces exerted by myosin molecular motors and evaluated in Sec. 2.5 are transmitted by a disordered elastic scaffold of actin fibers and determine much of the cell's active mechanics. More generally, forces in living systems are largely generated at the nanometric protein level, and yet biological function often requires them to be transmitted to much larger length scales. At the tissue scale for instance, contractile cells exert forces on their surroundings to participate in muscular contraction, clot stiffening [32] and wound healing [33]. Due to their physiological relevance, such systems have been extensively studied *in vitro*, and direct, dynamical imaging has recently progressed from macroscopic observations [34] to visualizations of the networks' microstructure [17, 18] as well as individual components [16] during contraction.

The abundance of different macroscopic behaviors generated by apparently similar microscopic components, which is particularly spectacular in the cytoskeleton, has attracted significant theoretical attention over the last decade. Two prominent theoretical strategies have emerged.

On the one hand, so-called "active gels" models emphasize macroscopic flows within the cytoskeleton, and do not formulate detailed assumptions about the microscopic interactions between motors and filaments [9, 35, 36]. Instead, they rely on symmetry considerations to derive the most general equations compatible with the problem considered, and successfully predict intricate patterns of motion resembling experimentally observed dynamical structures. While very general, these approaches involve a large number of unprescribed parameters enclosing the relevant aspects of the microscopic dynamics; in particular, the most important, specifically active aspects of the cytoskeletal dynamics are typically described by a phenomenological "active stress tensor".

On the other hand, length scales too small to be accurately captured by an active gel formalism have typically been modeled using both continuum [37] and discrete [38] elastic models. Such models yield insights into specific cellular processes such as mitotic spindle organization [39], lamellipodium growth [40] or intracellular propulsion [41], as well as into the propagation of dipolar forces generated by cells embedded in an elastic matrix [42]. However, although the bulk elastic properties of such models have been thoroughly investigated [42, 43] on a general basis, force transmission from the microscopic to the macroscopic level was only considered in numerical simulations of specific geometries [20, 38, 44, 45, 46, 47], and a general theoretical framework to understand this process is lacking.

Here we introduce such a formalism under the form of a direct relation—termed "dipole conservation"—between the macroscopic active stress and the force dipole tensor, a local quantity describing the individual force-exerting elements and whose trace D is identical to the "force dipole" discussed in the previous section and defined in Eq. (2.9). In this section we derive dipole conservation only for the elementary case of a homogeneous, continuum elastic medium and briefly discuss more technically involved generalizations to discrete and disordered networks [48].

Let us consider a general d-dimensional piece of elastic material at mechanical equilibrium, filling a domain Ω of space with boundary $\partial\Omega$ and volume V. We model the active elements embedded in the elastic body as a distribution of body forces $F_\mu(\mathbf{R})$. To quantify the macroscopic consequences of these active forces, we consider the response of the total system composed of the elastic medium and the embedded elements to an infinitesimal, affine deformation characterized by a strain tensor $\gamma_{\mu\nu}$. Under this transformation, a point belonging to the boundary $\partial\Omega$ of the elastic body with position $\mathbf{R}$ in the resting state is displaced by a quantity $\delta R_\mu(\mathbf{R}) = \gamma_{\mu\nu} R_\nu$ (summation over repeated Greek indices is implied). Denoting the elastic stress tensor by $\sigma_{\lambda\mu}(\mathbf{R})$ and considering a surface element $\mathrm{d}s_\lambda$ lying on the boundary $\partial\Omega$, the force exerted by the outside world on the surface element reads $-\sigma_{\lambda\mu}(\mathbf{R})\,\mathrm{d}s_\lambda$. As the surface element gets displaced by an infinitesimal δR_μ, the work performed by this force is $[-\sigma_{\lambda\mu}(\mathbf{R})\,\mathrm{d}s_\lambda] \times \delta R_\mu$. The change in energy of the total system is given by the work performed over the whole boundary:

$$\begin{aligned} \delta E &= \oint_{\partial\Omega} [-\sigma_{\lambda\mu}(\mathbf{R})\,\mathrm{d}s_\lambda] \times \delta R_\mu \\ &= -\gamma_{\mu\nu} \times \oint_{\partial\Omega} \sigma_{\lambda\mu}(\mathbf{R}) R_\nu\,\mathrm{d}s_\lambda. \end{aligned} \tag{2.15}$$

Noting that the integral in the right-hand side of Eq. (2.15) is the dipolar moment of the boundary forces, we refer to this quantity as the "boundary dipole tensor" and denote it as

$$\Delta_{\mu\nu} = \oint_{\partial\Omega} \sigma_{\lambda\mu}(\mathbf{R}) R_\nu\,\mathrm{d}s_\lambda. \tag{2.16}$$

The meaning of this new quantity becomes clear if we note that according to Eq. (2.15), $\Delta_{\mu\nu}$ is the derivative of the energy of the total system with respect to the boundary strain $\gamma_{\mu\nu}$. This is reminiscent of the definition of the stress tensor $\sigma_{\mu\nu}$ as the derivative of the energy density e with respect to the local strain tensor $\gamma_{\mu\nu}(\mathbf{R})$. Considering a coarse-grained approximation of the total system with a uniform bulk deformation $\gamma_{\mu\nu}$ and uniform stress $\tilde{\sigma}_{\mu\nu}$, we have $E = Ve$ with e a uniform elastic energy density and the boundary dipole tensor is directly related to the coarse-grained stress tensor:

$$\Delta_{\mu\nu} = \frac{\partial(Ve)}{\partial\gamma_{\mu\nu}} = -V\tilde{\sigma}_{\mu\nu}. \tag{2.17}$$

Thus $-\Delta_{\mu\nu}/V$ is the medium's coarse-grained stress tensor and $\Delta/(Vd) = \Delta_{\mu\mu}/(Vd)$ is the analog of a hydrostatic pressure. In an active medium language, $\Delta < 0$ thus characterizes a contractile medium while $\Delta > 0$ is associated with extensility.

As a first step towards establishing dipole conservation, here we rederive the so-called mean-stress theorem [45, 49]. We introduce the dipolar moment of the active forces $F_\mu(\mathbf{R})$ as

$$D_{\mu\nu} = \int_\Omega F_\mu(\mathbf{R}) R_\nu\,\mathrm{d}V. \tag{2.18}$$

Note that $D_{\mu\nu}$ is independent of the origin of the coordinates if the body forces sum to zero as expected for active elements embedded in an elastic medium, and that the total force dipole exerted by several active elements is equal to the sum of the individual force dipoles.

Inserting the force balance equation $\partial_\nu \sigma_{\mu\nu} = -F_\mu$ into Eq. (2.18) and integrating by part yields the mean stress theorem

$$D_{\mu\nu} = \oint_{\partial\Omega} \sigma_{\lambda\mu}(\mathbf{R}) R_\nu\,\mathrm{d}s_\lambda + \int_\Omega \sigma_{\mu\nu}(\mathbf{R})\,\mathrm{d}V. \tag{2.19}$$

Defining the integrated stress tensor $\Sigma_{\mu\nu} = \int_\Omega \sigma_{\mu\nu}\,\mathrm{d}V$ and using the definition of the boundary dipole Eq. (2.16), Eq. (2.19) can be cast into a compact form:

$$\Delta_{\mu\nu} = D_{\mu\nu} - \Sigma_{\mu\nu}. \tag{2.20}$$

This result holds irrespective of the medium's material properties, including homogeneity and linearity.

Despite its universality, in the general case the result of Eq. (2.20) involves a complicated unknown object $\Sigma_{\mu\nu}$ and is thus of limited practical use. Here we show that this limitation is lifted when considering a linear homogeneous elastic medium with fixed boundaries (useful generalizations for mobile boundaries are easily derived).

In a linear homogeneous elastic medium, stress is related to strain through a position-independent stiffness tensor: $\sigma_{\mu\nu}(\mathbf{R}) = C_{\mu\nu\alpha\beta}\gamma_{\alpha\beta}(\mathbf{R})$. Integrating this relation over space, we get

$$\Sigma_{\mu\nu} = C_{\mu\nu\alpha\beta}\Gamma_{\alpha\beta} \quad \text{with} \quad \Gamma_{\alpha\beta} = \int_\Omega \gamma_{\alpha\beta}(\mathbf{R}) \ \mathrm{d}V, \tag{2.21}$$

with $\Gamma_{\alpha\beta}$ the integrated strain. Assuming small displacements, we use the linear strain $\gamma_{\alpha\beta}(\mathbf{R}) = [\partial_\alpha u_\beta(\mathbf{R}) + \partial_\beta u_\alpha(\mathbf{R})]/2$ with $u_\alpha(\mathbf{R})$ the medium's displacement vector. Integration of Eq. (2.21) then yields a boundary integral

$$\Gamma_{\alpha\beta} = \oint_{\partial\Omega} \left[\frac{u_\beta(\mathbf{R})}{2} \, \mathrm{d}s_\alpha + \frac{u_\alpha(\mathbf{R})}{2} \, \mathrm{d}s_\beta \right]. \tag{2.22}$$

Equation (2.20) thus provides a decomposition of the boundary stress as a sum of a bulk term $D_{\mu\nu}$ involving active forces and a boundary term $\Sigma_{\mu\nu} = C_{\mu\nu\alpha\beta}\Gamma_{\alpha\beta}$ related to the system deformation. Note that the latter depends on the system's elastic properties through the stiffness tensor $C_{\alpha\beta\mu\nu}$, while the former does not. Now introducing the assumption of fixed boundary conditions, we find that the boundary displacements in the right-hand side of Eq. (2.22) vanish, implying that the whole integral vanishes. Using Eq. (2.21), we thus find that $\Sigma_{\mu\nu} = 0$, and thus Eq. (2.20) can be rewritten as the dipole conservation relation:

$$\Delta_{\mu\nu} = D_{\mu\nu} \tag{2.23}$$

which relates bulk and boundary forces. To understand the meaning of this equation, we decompose it into the equality of the traces, symmetric traceless parts and antisymmetric parts of the two tensors. The equality of the traces, $\Delta = D_{\mu\mu} = D$, is of particular interest for biological systems as it relates the "hydrostatic pressure" $\Delta/(Vd)$ of the medium to the local force dipole D, a quantity routinely interpreted as the amount of contractility of the active elements (see Refs. [20, 45, 46] as well as Secs. 2.5 and 2.7 of this thesis). Next, the symmetric traceless part of each of the two dipole tensors [$(\Delta_{\mu\nu} + \Delta_{\nu\mu})/2$ and $(D_{\mu\nu} + D_{\nu\mu})/2$] is analogous to a nematic order parameter characterizing the anisotropy of the corresponding forces, and thus their equality means that the anisotropy of the contractile forces is also conserved across scales. Finally, the equality $\Delta_{\mu\nu} - \Delta_{\nu\mu} = D_{\mu\nu} - D_{\nu\mu}$ of the antisymmetric parts is equivalent to torque balance in the elastic medium; since embedded active elements exert a vanishing total torque on the elastic medium, it simply reduces to $\Delta_{\mu\nu} - \Delta_{\nu\mu} = 0$, and thus expresses torque balance on the total system.

As shown in Eq. (2.23), the laws governing force transmission from the microscopic to the macroscopic scale in elastic materials take a simple, geometry-independent form in homogeneous linear elastic media, whereby the force dipole is an invariant of linear elasticity. More specifically, the macroscopic force dipole tensor exerted by the medium on its boundaries is equal to the sum of the microscopic force dipoles exerted on it by embedded active elements. While the derivation of Eq. (2.23) is elementary, a more detailed analysis allows us to prove that this relation also applies to discrete media with unspecified finite range interactions, making it relevant for popular biological fiber network models with stretching and bending energies [43]. We moreover prove that this relationship is conserved on average in the presence of disorder, but can be violated in nonlinear elastic media, which we discuss in more detail in Sec. 2.7. It also holds true in linear anisotropic media. Due to its generality, dipole conservation is a powerful tool to relate widely used macroscopic descriptions of the cytoskeleton, sometimes termed active gel theories, to the underlying microscopic phenomena. For instance, in a homogeneous linear elastic medium with a density ρ of embedded elements each exerting a force dipole $d_{\mu\nu}$, the active stress $\tilde{\sigma}_{\mu\nu}$—the central object of active gel theories—is simply given by $\tilde{\sigma}_{\mu\nu} = -\rho d_{\mu\nu}$ [see Eqs. (2.17) and (2.23)].

As biological media reorganize and flow under force, we expect their long-time behavior to depart from the elastic framework considered here and behave viscoelastically. Interestingly, for small enough deformation our results still apply in these cases. Indeed, both force balance and the linear relationship between stress and strain are still satisfied in viscoelastic systems, the only difference being that the elastic modulus

relating these two quantities is now frequency-dependent. However, if the material is liquid-like on long time scales we expect the resulting flows to induce large deformations, resulting in geometrical nonlinearities and violations of the dipole conservation. Finally, we note that geometrical nonlinearities are also more prevalent in disordered than homogeneous networks [50], implying that disorder might significantly affect contractility by lowering the threshold to nonlinear behavior. As a result, a reliable understanding of contraction in active biological materials requires a good characterization of the viscoelastic and nonlinear properties of the underlying matrix. We undertake a study of the latter in the next section.

Reference: *Connecting local active forces to macroscopic stress in elastic media.*
Pierre Ronceray, **Martin Lenz**, *Soft Matter* **11**, 1597 (2015)

2.7 Amplification of active forces in fiber networks

Going beyond the linear effects investigated in the previous section, we study how large-scale, nonlinear force transmission in fiber networks can affect the relationship between macroscopic stresses and microscopically imposed forces. To assess this, we numerically simulate force transmission in a lattice-based fiber network originally introduced in Ref. [51]. While the bulk properties of this and other model fiber networks have been thoroughly investigated theoretically [43], their *in vivo* function instead rely on their ability to transmit *localized* forces. In the nonlinear regime studied here, this local response cannot be straightforwardly inferred from the networks' bulk properties, and gives rise to an unexpected stress amplification, collective effects within populations of motors and the rectification of locally extensile forces into contractile large-scale stresses.

In the model, a crosslinked semiflexible filament network is represented by a regular lattice of bucklable filament sections. As shown in Fig. 2.13(a), each filament section is constituted of two quasi-inextensible bonds with length ξ (actually harmonic bonds with a large spring constant μ) hinged together so that deviations from a straight filament section carries an energy penalty proportional to the square of the deviation angle θ (for small deviations). In addition, consecutive filament sections through a lattice site are also hinged in a similar way. The elastic energy of the system thus reads

$$E = \sum_{\text{bonds } i} \frac{\mu}{2}(\ell_i - \xi/2)^2 + \sum_{\text{hinges } j} \frac{\kappa}{2}\theta_j^2, \tag{2.24}$$

with $\mu\xi^2 \gg \kappa$. As discussed in Sec. 2.5, motors in two- or three-dimensional fiber networks exert locally contractile force dipoles *on average*. However, depending on the local configuration of the neighboring filaments [in particular the respective length of the filament sections in Fig. 2.9(a)], individual motors can exert extensile as well as contractile force dipoles. The motor-to-motor fluctuations of this dipole can be much larger than the average contractile force dipole, implying that differences in the way that they are transmitted can strongly influence the overall active stress in a medium containing many motors.

We first model a local force dipole by applying two equal and opposite forces on two nodes of a circular patch of triangular fiber lattice as illustrated in the inset of Fig. 2.13(b). We numerically minimize the network's elastic energy through a conjugate gradient method and measure the boundary dipole Δ defined in the previous section. For small locally applied force dipoles D, the networks responds linearly, implying $\Delta = D$ as shown in Sec. 2.6. When the local forces exerted on the network exceed the buckling force of a filament section, however, Δ departs from the linear prediction. For contractile forces ($D < 0$), Δ remains contractile, but its magnitude is amplified significantly. For extensile forces, the boundary dipole Δ has an opposite sign compared to the locally imposed dipole. Thus fiber networks generically convert microscopic extensility into macroscopic contractility. This surprising effect could play a strong role in breaking the symmetry between contractility and extensility in actomyosin assemblies. To understand its origin, we look closely at the deformations in the region surrounding our force dipole [Fig. 2.13(b), inset]. Due to its anisotropy, the force dipole deforms the surrounding network by locally pushing in the longitudinal direction (blue-colored bonds), but also induces pulling in the transverse direction (red-colored bonds). As the network buckles locally under compression, the long-range propagation of compressive forces is compromised. As a results, only tensile forces propagate and the net boundary dipole is contractile.

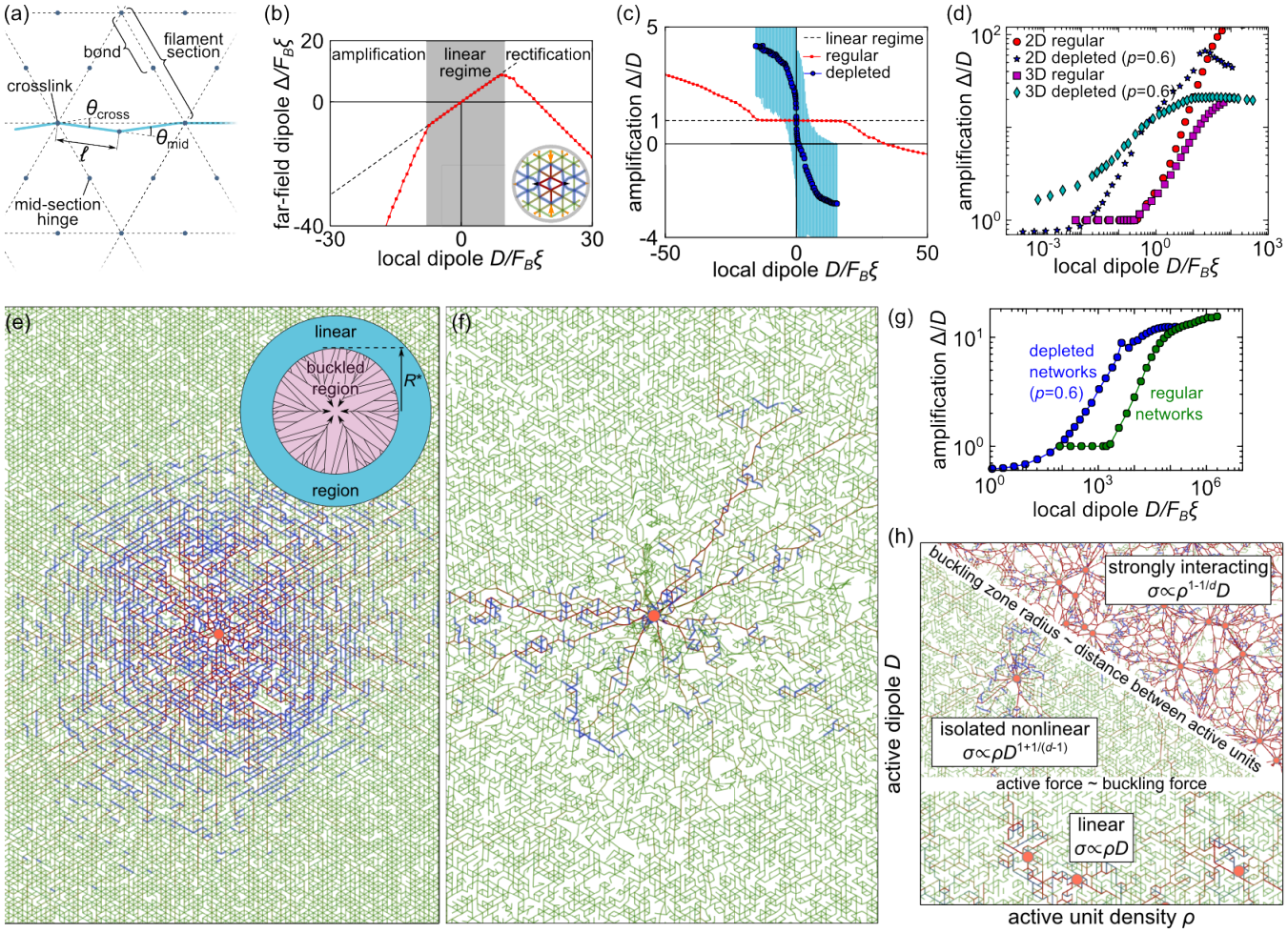

Figure 2.13: Force transmission from the microscopic to the macroscopic level in fiber networks. (a) Discrete elastic model for the filament network, with one deformed filament highlighted in *blue*. The hinge angles at one crosslink and one mid-section hinge are indicated; each of them contributes one hinge term to the right-hand side of the energy of Eq. (2.24). (b) Force transmission in a regular lattice, showing three distinct regimes as discussed in the main text. *Inset:* Network stresses in the vicinity of the force dipole (*arrowheads*) with the following color code: *blue:* buckled filament section, *green:* unstressed bond, *red:* extended bond, *yellow arrows:* forces exerted on the boundaries of the domain represented here. Due to buckling, these forces are predominantly contractile. (c) stress amplification factors in regular and depleted networks compared to the linear expectation (*dashed line*). The amplification and stress-reversal is much more pronounced in depleted networks, which respond linearly only over a very limited range of dipoles. Due to its disordered structure, the amplification factor associated with a depleted network is a random variable. The *blue symbols* and *light blue bars* denote its mean $\pm$ std computed over $\approx 10^5$ samples. (d) Amplification for the isotropic force dipole. (e) Large-scale force propagation in a high-coordination lattice ($p = 0.8 > p_c$), displaying a behavior similar to that of the regular lattice. Colors are as in the inset of (b). *Inset:* schematic of the nonlinear force transmission mechanism. (f) Large-scale force propagation in a low-coordination depleted lattice ($p = 0.58$). (g) Amplification factor in the presence of a finite motor density. The saturation occurs when the radius R^* of the buckled region becomes comparable to the inter-motor distance $\rho^{-1/d}$. (h) Phase diagram presenting the various force transmission regimes in depleted networks, with associated typical network configurations in the background.

In contrast with regular triangular lattices, in crosslinked actin networks connection points between filaments have a coordination of at most four, as individual crosslinks typically link two filaments (each extending in two directions) and not three as in the regular triangular lattice. This low coordination has important implications for the elasticity of such networks. Indeed, it implies that unlike triangular lattices, they can be deformed without changing the length of any filament section. The network can therefore be deformed without any stretching or buckling. This is easily understood from a simple constraint counting argument originally due to Maxwell: consider N point-like crosslinks, each with a connectivity of z in a space of dimension d. There are Nd degrees of freedom associated with the positions of the crosslinks, and the assumption that the filament sections each retain a constant length imposes $\sim Nz/2$ scalar constraints. If the number of constraints is smaller than the number of degrees of freedom, or equivalently $z < 2d$, deformations of the network where every filament section retains its resting length (and thus remains unbuckled) are possible. In practice, the existence of such modes of deformation results in networks whose macroscopic rigidity is dramatically smaller than that of a more highly coordinated network. Indeed, they are dominated by bending and thus have a typical modulus of order $\kappa\xi^{-d}$ [43]. Remembering that $\mu\xi^2 \gg \kappa$, we find that this is much smaller than the typical elastic modulus $\mu\xi^{2-d}$ of a high-coordination network dominated by stretching. Moreover, low-coordination networks tend to display strong nonlinear elastic behavior at small imposed strain [52].

To understand how these features of realistic fiber networks affect our results on force transmission, we randomly remove each bond in our two-dimensional triangular lattice with a probability p. As a result, the average coordination of its crosslinks becomes $z = 6p$. Placing ourselves in dimension $d = 2$, the number of constraints $Nz/2$ is larger than the number of degrees of freedom $dN = 2N$ if $p > p_c = 2/3 \simeq 0.67$. Under these conditions, the network behaves similarly to the full triangular lattice. On the other hand, if $p < p_b = (\sqrt{11/3} - 1)/2 \simeq 0.46$ the network is so sparse that it can be deformed without any stretching of bond or even any bending of hinges. It thus becomes completely floppy, and its macroscopic elastic modulus vanishes altogether. In this study, we focus on the generic behavior of macroscopically rigid, actin gel-like fiber networks and thus focus on the range[2] $p_b < p < p_c$. Noting that a value of p close to either p_b or p_c elicits a complex, highly collective response of the network [51], we stay away from these critical points in the following. Unless otherwise specified, in the following we use $p = 0.6$ as representative of the generic behavior of fibrous networks. As shown in Fig. 2.9(c), depleted networks transmit forces in a qualitatively similar way as our triangular lattice, displaying both amplification and dipole reversal for large extensile local dipoles. Due to their strong propensity for nonlinear behavior, the amplification in depleted networks is however much stronger than in regular ones.

To understand the origin of force dipole amplification in the presence of buckling, we study the response of the network to an isotropic contractile dipole capable of exerting arbitrarily large forces on the surrounding network. This allows a more thorough exploration of the large-dipole nonlinear regime compared to the anisotropic dipole discussed above. Indeed, the anisotropic dipole can only pull on the surrounding network as long as the two nodes on which it exerts forces are not collapsed to a point. We implement our isotropic dipole by introducing a short-range attraction between a specific node i of the network and any node j located within a distance $2d$ of it, where d is a length of order ξ. Specifically, we choose $d = 1.95\xi$ and use an attractive potential with energy

$$E_{\text{attraction}} = \begin{cases} \frac{E_0}{2}\left(\frac{r}{d}\right)^2 - E_0 & \text{if } r \leqslant d \\ -\frac{E_0}{2}\left(\frac{2d-r}{d}\right)^2 & \text{if } d < r \leqslant 2d \\ 0 & \text{if } 2d < r \end{cases} \tag{2.25}$$

where $r = |\boldsymbol{r}_j - \boldsymbol{r}_i|$ and E_0 is the trap depth. By increasing E_0, we can increase the attractive strength of node i by an arbitrary amount, implying that an increasing number of network nodes are swallowed into its region of influence with radius $2d$. We compute the local force dipole D through Eq. (2.18), where the $\boldsymbol{F}_i$ are the attractive forces deriving from the attractive potential of Eq. (2.25). The scaling of the resulting force dipole amplification factor Δ/D is presented in Fig. 2.13(d). For regular networks, the amplification

[2]The value given here for p_b and p_c are in fact derived from a mean-field constraint counting argument and are thus approximative. More precise values have been extracted from numerical simulations [51]. These corrections are however not essential for our discussion.

factor is equal to one, as expected for linear response as long as $D < F_B\xi$. Above this threshold, bonds buckle within the network, leading to $\Delta/D \propto D^{1/(d-1)}$. This dependence is explained by the mode of force transmission illustrated in the inset of Fig. 2.13(e). In this simplified picture, the network is divided into a completely buckled region of radius R^* where only filaments that are under extension matter for force transmission. As a result, the network behaves as a network of tense, interconnected radial ropes. The pulling force of the dipole is conserved as it is transmitted in the radial direction, and for any value of the radial coordinate r it is shared between a number $n(r) \approx (r/\xi)^{d-1}$ of outgoing ropes. As the force exerted by the dipole on each outgoing rope at a radius ξ is of order D/ξ, the force carried by an individual rope decays as

$$f(r) \approx \frac{D/\xi}{n(r)} \approx \frac{D\xi^{d-2}}{r^{d-1}}. \tag{2.26}$$

The size of the buckled region is determined by imposing that $f(R^*) \approx F_B$, implying

$$R^* \approx \xi \left(\frac{D}{F_B\xi}\right)^{1/(d-1)}. \tag{2.27}$$

Beyond R^*, forces propagate as in a linear elastic medium ($f \propto r^{2-d}$). To this elastic medium, the buckled region appears as a force dipole exerting $n(R^*)$ forces each of order F_B over a region of typical size R^*. As a result, the force dipole exerted by the buckled region on the linear region reads

$$D^* \approx n(R^*)F_B R^* \approx D\frac{R^*}{\xi} \approx D\left(\frac{D}{F_B\xi}\right)^{1/(d-1)}. \tag{2.28}$$

The linear medium faithfully transmits this force dipole to large distances as in Sec. 2.6, thus

$$\frac{\Delta}{D} \approx \frac{D^*}{D} \approx \left(\frac{D}{F_B\xi}\right)^{1/(d-1)}, \tag{2.29}$$

consistent with the scaling observed for regular networks in Fig. 2.13(d). At very large forces, the size of the buckled region saturates as it becomes comparable to the total size $\mathcal{R}$ of the network. This accounts for the saturation of the amplification factor for $R^* \approx \mathcal{R}$, *i.e.*, $\Delta \approx D\mathcal{R}/\xi$. The size of the buckling zone as a function of exerted dipole as well as the decay of the network stresses with distance are consistent with the scenario outlined above (not shown).

We further monitor dipole amplification in depleted networks. The qualitative evolution of the amplification factor with local force dipole is similar to that in regular networks, including the saturation of the amplification as the radius of the buckling zone becomes comparable to that of the network. However, the amplification factor in the intermediate regime $\xi < R^* < \mathcal{R}$ is much larger than in regular networks. Moreover, the scaling exponent of Δ/D with D is smaller. Qualitatively, this is due to a different structure of the buckling region in depleted networks, shown in Fig. 2.13(e-f). Indeed, while buckling is observed in all directions in isotropic networks, the irregular structure of depleted networks causes it to extend along finger-like force chains instead. This leads to a larger overall buckling region and stronger dipole amplification, even though the saturating value of the amplification must be the same in regular and depleted networks. We do not yet have a convincing argument for the specific value of the force amplification exponents in the depleted case, nor have we yet been able to determine whether their value sensitively depends on p.

Whether we consider regular or depleted lattices, the above results indicate that an isolated force dipole may become amplified by an arbitrarily large factor provided that the buckling zone has sufficient space to grow. By contrast, in biological systems individual force dipoles are often present at a finite density, be they motors in the cytoskeleton or force-exerting cells embedded in a filamentous extracellular matrix. This poses the question of whether a finite density of dipoles leads to cooperative or antagonistic interactions. Simulating a finite density ρ of motors in a large filamentous network with periodic boundary conditions, we find that the corresponding amplification factor grows as previously, but saturates as the size of the buckled region becomes comparable to the typical inter-motor distance $\rho^{-1/d}$ [Fig. 2.13(g)]. Indeed, as within the buckling region a fraction of order one of the filament sections are buckled, the merging of the

buckling regions regions implies that a fraction of order one of all filament sections become buckled. From that point, the total number of buckled bonds cannot increase dramatically, yielding a saturation of force amplification in the network. These results are summarized in the "phase diagram" of Fig. 2.13(h).

Reference: *Amplification of active forces in fiber networks.*
Pierre Ronceray, Chase Broedersz, **Martin Lenz**, *in preparation* (2015)

2.8 Outlook

The current paradigm to understand stress generation by actomyosin networks is strongly based on the well-characterized sarcomeric contractility found in striated muscle. In this model, myosin motors exert contractile forces, while the role of the surrounding actin scaffold merely consists in transmitting these forces to larger scales. In contrast, our results on the contractility of disordered actomyosin networks suggest a radically different picture, where individual myosin motors exert randomly contractile or extensile forces depending on the local geometry of their surroundings. Actin filaments then not only transmit forces, but also rectify them towards contraction and amplify them.

Our predictions on the amplification of localized force dipoles in fiber networks are quantitatively supported by a range of experiments in $d = 2$ and $d = 3$ in tissues as well as actomyosin and covering all the regimes predicted in Fig. 2.13(h). Indeed, a comparison of the pulling force $F = 15\,\mathrm{nN}$ exerted by a single platelet of size $d = 2\,\mu\mathrm{m}$ and yielding a force dipole $D = -Fd = -3 \times 10^{-14}\,\mathrm{N \cdot m}$ [32] to the active contractile stress $\rho\Delta = 150\,\mathrm{Pa}$ generated by a blood clot—*i.e.* fibrous networks rendered contractile by a concentration $\rho = 3 \times 10^8\,\mathrm{cells \cdot mL^{-1}}$ of the same platelets [34]—indicate a dipole amplification factor $\Delta/D = 17$. Using a persistence length $\ell_p = 0.5\,\mu\mathrm{m}$ and conservatively assuming that the fibrin mesh size is larger than two hundred nanometers ($\xi \geqslant 200\,\mathrm{nm}$) [53], we estimate a buckling zone size $R^* = \xi(F/F_B)^{1/2} \geqslant 70\,\mu\mathrm{m}$ (with $F_B \approx k_B T \ell_p^2/\xi^3$), larger than the inter-cell distance $\rho^{-1/3} = 15\,\mu\mathrm{m}$. The buckling zones of neighboring cells thus interpenetrate [strongly interacting regime in Fig. 2.13(h)]. In this regime, we predict a dipole amplification factor $\Delta/D = \rho^{-1/3}/L \simeq 8$, in order-of-magnitude agreement with the experimental result.

Turning to another system, in Ref. [29] a crosslinked actin network with mesh size $\xi = 200\,\mathrm{nm}$ is populated by myosin thick filaments of size $d = 1\mu\mathrm{m}$ each comprising $\simeq 300$ myosin heads. Due to the end-polar geometry of the thick filament, no more the 25% of all heads can act on a single actin filament at any time. Each of these actively exerts a $f_1 = 4\,\mathrm{pN}$ force a fraction 2% of the time [28]. The motor thus exerts an average force $F = 1/4 \times 300 \times 0.02 \times 4\,\mathrm{pN} \simeq 6\,\mathrm{pN}$. This force is too small to induce filament buckling ($F \ll F_B = 50\,\mathrm{pN}$). We thus predict linear force transmission in this experiment [linear regime in Fig. 2.13(h)], and thus $\tilde{\sigma}_{\mu\mu} = \rho D = \rho F d \simeq 12\,\mathrm{Pa}$, where we used $\rho = 2 \times 10^{18}\,\mathrm{m^{-3}}$. While this active stress is not directly measured in Ref. [29], we are able to infer it from the amount of shear stiffening observed in the network, yielding $\tilde{\sigma}_{\mu\mu} \simeq 14\,\mathrm{Pa}$, in very good agreement with our prediction.

Finally, an experimental study currently under revision [54] uses a novel surface tension measurement technique to reveal that an average three thick filaments ($F \simeq 6\,\mathrm{pN}$ as above) on giant unilamellar lipid vesicles with radius $r \simeq 10\,\mu\mathrm{m}$ covered by a two-dimensional actin network ($\xi = d = 1\,\mu\mathrm{m}$) generates active stresses on par with the vesicle's membrane tension $\rho\Delta \approx \sigma \approx 10^{-6}\,\mathrm{N \cdot m^{-1}}$. Computing the buckling force as $F_B = 0.4\,\mathrm{pN}$ and assuming a highly coordinated network, we predict a buckling radius $R^* = \xi F/F_B = 15\,\mu\mathrm{m}$ that is both larger than the mesh size and smaller than the inter-motor spacing $\rho^{-1/2} \simeq 20\,\mu\mathrm{m}$, where we used $\rho = 3/(4\pi r^2)$ [isolated nonlinear regime in Fig. 2.13(h)]. This yields an amplification factor $\Delta/D = 15$, and an overall two-dimensional active stress $\tilde{\sigma}_{\mu\mu} = \rho F R^* \simeq 2 \times 10^{-7}\,\mathrm{N \cdot m^{-1}}$. While this order-of-magnitude is consistent with our current rough estimate of the experimentally relevant active stress, it is interesting to note that the agreement improves if we consider a low-coordinated rather than high-coordinated filament network model, leading to enhanced amplification as in Fig. 2.13(g).

While these calculations offer encouraging estimates covering all our predicted regimes, more detailed *in vitro* experimental validations will allow to further refine our understanding of force transmission in biological fiber networks. We are currently discussing such possible tests with the Gardel, Murrell and Sykes labs in Chicago, Yale and Institut Curie. The *in vivo* situation is obviously more complicated, not

least due to the experimental uncertainty regarding the exact degree of polarity organization of any given physiological actomyosin structure. While this uncertainty makes it difficult to attribute the contractility of a given actomyosin structure to either simple sarcomeric contractility or to the mechanisms discussed here, we believe that an undeniable achievement of our approach is to allow this discussion by offering a viable alternative to actomyosin contractility.

Further elaborating on the applicability of our ideas to *in vivo* systems, we note that although this chapter is entirely phrased in terms of filament buckling, none of its results are specifically tied to this mechanism. Indeed, the essential characteristic underpinning the behaviors described here is that an individual filament section should resist under extension while yielding under compression. This property could stem from a number of different processes, including selective severing of filaments depending on their tension as observed with severing protein cofilin [55]. Another possible mechanism could be provided by an increased propensity of the filaments to break when subjected to a torque of a given sign. Indeed, the helical structure of the filaments implies that the sign of the torque exerted by a myosin motor on a filament section is correlated to whether it puts that filament section under compression or extension. Finally, the question of whether inelastic reorganizations of sufficiently fluid actomyosin networks under the influence of motors could favor contractility remains open.

Chapter 3

Mechanical regulation of membrane trafficking

Eukaryotic cells are enclosed by a thin, impermeable lipid bilayer. To allow vital exchanges with the outside world as well as between cellular compartments, specialized proteins must constantly tubulate, cut, deform, and fuse this membrane. One crucial such process is clathrin-mediated endocytosis [Fig. 3.1(a)], during which a coat of the protein clathrin deforms the membrane into a spherical bud containing a molecular cargo of interest. Protein dynamin is next recruited to the neck of the bud, polymerizes into a helix and hydrolyzes the cellular fuel guanosine triphosphate (GTP) to detach the bud from the membrane, thus creating a transport vesicle which is then processed by the cell. While this process pulls a vesicle *into* the cell, Cells also perform the topologically opposite operation of pushing a vesicle *away* from the cytoplasm. As illustrated in Fig. 3.1(b), this job is performed by the protein complex ESCRT-III in many situations, including the generation of multivesicular bodies involved in protein and lipid degradation, cytokinesis and viral budding. All these processes are highly specific, and targeting them to the right cellular locations at the right time involves a complex and intensively studied interplay of molecular signals.

Beyond these biochemical considerations, significant physical forces are also involved in deforming the cellular membrane at such small (a few 10 nm) scales. This cost is described by the Helfrich energy functional, which gives the energy of a piece of membrane (*e.g.*, a forming vesicle) in contact with a reservoir (*e.g.*, the cell membrane) as a function of its shape [56]:

$$\mathcal{H} = \iint \left(\frac{\kappa}{2}c^2 + \sigma\right) \mathrm{d}S, \tag{3.1}$$

where $\kappa \approx$ 10-100k_BT is the membrane's bending modulus, σ the tension of the membrane reservoir, c the local curvature and where the integral runs over the surface of the membrane.

In a longstanding collaboration with the experimental group of Aurélien Roux at the Biochemistry Department of the University of Geneva, we go beyond the well-studied biochemistry of membrane trafficking machinery to extract insights from the mechanics and thermodynamics of its constituents. This is a challenging task due to the small size of these objects, which implies that their dynamics cannot be directly resolved through optical imaging. As a result, our structural knowledge chiefly stems from static electron micrographs. To extract crucial dynamical information about these processes, we use mathematical and physical modeling to integrate the information obtained through indirect experimental techniques including force measurements, optical microscopy and atomic force microscopy (AFM). In this chapter we present three such studies elucidating how clathrin deforms the membrane (Sec. 3.1), how dynamin severs it (Sec. 3.2) as well as proposing a mechanism for the unknown mode of operation of the membrane-remodeling ESCRT-III complex (Sec. 3.3). We show that the mechanics of the lipid bilayer has a strong influence on their function, suggesting that the biological regulation of endocytosis might not only be biochemical, but also mechanical (see also our review article Ref. [57]).

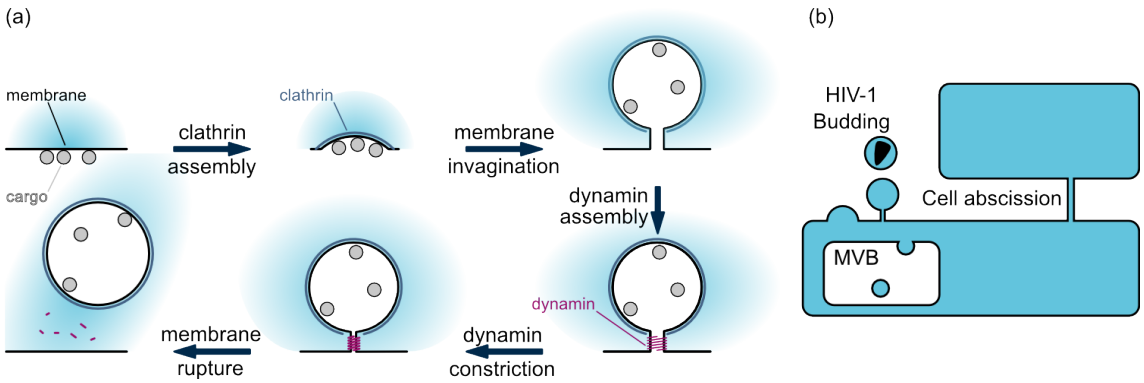

Figure 3.1: Two crucial membrane trafficking processes. In both drawings *blue* denotes the cell cytoplasm. (a) The successive steps of clathrin-coated endocytosis. The typical diameter of a clathrin-coated bud is 50-100 nm. (b) The ESCRT complex assembles at the membrane on the cytoplasmic side to generate vesicles away from the cytoplasm, notably multivesicular bodies (MVBs) involved in protein and lipid degradation.

3.1 Control of clathrin coat formation by membrane mechanics

Budding of spherical vesicles is essential for membrane trafficking. Clathrin has been the first protein found to be involved in this process [58, 59]. Clathrin polymerizes into truncated icosahedral cages *in vitro* [60] and together with various partners [61] deforms the membrane into a spherical bud [62, 63]. Among the mechanisms involved in bud formation, amphipathic insertions, that act as wedges to create curvature, and crowding effect [64] of proteins binding asymmetrically to the membrane have been investigated. In contrast, clathrin has been proposed to act by scaffolding, meaning that a protein coat of a given shape forces the membrane to curve [61]. The structure of the smallest clathrin cage is known in great detail [65, 66, 67]. However, clathrin also forms flat hexagonal lattices at the plasma membrane of cells [68] and spherical coated vesicles of various sizes, ranging from 35 nm to 200 nm in various organisms [69]. This variability in size and shape has called into question the initially proposed membrane scaffolding mechanism based on clathrin polymerization (image adapted from Ref. [70]).

To study the mechanism by which clathrin deforms the membrane, we reconstitute clathrin coats onto giant unilamellar vesicles (GUVs—diameter 5-50 μm) whose lipid composition mimics the composition of the inner plasma membrane leaflet. In the presence of an excess of the membrane adaptor protein AP180, clathrin in solution binds to the membrane, forming a uniform coat. This coat behaves as a two-dimensional solid, as demonstrated by the absence of recovery after photobleaching. Electron microscopy (EM) on large unilamellar vesicles under similar conditions moreover reveals the formation of clathrin cages at the membrane [Fig. 3.2(e)].

To investigate the role of membrane tension on clathrin assembly, we transfer GUVs made in a 208 ± 1 mOsm sucrose solution to a clathrin/AP180 solution of varying osmolarity. We examine clathrin polymerization on GUVs under hypotonic (180 ± 1 mOsm), isotonic (208 ± 1 mOsm) and hypertonic (236 ± 1 mOsm) external buffer conditions. While this technique does not allow precise control over the membrane tension, isotonic conditions ensure that its value is moderate, and yield no optically visible deformations of GUVs [Fig. 3.2(b), (d), (e)]. Hypotonic conditions promote a high (although lower than the lysis tension $\approx 10^{-3}\,\mathrm{N \cdot m^{-1}}$) surface tension, and prevent AP180/clathrin binding in most cases [Fig. 3.2(a), (d)]. In all case studied here, fluorescent AP180 binds efficiently and with the same density whether or not clathrin is present. We thus conclude that increased membrane tension can directly impair clathrin polymerization. Strikingly, under hypertonic (low-tension) conditions result in strong clathrin and membrane fluorescence signals, and electron microscopy reveals an entirely budded surface, covered with an electron-dense coat [Fig. 3.2(c), (d), (f)]. In many cases, long, highly coated membrane tubules emanate from the GUVs, suggesting that under hypertonic conditions, the membrane is heavily deformed by the clathrin coat.

These observations demonstrate that clathrin coat binding is affected by membrane tension. Since a high tension inhibits clathrin binding, this also suggests that the formation of a clathrin coat is related

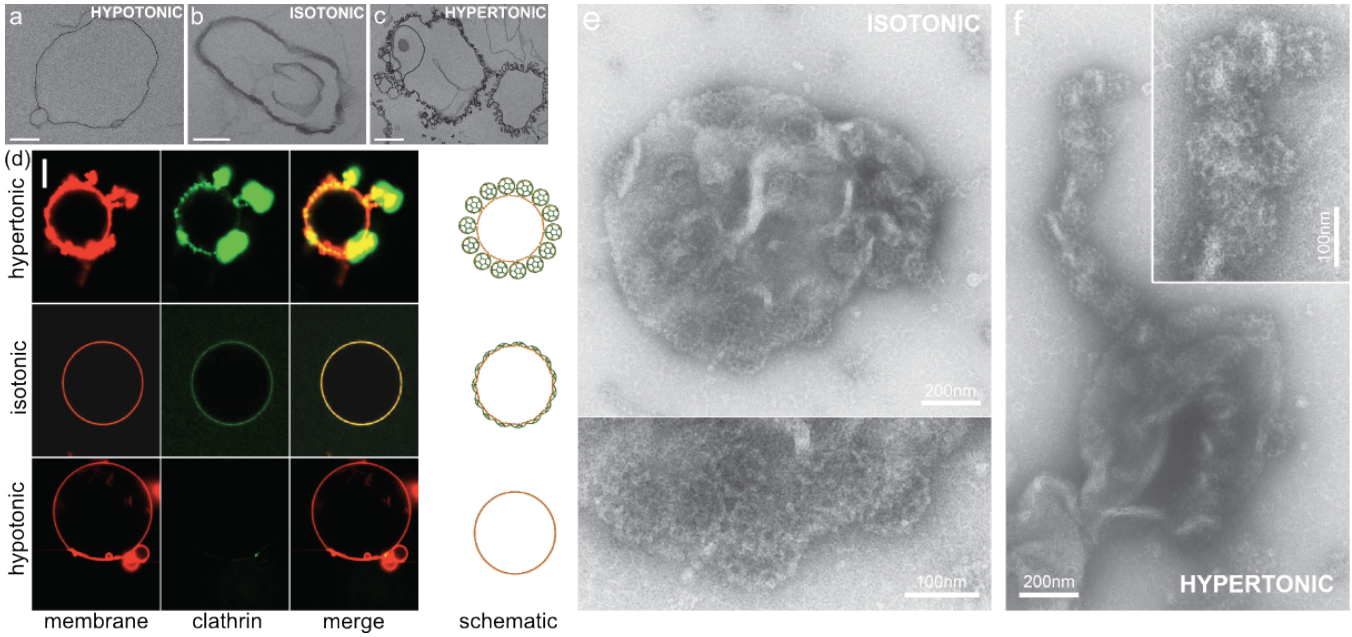

Figure 3.2: The morphology of clathrin coats reconstituted on GUVs is dictated by the osmotic pressure difference between the inside and the outside of the vesicle. Hypertonic conditions yield a low surface tension, which results in membrane tubulation and the formation of spherical coats, as seen in transmission EM (c), fluorescence microscopy (d) and negative stain EM. Isotonic conditions, which result in a moderate surface tension, induce the formation of a moderate amount of shallow buds (b, d). Finally, hypotonic conditions imply a high surface tension and prevents clathrin binding (a, d, f).

to the availability of extra membrane area, and thus requires at least some membrane deformation. To enable quantitative tests of this hypothesis, we develop a theoretical model that describes the competition between clathrin polymerization (which favors full budding) on the one hand, and membrane tension and rigidity (which favor planar membranes) on the other to predict transitions between different possible bud shapes [Fig. 3.3(a)]. In the model, a membrane of tension σ and bending rigidity κ is in contact with a clathrin/AP180 solution of fixed concentration. We denote by μ the free energy gain associated with the polymerization of a unit area of coat. As membrane-bound clathrin coats are very rigid (bending rigidity $\kappa_c \simeq 300 k_B T$ [71]), we make the assumption that clathrin always polymerizes into spheres of fixed radius $r_c = 32.5\,\mathrm{nm}$ (estimated from electron microscopy). In our model, tension cannot modify the coat's radius, but it can limit clathrin polymerization to partial buds as illustrated in Fig. 3.3(a-b). Accordingly, our model considers four possible bud states illustrated in Fig. 3.3(a): 1–bare membrane: clathrin cannot polymerize, and the membrane remains uncoated; 2–shallow partial bud: clathrin polymerizes partially into buds that are less than a half-sphere; 3–deep partial bud: clathrin polymerizes into a bud that is more than a half sphere but less than a full sphere, leaving a patch of flat, bare membrane at the base of the bud; and 4–full bud: a full spherical clathrin coat forms around the membrane bud. This coat is traversed by a small membrane tether of negligible energy [72] that relates the membrane bud to the main membrane. This connection is the only difference between our full buds and free clathrin-coated vesicles. This description is consistent with the partial coats observed by negative stain EM.

In the model, we decompose the polymerization energy of clathrin into two contributions:

$$\mu = \mu_0 - \frac{\kappa}{2r_c^2}, \tag{3.2}$$

where μ_0 is the (positive) clathrin binding free energy and $-\kappa/(2r_c^2)$, the cost of bending the membrane into a bud. Additionally, we introduce the coat's line tension τ, describing the energetic cost of broken clathrin-clathrin bonds at the boundary of a partial bud. The model thus leads to the following expression for the free energy of a single bud:

$$F = \sigma A_m - \mu A_c + \tau L \tag{3.3}$$

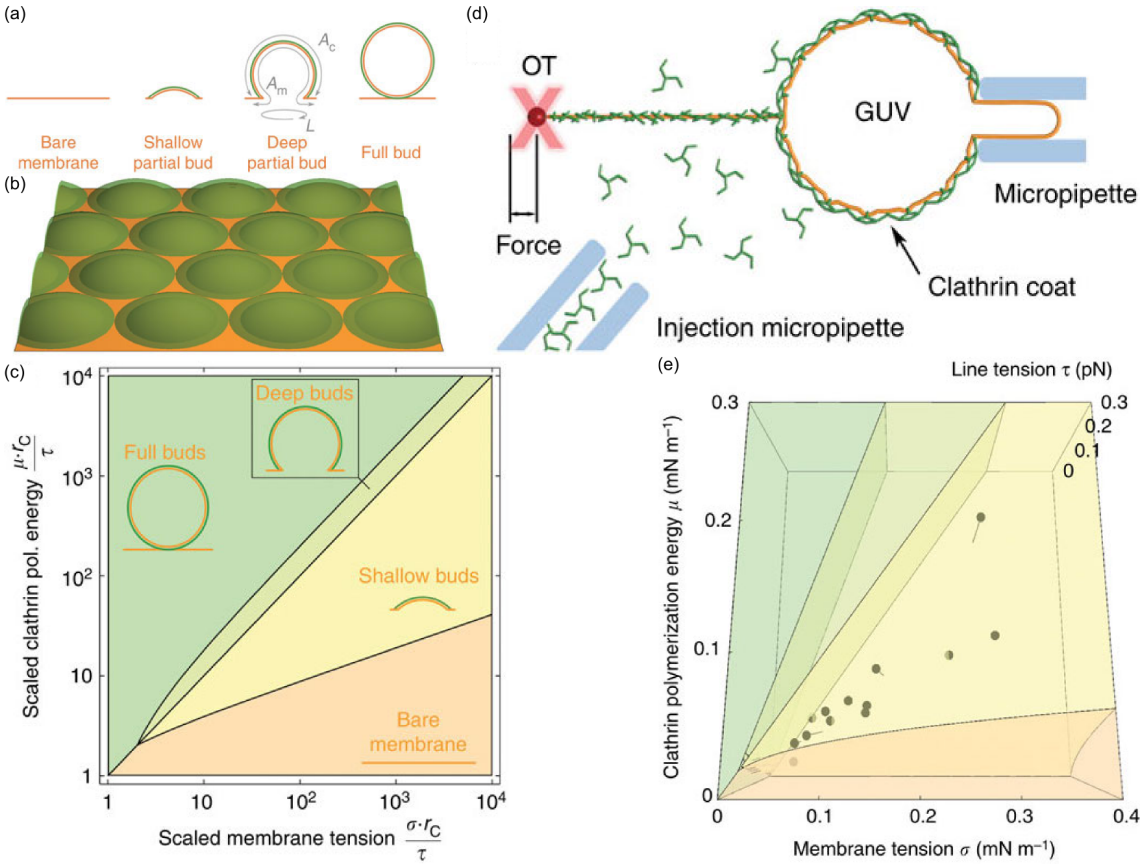

Figure 3.3: Model and clathrin polymerization energy measurements. (a) The four possible states of a single bud considered in the model: bare membrane (no clathrin binding), shallow partial budding, deep partial budding and full budding (yielding a closed bud). Parameterization of the bud is shown on the deep partial bud as discussed in the text. (b) Our mathematical model predicts the state of a membrane densely packed with contiguous buds. Our fitting of the model parameters (see main text) predicts a bud depth $\simeq 2\,\mathrm{nm}$. (c) Phase diagram predicted by our model, showing the predicted budding state as a function of the scaled tension and polymerization energy (logarithmic plot). (d) Experimental setup for the measurement of the clathrin polymerization energy: OT, optical tweezers; GUV, giant unilamellar vesicle. (e) Three-dimensional phase diagram with individual experimental measurements represented as black circles (linear plot). The clathrin polymerization energy was measured from 15 independent experiments.

where A_m and A_c are the membrane and coat areas associated with one bud, and L is the length of its rim [Fig. 3.3(a)]. In this expression, μ is dimensionally equivalent to a force per unit length, and represents the net force that a clathrin coat applies on the membrane while polymerizing. The membrane tension σ and the bending rigidity κ oppose this tendency to polymerize, while the coat's line tension τ favors buds with short rims. To make predictions at the liposome level, we apply this theoretical framework to a densely packed assembly of coated buds [Fig. 3.3(b)]. Depending on the value of the parameters, we can analytically predict the shape of the clathrin buds (bare membrane, shallow/deep partial buds or full buds) as shown on the phase diagram [Fig. 3.3(c)]. Qualitatively, high line tensions ($\mu < 2\tau/r_c$) strongly penalize partial buds, implying that the membrane is either bare for high tensions ($\sigma > \mu$) or fully budded if $\sigma < \mu$. These two regimes still exist at low line tensions ($\mu > 2\tau/r_c$), but with the added possibility of partial buds at moderate membrane tensions. This latter situation reproduces our above observations of GUVs under various osmotic conditions (Fig. 3.2).

To validate our model, we simultaneously measure the membrane tension σ and clathrin polymerization energy μ. We use an *in vitro* micromanipulation assay [Fig. 3.3(d)] [73] to pull a membrane nanotube out of GUVs by means of a streptavidin bead held in optical tweezers. We modulate the membrane tension σ by aspirating the GUV in a micropipette. This technique allows us to quantify and control tension, in a way that cannot be achieved by osmotic shocks. We measure the force f required to maintain the tube

using optical tweezers. In the absence of clathrin, this force and the radius of the tube are given by the minimization of Eq. (3.1) for a cylindrical membrane under a longitudinal force [74]:

$$f = 2\pi\sqrt{2\kappa\sigma} \qquad \text{and} \qquad r_b = \sqrt{\frac{\kappa}{2\sigma}}. \tag{3.4}$$

Direct measurement of f using the optical tweezers allows us to measure the membrane bending modulus $\kappa = 13 \pm 5 k_B T$; as a result, the model of Eq. (3.3) has only two free parameters μ and τ. Once the tube is formed, a mix of clathrin and adaptor in isotonic buffer is injected using a second micropipette. Homogeneous clathrin binding is observed on the membrane tube and on the GUV surface. Following clathrin polymerization, we observed a reduction δA of the total apparent GUV membrane area, consistent with the sequestration of the membrane into clathrin-coated pits. During clathrin polymerization on the GUV and the tube, we also measure a drop δf in the tube force. Relating δA and δf to the values of μ and τ within the model of Eq. (3.3), we are able to infer values of μ and τ for each individual experiment that we perform. From these values, our model predicts whether the coat forms on the membrane, and whether the resulting bud is partial or full. As shown in Fig. 3.3(e), in each case studied we predict a partial bud. On the other hand, direct observation of the GUVs using fluorescence microscopy reveals thin coats in every experiment similar in appearance to those observed in Fig. 3.2(d–isotonic). This validates our prediction and confirms our hypothesis that the continuous staining of clathrin-coated GUVs in isotonic conditions is associated with contiguous shallow buds. On average, we find that $\mu = 7.6 \pm 5.4 \times 10^{-5}\,\mathrm{N \cdot m^{-1}}$, with $\mu_0 = 1.0 \pm 0.5 \times 10^{-4}\,\mathrm{N \cdot m^{-1}}$ and $\tau = 5.2 \pm 7.4 \times 10^{-2}\,\mathrm{pN}$, well below values at which line tension is able to bud membrane domains on its own (typically 1 pN [75]). This supports our interpretation that membrane bending is primarily driven by clathrin polymerization and not to line tension.

The clathrin polymerization energy μ_0 is the sum of two contributions: clathrin-clathrin interactions and clathrin-membrane interactions mediated by the adaptors, which we express as $\mu_0 = \mu_{\text{c-c}} + \mu_{\text{c-m}}$. In the scaffolding model, clathrin polymerization is the main driver of membrane deformation, implying that $\mu_{\text{c-c}}$ is much larger than $\mu_{\text{c-m}}$. To test this model, we estimate the relative importance of $\mu_{\text{c-c}}$ and $\mu_{\text{c-m}}$ by measuring the force required to rupture the clathrin coat. We aspirate a clathrin-coated GUV using a micropipette of radius $R_p \simeq 1\,\mu\mathrm{m}$ (Fig. 3.4) in isotonic conditions. For moderate pressures, the vesicle retains its spherical shape as the coat prevents membrane deformation. We then gradually increase the aspiration pressure by an amount ΔP. While no change is observed initially, above $\Delta P_c = 231 \pm 26\,\mathrm{Pa}$ the coat suddenly ruptures along the rim of the pipette, following which the membrane tongue (portion of the membrane lined with the walls of the pipette) elongates dramatically (Fig. 3.4, bottom row). We reason that rupturing the coat in this way disrupts the clathrin-clathrin bonds while leaving the clathrin-membrane interactions essentially unaffected, thus allowing us to estimate $\mu_{\text{c-c}} = 1.1 \pm 0.1 \times 10^{-4}\,\mathrm{N \cdot m^{-1}}$. This value is indistinguishable from the previously measured value $\mu_0 = 1.0 \pm 0.5 \times 10^{-4}\,\mathrm{N \cdot m^{-1}}$, confirming that clathrin-clathrin interactions are predominant in driving clathrin assembly, consistent with the scaffolding model. Multiplying $\mu_{\text{c-c}}$ by the specific area $a \simeq 800\,\mathrm{nm^2}$ occupied by a triskelion yields the binding energy per triskelion $a\mu_{\text{c-c}} = 23 \pm 3 k_B T$, consistent with a previous theoretical estimate based on the critical concentration of clathrin polymerization [76], $a\mu_{\text{c-c}} = 42 k_B T$, and with estimates coming from computational assembly statistics [77], where $a\mu_{\text{c-c}} = 23 k_B T$. Also, it is too large to allow for internal rearrangements of the clathrin lattice once polymerized, implying that clathrin buds directly polymerize into curved structures rather than going through a hexagonal flat coat intermediate.

A final prediction of our model is that a higher membrane budding rigidity should inhibit budding. Indeed, we predict that an increase in κ results in a lowering of $\mu = \mu_0 - \kappa/(2r_c^2)$, favoring a flat membrane as indicated in the phase diagram of Fig. 3.3(c), (e). We use GUVs of higher bending rigidity obtained by adding sphingolipids and cholesterol, resulting in a bending rigidity $\kappa = 51 \pm 20 k_B T$. This decreases the average value of μ by more than an order of magnitude ($\mu_{\text{stiff}} = 3.7 \times 10^{-6}\,\mathrm{N \cdot m^{-1}}$), implying a dramatic decrease of the maximum tension allowing clathrin assembly to $3.5 \times 10^{-6}\,\mathrm{N \cdot m^{-1}}$. Consistent with our expectation, clathrin fails to bind to a vast majority of liposomes under all osmotic conditions investigated above, despite significant binding of AP180.

In summary, here we show that clathrin polymerization is counteracted by membrane tension, which hinders the closure of the clathrin-coated pits. The clathrin polymerization energy is found to be in the

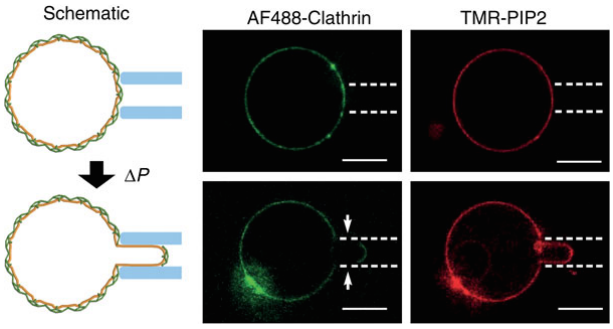

Figure 3.4: Clathrin coat rupture experiments. Schematic and confocal images of GUVs coated with fluorescent clathrin before and after being aspirated using a pipette. Arrows show the clathrin-uncoated part of the membrane tongue.

range of *in vivo* membrane tension values (10^{-5}-$10^{-4}\,\mathrm{N}\cdot\mathrm{m}^{-1}$), supporting a possible physiological control of clathrin budding through membrane tension. Consistent with this, clathrin-mediated endocytosis is delayed in cells that have higher membrane tension, and requires actin for completion [78, 79]. At the structural level, we propose that membrane tension may not allow for the correct binding angle between arms of the triskelia, impairing their correct association. We also find that increased membrane rigidity opposes clathrin budding. This is consistent with the fact that clathrin-mediated endocytosis is slower at the apical pole of epithelia, where the membrane is more rigid than at the basal pole [80]. We also find (not shown here) that if the membrane adaptor epsin is used instead of AP180, its known membrane deforming ability stemming from the insertion of its amphipathic helix favors clathrin-mediated budding, even when the membrane's elastic parameters (namely tension and rigidity) are not favorable. This indicates that the different actors that can generate membrane curvature (wedge insertion, crowding or local forces exerted by the cytoskeleton) can act synergistically to deform the membrane. Our results support a modulatory role of each adaptor and actin depending on the difficulty of deforming the membrane [79]: in extreme cases where membrane is very stiff and tension is high, all partners are required, whereas they become dispensable in intermediate conditions.

Reference: *A balance between membrane elasticity and polymerization energy sets the shape of clathrin coats.*
Mohammed Saleem, Sandrine Morlot, Annika Hohendahl, John Manzi, **Martin Lenz***, Aurélien Roux* (*equal contributions) *Nat. Commun.* **6**, 6249 (2015)

3.2 Mechanism for membrane severing by dynamin

Dynamin is part of a protein superfamily that has been proposed as one of universal membrane tubulation and fission molecules. Its representatives are involved in many processes including budding of transport vesicles, division of organelles, cytokinesis and pathogen resistance [81]. As discussed above (see Fig. 3.1), dynamin is a GTPase that polymerizes into helical collars at the neck of clathrin-coated pits. While a variety of mechanisms have been proposed for the membrane-severing action of dynamin over the years [82], a consensus has emerged that fission is likely driven by a constriction of its helical structure. Nevertheless, the specific mechanism for this fission is unknown.

When assembled in absence of GTP, the unconstricted dynamin helix surrounds a membrane tube with a radius $r_u = 10\,\mathrm{nm}$ [83, 84]. Upon GTP hydrolysis, a conformational change of dynamin at the dimer and the polymer levels [85, 86, 87] constricts the membrane [84, 88]. Constriction correlates with a reduction of the helix radius, itself reflected by a reduction of the number of dimers per helix turn from 14 to 13 [85] and torsion. This torsion of the entire helical polymer can be monitored by live imaging [89]. Early models [90, 91] have proposed that the dynamin helix would constrict down to such a small radius that the two sides of the membrane tube would come in contact with each other and locally fuse into a single bilayer structure. The resulting "hemifusion" intermediate would then spontaneously evolve towards full

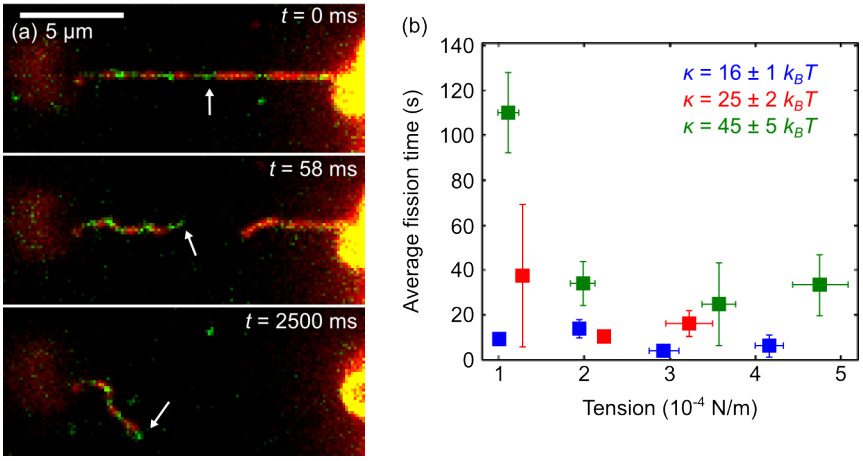

Figure 3.5: Experimental characterization of dynamin fission. (a) Images from dual-color spinning disk confocal microscopy of an experimental setup similar to that of Fig. 3.3(c), showing the retraction of the membrane tube following dynamin-induced fission. After fission, the extremity of the left stump is covered with green dynamin, whereas the right stump is uncoated, showing that fission occurred at the edge between a seed of dynamin (white arrows) and the dynamin-free membrane tube. (b) Dependence of fission time on membrane tension and bending modulus κ. *Squares and bars:* experimental average $\pm$ sem.

membrane rupture [92].

More recent data have however modified our understanding of the possible role of constriction in dynamin-mediated membrane fission: (1) dynamin cryoelectron microscopy images and 3D reconstruction show that the polymer can constrict down to radius r_c = 4-5 nm [84], filled with a tubular membrane (2 nm thick) that surrounds a water lumen (2-3 nm) [85]. These structural data support the idea that dynamin does not reach the hemifission state by constriction alone. (2) GTP-mediated constriction and torsion do not lead to fission unless the tube is both attached to the substrate [84] and subjected to longitudinal tension [89]. These results show that membrane constriction is not sufficient for fission and also suggest that mechanical parameters of the membrane (tension, bending rigidity) could play role in controlling fission.

As the dynamin helix constricts, it imposes a strong curvature on the membrane tube that it covers. This strong curvature has a high energetic cost, suggesting that the mechanism of dynamin constriction could be significantly constrained by membrane elasticity. We thus study how membrane mechanics influences the dynamin-mediated fission reaction. Using a similar micromanipulation setup as that of Fig. 3.3(d), we form a membrane tube of controlled radius [Fig. 3.5(a)] partially covered by relatively short (a few hundreds of nm) dynamin helices. GTP is required for fission, and we find that the membrane ruptures only after tens of seconds. This is much longer time than required for the conformational change of our short dynamin helices, as determined in our previous work [93, 94]. Therefore, the forces associated with the conformational change do not directly tear or fuse the membrane, but merely facilitate its later breakage. We next observe that GTP-induced fission occurs preferentially at the boundary between the helix-covered and the bare membrane, as shown in Fig. 3.5(a). These fission events are moreover more frequent when the helix is in contact with the vesicle or the bead than when it was in the middle of the tube. We then consider the influence of membrane tension and bending rigidity (controlled through its lipid composition as in Sec. 3.1), and find that fission proceeds more quickly for high tension and low bending modulus [Fig. 3.5(b)].

To rationalize these observations, we develop a model where membrane breakage is eventually induced by a thermal fluctuation that brings the two walls of the membrane tube in close enough proximity to induce their hemifusion, from which full fission follows [Fig. 3.6(a)]. We thus assimilate membrane breakage to a barrier crossing problem under thermal agitation, predicting that its duration is (1) exponentially distributed and (2) has a mean satisfying an Arrhenius law

$$\langle \tau \rangle \propto e^{-(E^*-E_c)/k_BT}, \tag{3.5}$$

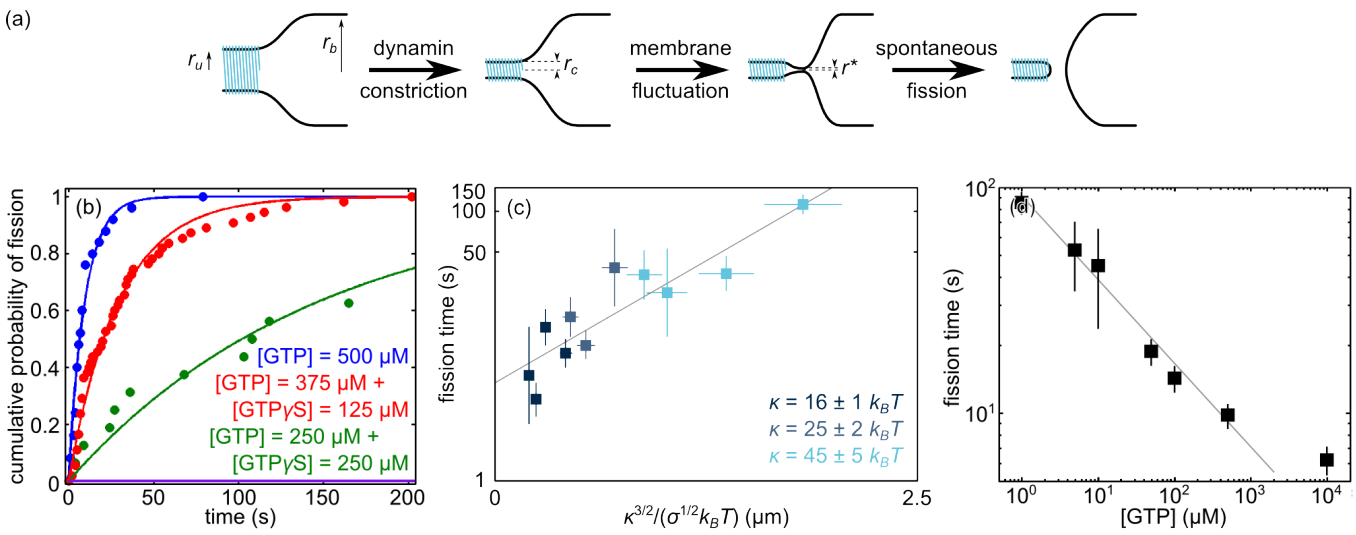

Figure 3.6: Proposed model and tests of its predictions. (a) Hypothesized dynamin fission sequence. (b) Cumulative probability distributions for fission of a subjected to different concentration of hydrolyzable GTP and its non-hydrolyzable analog GTPγS. *Circles:* experimental points. *Lines:* exponential fit. (c) Test of the expected dependence of fission time on the membrane's mechanical parameters (*line*) a in Eq. (3.7). *Squares and bars:* experimental average $\pm$ sem. The data is the same as in Fig. 3.5(b) (d) Dependence of fission time on GTP concentration (experimental average $\pm$ sem) and theoretical expectation from Eq. (3.11).

where E^* is the energy of the intermediate state and E_c is that of the initial, constricted state. Prediction (1) is well verified experimentally, as shown in Fig. 3.6(b). To quantitatively assess the validity of Eq. (3.5), we numerically compute the energy E^* of the membrane in the intermediate state. The scaling of the result can be understood from a simple argument where the energy of the membrane is dominated by that of its narrowest portion. Denoting by r^* its smallest radius and by r_b the radius of the bare tube, we note that the characteristic length for the elastic screening of a perturbation of the tube radius is r_b. This suggests that the lateral extent of the narrow region is of order r_b, implying a characteristic area $r^* \times r_b$. Its curvature is dominated by r^*, and the membrane energy per unit surface is thus dominated by the bending energy density $\kappa/[2(r^*)^2]$ [see Eq. (3.1)]. Using Eq. (3.4), we thus find

$$E^* \approx \left[\frac{\kappa}{2(r^*)^2}\right] \times r^* r_b \approx \frac{\kappa^{3/2}}{r^* \sigma^{1/2}}. \tag{3.6}$$

Combining this prediction with Eq. (3.5), we find

$$\log(\langle\tau\rangle) \propto \kappa^{3/2}/\sigma^{1/2}. \tag{3.7}$$

Fig. 3.6(c) shows that this dependence is well verified experimentally, validating our prediction (2). Numerically minimizing the membrane energy, we validate the scaling arguments presented above as well as compute the numerical prefactor in Eq. (3.6) for both a dynamin helix located in the vicinity of the vesicle and one far away from it. This allows us to estimate the corresponding fission times, and the resulting estimates quantitatively account for the experimentally measured differences.

Our simple model also allows us to predict the dependence of the dynamin fission time on the GTP concentration. As demonstrated in our previous work from very general symmetry arguments, GTP hydrolysis affects the structure of the dynamin much as an external torque Γ would [93, 94]. If the system is weakly out-of-equilibrium[1], this torque depends linearly on the chemical potential difference between GTP and its

[1]While the validity of this specific assumption is not completely clear in our experimental conditions, in practice a perhaps more plausible Michaelis-Menten prediction yields as good an agreement with the data as Eq. (3.8). In any case, distinguishing between these two dependences is not important for our main point.

hydrolysis products, yielding

$$\Gamma(c_{\mathrm{GTP}}) = \Gamma_0 \ln\left(\frac{c_{\mathrm{GTP}}}{c_0}\right), \tag{3.8}$$

with c_{GTP} the GTP concentration and where Γ_0 and c_0 are constants. Through the use of magnetic tweezers, we are able to measure $\Gamma_0 = 1.1 \pm 0.3\,\mathrm{nN}\cdot\mathrm{nm}$ at $c_0 = 1\,\mu\mathrm{M}$, comparable to our previous theoretical estimates [93, 94]. A simple estimate of the competition between this dynamin torque and the bending energy of the membrane allows us to determine the helix' constricted radius as a function of the GTP concentration as well as the mechanical parameters of the membrane:

$$r_c = \frac{r_b}{1 + \Gamma/(2\pi p\sqrt{2\sigma\kappa})}, \tag{3.9}$$

where $p \simeq 13\,\mathrm{nm}$ is the pitch of the dynamin helix. In the realistic case where $r_c \ll r_b$, we develop an estimate for the constricted energy E_c similar to that of Eq. (3.6):

$$E_c \approx \frac{\kappa^{3/2}}{r_c\sigma^{1/2}} \approx \frac{\Gamma_0 r_b}{p} \ln\left(\frac{c_{\mathrm{GTP}}}{c_0}\right), \tag{3.10}$$

where we substituted r_c using Eq. (3.9) and Γ using Eq. (3.8). Inserting Eq. (3.10) into Eq. (3.5), we predict the dependence of the fission time on GTP concentration:

$$\log(\langle\tau\rangle) \approx \frac{\Gamma_0 r_b}{k_B T p} \ln\left(\frac{c_{\mathrm{GTP}}}{c_0}\right), \tag{3.11}$$

again finding excellent experimental agreement [Fig. 3.6(d)]. Finally we perform experiments on live cells showing that the effect of membrane tension on dynamin localization at the base of clathrin-coated pits and rate of endocytosis is qualitatively consistent with our model.

Overall, our study proposes a solution to the longstanding puzzle of dynamin-mediated tube fission and validates it with unprecedented quantitative accuracy. Our results support a mechanism by which dynamin constricts within a few hundred milliseconds, forcing the membrane to reach a high elastic energy state at the edge of the dynamin coat. This state then spontaneously fissions over a few seconds. However, whether this mechanism applies *in vivo* without any differences is not completely clear. Indeed, the fission times observed in our experiments remain much longer than the ones observed in cells. The key to this discrepancy might reside in the numerous partners involved in the formation of dynamin helices *in vivo*, such as proteins amphiphysin and endophilin, and whose exact role remains to be clarified. More broadly, it will be interesting to investigate whether dynamin-independent fission reactions relying on different energy source may rely on similar mechanisms.

Reference: *Membrane shape at the edge of the dynamin helix sets location and duration of fission.* Sandrine Morlot, Valentina Galli, Markus Klein, Nicolas Chiaruttini, John Manzi, Frédéric Humbert, Luìs Dinís, **Martin Lenz**, Giovanni Cappello, Aurélien Roux, *Cell* **151**, 619 (2012)

3.3 Membrane deformation by the ESCRT-III complex

Membrane trafficking is essential to many crucial processes in the life of eukaryotic cells. Accordingly, they have developed many different tools to remodel their membrane depending on biological context. Thus, while the clathrin-dynamin system is used in situations where the cell needs to import cargo, a different machinery is used in cases where cellular material is to be exported. Here we explore this topologically opposite situation where a membrane bud needs to be generated away from the cytoplasm, and the resulting membrane neck severed from the *inside*. Interestingly, while a protein scaffold deforms the membrane in this context, the detailed mechanism is quite different from the rigid coating developed by clathrin and investigated in Sec. 3.1.

Here we focus on processes involving the Endosomal Sorting Complex Required for Transport III (ESCRT-III). The ESCRT-III complex is composed of a several proteins known as Vps20, Snf7, Vps2, Vps24 which

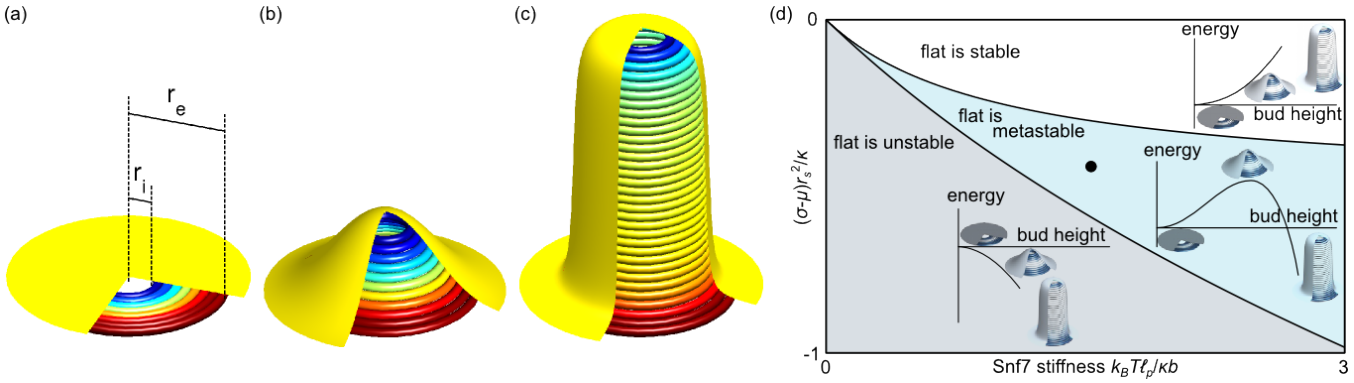

Figure 3.7: Illustration of the proposed buckling mechanism. Overbent filaments are represented in blue, underbent filaments in red, and the membrane in yellow. Wedges of the membrane were removed for visualization. (a) Curved filaments with an affinity for each other and the membrane form membrane-bound circular arrays. The tension and bending modulus of the membrane tend to stabilize flat arrays. (b) Buckling, on the other hand, allows the binding of more filaments and the relaxation of those already bound to their preferred (yellow) radius. These stabilizing and destabilizing effects balance at the buckling threshold. (c) The formation of long tubes allows the binding of an arbitrarily large number of filaments close to their preferred radius. (d) Phase diagram for the composite membrane, showing parameter regions where a flat membrane is stable, metastable or unstable with respect to tube formation. *Black circle*: Estimate of experimentally relevant parameters. (discussed in Sec.3.3.4)

polymerize into filamentous structures that lie in contact with the membrane. The most abundant protein within these filaments is Snf7, with the others mainly regulating the initiation and the termination of the filaments. The three ESCRT complexes, ESCRT-I, -II and -III, were initially identified for their involvement in protein sorting at the surface of vacuoles, a yeast organelle devoted to the degradation of the cell's waste and the functional equivalent of the mammalian lysosomes. Among all ESCRTs, only ESCRT-III is believed to take part into the mechanical deformation of the vacuolar membrane, a function that we focus on in the present study [95].

Here we first present our theoretical proposal for the mode of action of ESCRT-III, which hypothesizes that Snf7 filaments store a significant amount of energy during their growth that can then be liberated to deform the membrane (Sec. 3.3.1). We then test this hypothesis in a dual theoretical-experimental work, where we first analyze the growth dynamics of ESCRT-III filaments *in vitro* (Sec. 3.3.2) and use these results to directly investigate the central assumptions of our model (Sec. 3.3.3). Finally, in Sec. 3.3.4 we reflect on the insights gained on the *in vivo* membrane deformation process.

3.3.1 A theoretical proposal

Our first foray into the mode of action of ESCRT-III consists in a theoretical proposal based on a study of COS-7 cells overexpressing Snf7 [96]. In this work, deep-etch electron micrographs reveal circular arrays of curved Snf7 polymers under the plasma membrane [Fig. 3.7(a)]. This is evidence of the strong affinity of these filaments for the membrane [97] and for each other [98], as well as of their intrinsic curvature. When an ATP-hydrolysis deficient mutant of Vps4—an ATPase involved in the disassembly of ESCRT-III filaments [98, 99]—is present, long membrane-covered tubes of Snf-7 filaments are observed [Fig. 3.7(c)]. Similar structures appear in *in vitro* systems using purified proteins [100]. This suggests that tubes always form *in vivo* but that in the presence of normal Vps4 alone they are immediately cut off the membrane to form vesicles. In our model, we propose that this flat-to-tubular transition is a general feature of systems where curved filaments with attractive interactions bind to a membrane and study this physical effect akin to the buckling of a rod (Fig. 3.7).

We consider an infinite, initially flat lipid bilayer parametrized by its radial coordinate r. A subdomain $r_i < r < r_e$ of this surface is bound to an array of filaments. The present simplified discussion assumes

$r_i = 0$ and $r_e = +\infty$. The dressed membrane is then put into contact with the cytoplasm, which acts as a reservoir of filaments. We consider only axisymmetric configurations and assume that the dressed membrane is very thin. We write the free energy of the dressed membrane as

$$\mathcal{F} = \int_{r\in\mathbb{R}^+} \left(\frac{\kappa}{2}c^2 + \sigma\right) d\mathcal{A} + \int_{r\in\mathbb{R}^+} \left[\frac{k_B T \ell_p}{2b}\left(\frac{1}{r} - \frac{1}{r_s}\right)^2 - \mu\right] d\mathcal{A}. \tag{3.12}$$

The first term is the Helfrich free energy of the membrane as in Eq. (3.1). The second term represents the free energy of a filament array with inter-filament spacing b. The filaments have a spontaneous curvature r_s^{-1}, and due to the cylindrical symmetry their actual curvature is r^{-1}. A Taylor expansion about r_s^{-1} to second order yields the filament stiffness $k_B T \ell_p$, where ℓ_p denotes the persistence length. We denote by μ the chemical potential difference between Snf7 in the cytoplasm and bound to the membrane. We assume that μ is uniform throughout the filament array. Eq. (3.12) also ignores the up-down asymmetry of the dressed membrane, which a detailed analysis shows is small enough to not significantly affect our conclusions.

We minimize the free energy $\mathcal{F}$ over tube shape as a function of total tube height, revealing three regions of stability as shown in Fig. 3.7(d). If the membrane tension σ is significantly larger than the binding chemical potential per unit surface μ, the flat membrane is globally stable. Conversely, a significantly negative $\sigma - \mu$ implies that the flat membrane is linearly unstable, yielding unbounded tube growth. Finally, for moderate $\sigma - \mu$, the flat membrane is metastable, with the Snf7 array packing significant lateral compression. If sufficiently disturbed, the array is destabilized and tubes are formed. We propose that this regime accounts for the observed coexistence of flat arrays and long tubes, the latter being assumed to later mature into vesicles through an as yet unknown mechanism. The energy barrier associated with this metastable state amounts to several tens of $k_B T$, suggesting that *in vivo* ESCRT-III- mediated budding may be assisted by some unknown active process (*e.g.*, actin polymerization, which is regulated by the ESCRT-associated protein Alix [101], or the action of the Vps4 ATPase).

Reference: *Membrane Buckling Induced by Curved Filaments.*
Martin Lenz, Daniel J. G. Crow, Jean-François Joanny, *Phys. Rev. Lett.* **103**, 038101 (2009)

3.3.2 ESCRT-III assembly process

The mechanism proposed above requires growth-induced stress accumulation in Snf7 arrays to be sufficiently large to deform the membrane. To investigate the existence and magnitude of these stresses, we conduct experiments where a lipid bilayer is deposited on a planar mica or glass surface and then put in contact with a solution containing the proteins constituting the ESCRT-III complex. High-speed atomic force microscopy (AFM) is used to monitor the growth dynamics of the Snf7 spirals, demonstrating that small 25 nm radius Snf7 ring form on the surface, which subsequently grow radially by addition of further Snf7 monomers [Fig. 3.8(a)]. The growth of the radius is sublinear with time, consistent with a growth of the disk area πr^2 at a constant speed w:

$$\pi r^2 = \pi r_0^2 + wt. \tag{3.13}$$

Such a law is expected if Snf7 monomers are added at a constant rate to one filament growing end within the spiral, and we fit $w = 80 \pm 36\,\mathrm{nm}^2 \cdot \mathrm{s}^{-1}$ to the data of Fig. 3.8(b). The formation of new Snf7 rings on the bare membrane is very rare ("homogeneous nucleation"), and most new spirals are initiated from the side of existing ones as shown in Fig. 3.8(c) ("heterogeneous nucleation"). Unfortunately these events are too rare for us to directly infer a nucleation rate from AFM imaging. Both nucleation and growth stop when the membrane is completely covered with disks, and we measure the final distribution of disk sizes with an average final disk radius $\langle r \rangle = 123\,\mathrm{nm}$ as shown in Fig. 3.8(d).

To understand the growth process through which internal stresses are generated in ESCRT-III and determine the physiologically important Snf7 spiral nucleation rate, we develop a mathematical description of the dynamics of the process by which Snf7 spirals cover the surface. In the model, Snf7 spirals are represented

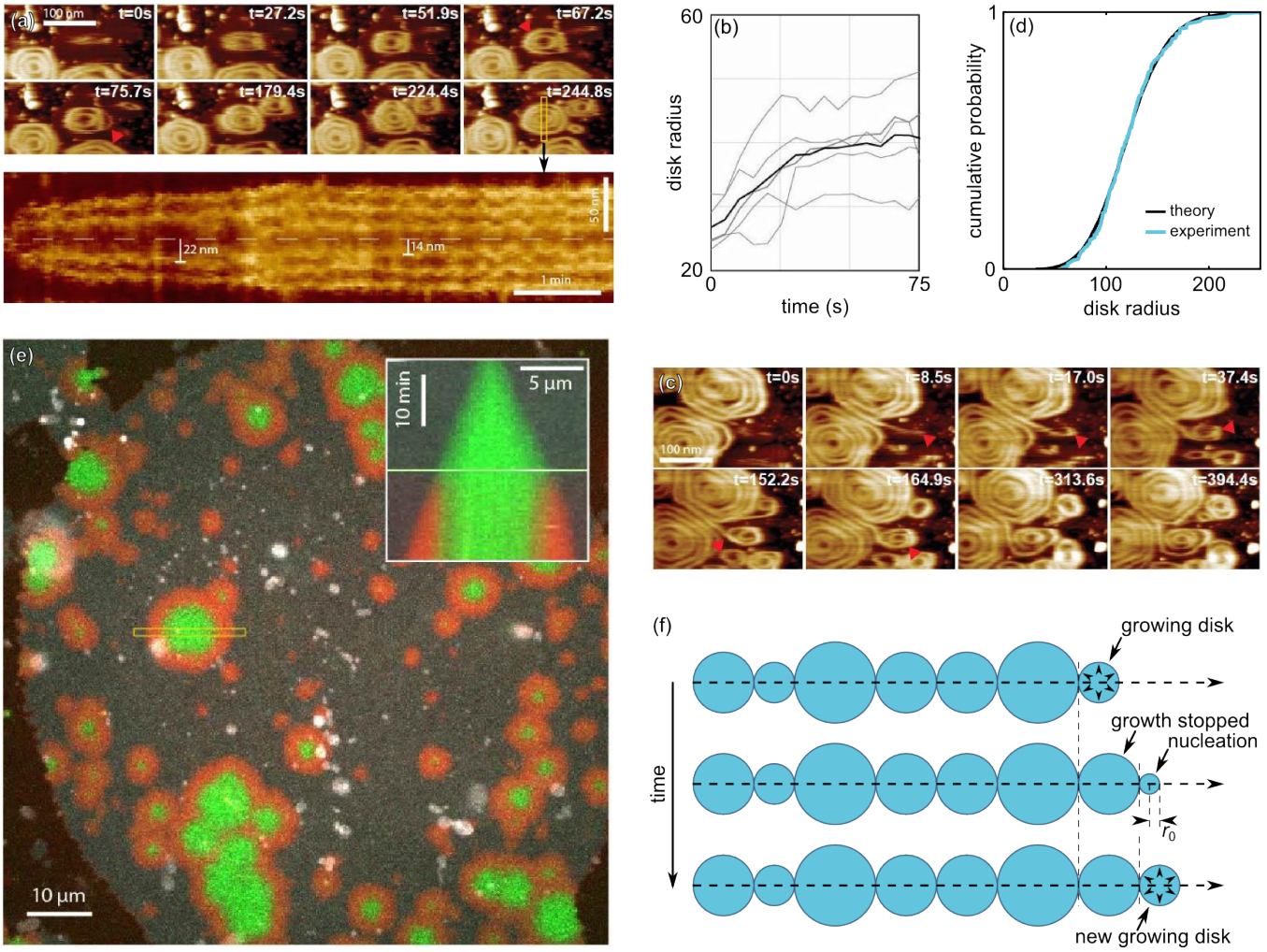

Figure 3.8: ESCRT-III assembly process. (a) High-speed AFM time-lapse sequence of an isolated Snf7 spiral with equatorial kymograph (*yellow rectangle*) of the same growing spiral shown below. Note that the radius of the innermost filament shrinks from 22 nm to 14 nm as indicated. This is consistent with the model of Sec. 3.3.1, according to which the spiral's inner filaments acquire an increasing strain during spiral growth. (b) Outer radius as a function of time of five growing Snf7 spirals followed by high-speed AFM (*thin lines*) and average (*thick line*). (c) High-speed AFM time-lapse sequence showing the stages of the heterogeneous nucleation of a new Snf7 spiral from pre-existing ones as indicated by *arrowheads*: a filament protrudes from a spiral ($t = 8.5\,\mathrm{s}$), curls from its tip ($t = 17.0\,\mathrm{s}$), and forms a small spiral ($t = 37.4\,\mathrm{s}$). Also indicated are the growth of a second turn in the new spiral ($t = 152.2\,\mathrm{s}$) and internal filament rearrangements during the growth again consistent with the model of Sec. 3.3.1 ($t = 164.9\,\mathrm{s}$). (d) Cumulative distribution of spiral sizes (*blue*) fitted with our theoretical model (*black*) for $r_0 = 25\,\mathrm{nm}$. (e) Large-scale growth of fluorescent Snf7 patches on supported membranes. The color of the fluorescent Snf7 is changed from green to red halfway through the experiment, highlighting the fact that the Snf7 patches grow from the rim. *Inset:* kymograph of the region encased in the *yellow box*, showing the constant radial growth velocity of the patch. (f) Illustration of our simplified one-dimensional patch growth model.

by impenetrable hard disks deposited on a two-dimensional surface representing a small (micron-sized) piece of membrane. A few disks with radius r_0 are initially present, corresponding to initial homogeneous nucleation event. Homogeneous nucleation is then neglected during the rest of the dynamics (an assumption justified by a more complete analysis). New disks are thus generated only by heterogeneous nucleation, following which their area grows with a speed w as described by Eq. (3.13). As the mean spacing between filaments within a spiral is $b = 17\,\mathrm{nm}$, this corresponds to a filament growth speed of $v = w/b = 2.1\,\mathrm{nm}\cdot\mathrm{s}^{-1}$. As the Snf7 spiral grows, its perimeter increases, offering an increasing number of potential spiral nucleation sites. We model this by stochastic nucleation of new disks with radius r_0 at a rate $\lambda\mathcal{P}$, where $\mathcal{P}$ denotes the total perimeter of the existing disks, and λ a constant spiral nucleation rate per unit length. Nucleation is prevented if the new disk location is already occupied by an existing disk, implying a decreasing total nucleation rate as the membrane becomes more and more crowded. For computational simplicity, we tackle the model in a mean-field approximation where these excluded volume interactions are computed while ignoring positional correlations between disks. Solving through numerical methods, we find a final distribution of disk sizes with only one adjustable parameter λ. Fitting $\lambda = 8.2\times10^3\,\mathrm{m}\cdot\mathrm{s}^{-1}$ yields excellent agreement with the observed distribution as shown in Fig. 3.8(d).

To further assess the validity of our model, we monitor the assembly of Snf7 spirals on much larger, $10\,\mu$m length scales through fluorescence microscopy. As shown in Fig. 3.8(e), an initial homogeneous nucleation event gives birth to a radially expanding patch of Snf7 composed of many spirals with expansion velocity ranging from $V = 1\,\mathrm{nm}\cdot\mathrm{s}^{-1}$ to $6\,\mathrm{nm}\cdot\mathrm{s}^{-1}$ experimentally. This value is consistent with the nucleation-and-growth model described above, which becomes clear when considering the approximate one-dimensional model illustrated in Fig. 3.8(f). In the model, Snf7 disks are arranged in a line and are in contact with their nearest neighbors. Disks are added sequentially from left to right. Due to crowding, only the rightmost disk is able to grow and nucleate new disks. The rightmost disk grows according to Eq. (3.13) and stochastically nucleates a new disk with radius r_0 to its right with a rate $2\pi r\lambda$ proportional to its perimeter. Following this nucleation event, the growth of the old disk stops and the new disk starts growing according to Eq. (3.13). As a result, the position of the edge of the disk-covered region of space moves with an average velocity

$$V = \frac{2w}{3\pi r_0}\frac{3e^{\tilde\lambda} + E_{2/3}(\tilde\lambda)}{E_{1/3}(\tilde\lambda)} \underset{\tilde\lambda\ll1}{\sim} \frac{\Gamma(1/6)}{3^{1/3}\pi^{5/6}} w^{2/3}\lambda^{1/3} \simeq 0.6\,\mathrm{nm}\cdot\mathrm{s}^{-1}, \tag{3.14}$$

where $\tilde\lambda = 4\pi^2 r_0^3\lambda/3w \simeq 0.021$, $E_n(z)$ is the exponential integral function and $\Gamma(z)$ the gamma function [102]. The numerical value in Eq. (3.14) stems from the parameter values determined in the previous paragraphs. Despite the obvious geometrical inaccuracies of the one-dimensional model, this value is in order-of-magnitude agreement with the measured value, and thus further validates our model of the ESCRT-III assembly kinetics.

3.3.3 Stress build-up in the Snf7 spiral and membrane deformation

Beyond the simple rigid-disk growth process described above, the experiments of Sec. 3.3.2 allow us to investigate the elastic deformation of ESCRT-III spirals and are thus crucial to assess the mechanism of Sec. 3.3.1. Indeed, in practice the process described above leaves small gaps between the disks that are too small to be filled by newly nucleated disks. As the existing disks continue to grow, they fill the voids by deforming into a more polygonal profile, as shown in Fig. 3.9(a). In this deformed state, elastic energy is stored in the (deformed) disks as determined by the competition between filament elasticity and the two-dimensional pressure associated with Snf7 polymerization. This pressure is equal to the chemical potential per unit surface μ defined in Eq. (3.12), and we independently measure $\mu = 3.1\times10^{-4}\,\mathrm{N}\cdot\mathrm{m}^{-1}$ using a pipette setup similar to that of Fig. 3.3(d). We also quantity filament elasticity by measuring the persistence length of individual fluctuating Snf7 filaments by AFM, finding $\ell_p = 260\,\mathrm{nm}$. In the following, we use these values to estimate the amount of elastic energy accumulated in the Snf7 disks.

To investigate the deformation of a spiral, we model the Snf7-covered membrane as a triangular lattice of identical deformed disks as shown in Fig. 3.9(b). As Snf7 polymerization progresses, the resting area A' of the protein coat becomes larger than its actual area A, which cannot increase due to the inextensibility

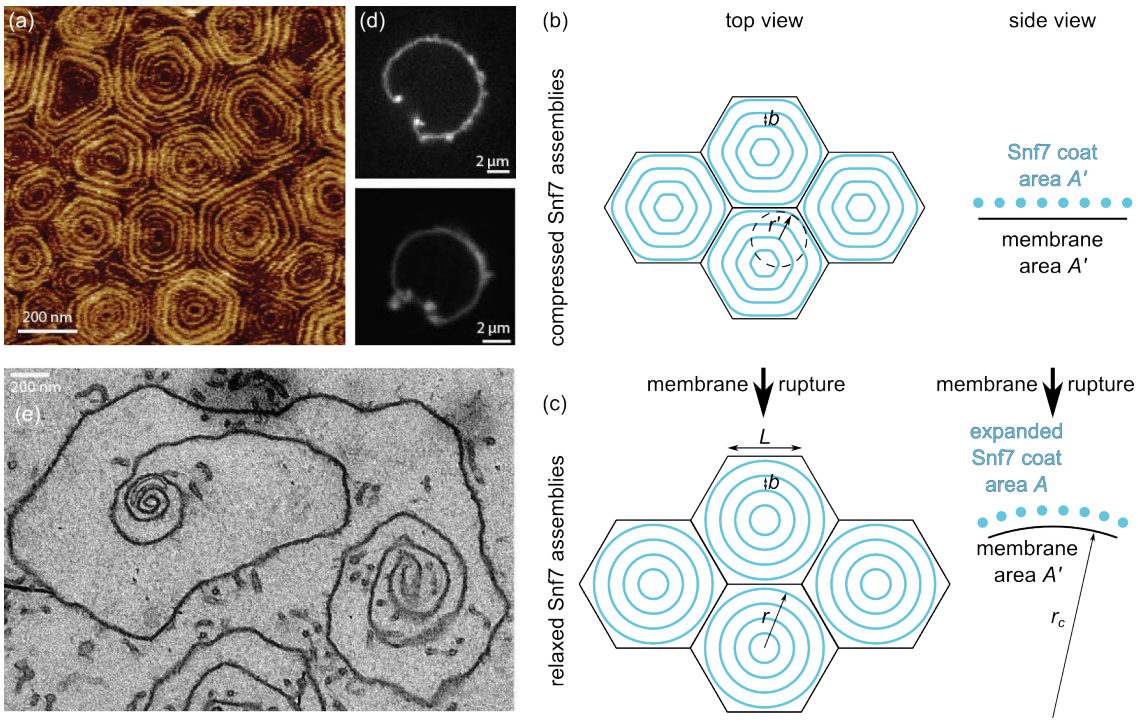

Figure 3.9: Snf7 filament compression drives membrane deformation. (a) AFM topographic image of a Snf7 coat, showing deformed spirals with an overall polygonal shape. (b) Model of these deformed spirals. (c) Allowing the Snf7 coat to expand laterally restores the circular shape of the spirals, and induces an overall curvature r_c^{-1} of the membrane-protein sandwich (*right*). (d) Confocal sections of burst Snf7-coated vesicles. Fluorescence is more intense at the rim of the pore. (e) Electron microscopy thin section image of a Snf7-coated vesicle displaying visible curling of the membrane rim.

of the underlying membrane. This mismatch between the resting areas of the membrane and the protein coat implies that the resulting assembly has a non-vanishing spontaneous curvature, which we quantify thanks to an elastic model of the Snf7 filament deformations. Approximating the shape of the filaments pictured in Fig. 3.9(b) as a succession of straight and constant-curvature sections and imposing mechanical equilibrium, we predict a typical radius of curvature of the bent sections of the filaments in agreement with experimental observations:

$$r' \underset{\mu \gg \mu^*,\, r \gg b}{\sim} r\sqrt{\mu^*/\mu} = 47\,\mathrm{nm}, \tag{3.15}$$

where

$$\mu^* = \frac{1}{2-\pi/\sqrt{3}} \frac{k_B T \ell_p}{r^2 b} \ln(r/b) \simeq 4.1 \times 10^{-5}\,\mathrm{N\cdot m^{-1}} \tag{3.16}$$

is the typical surface pressure needed to induce substantial compression of the disks. Here $b \simeq 16\,\mathrm{nm}$ is the spacing between concentric filaments as illustrated in Fig. 3.9(b). Note that the expression Eq. (3.15) is valid in the experimentally relevant limits $\mu \gg \mu^*$, $r \gg b$. Combining this equation with geometrical considerations, we find

$$A'/A = \left[\frac{\pi}{2\sqrt{3}} + \left(1 - \frac{\pi}{2\sqrt{3}}\right)\frac{r'}{r}\right]^2. \tag{3.17}$$

A spectacular proof of the accumulation of elastic energy in the Snf7 disks is obtained when the vesicle ruptures spontaneously over hours. Instead of bursting, the membrane shrinks from the rim of the pore towards the opposite side of the vesicle as shown in Fig. 3.9(d). This process is known as curling, and is generically observed when a vesicle with spontaneous curvature is ruptured. Examples include polymersomes [103] and the bursting of red blood cells [104]. In these cases, the innermost radius of the curled membrane seen in Fig. 3.9(e) reflects the spontaneous curvature of the membrane due to this area

difference. Our model predicts that this difference reads

$$r_c = \frac{d}{2} \times \frac{1 + A'/A}{1 - A'/A} \simeq 37\,\mathrm{nm}, \tag{3.18}$$

where the numerical value was obtained using Eqs. (3.15) and (3.17). This prediction is in very good agreement with the experimentally observed value $39 \pm 6\,\mathrm{nm}$, thus validating our model of elastic stress accumulation in ESCRT-III spirals.

3.3.4 Outlook

Understanding the mechanics of ESCRT-III deformation requires a grasp of three processes: its assembly at the membrane, its membrane-deforming action, and the separation of the resulting vesicle from the main membrane. Here we offer theoretical models for the first (Sec. 3.3.2) and second (Sec. 3.3.1) steps, and use further modeling and experiments to verify their fundamental assumptions (Secs. 3.3.2 and 3.3.3, respectively). We moreover independently determine all of our models' parameters. Further combining our determination of the Snf7 persistence length with information about the diameter of ESCRT-III-dressed tubes *in vivo* (see Ref. [105]), we also predict where the *in vivo* ESCRT-III assemblies of Ref. [96] lie in the phase diagram of Fig. 3.7(d). We find that our data is compatible with metastable ESCRT-III disks, accounting for the observation of both flat and tubulated structures in this study.

These numerical values moreover allow us to compute the amount of elastic energy accumulated as the Snf7 filaments become compressed in Fig. 3.9(b). We find $\Delta E \simeq 170 k_B T$, larger than the $4\pi\kappa \simeq 160 k_B T$ bending energy cost of creating a spherical vesicle. This order of magnitude as well as our successful prediction of the ESCRT-III-induced vesicle curvature without any adjustable parameters suggest that the lateral compression of Snf7 filaments due to their own polymerization energy is indeed sufficient to induce membrane deformation, as hypothesized in the model presented in Sec. 3.3.1. Note that our tests involve a slightly different geometry that the model: in the former, Snf7 compression arises from lateral contact between independent spirals whereas the latter deals with interactions within a single spiral, a more physiologically relevant situation. Nevertheless, we do expect the energies involved in both cases to be of the same order, providing support for our "spring-release" membrane deformation mechanism.

Beyond membrane deformation, a quantitatively validated, predictive model of how ESCRT-III severs the membrane to produce vesicles is currently lacking despite the existence of several competing qualitative models [106, 107, 108]. Several pieces of evidence point to a fairly different mechanism than the one at work in dynamin. First, membrane fission appears to require the intervention of ATPase Vps4 [97], which is associated with the disassembly of ESCRT-III filament rather then with a conformational change [99]. Second, the resulting vesicles appear clear of ESCRT-III associated proteins [108], in contrast with the continued association of clathrin coats with endocytosed vesicles. We believe that a more thorough understanding of this process will be brought about through continued interactions between modeling and quantitative experiments.

Reference: *Relaxation of loaded ESCRT-III spiral springs drives membrane deformation.*
Nicolas Chiaruttini, Lorena Redondo-Morata, Adai Colom, Frédéric Humbert, **Martin Lenz***, Simon Scheuring*, Aurélien Roux* (*equal contributions), *submitted* (2015)

Chapter 4

Research project: Dissecting active matter

Summary

Biological motion and forces originate from mechanically active proteins operating at the nanometer scale. These individual active elements interact through the surrounding cellular medium, collectively generating structures spanning tens of micrometers whose mechanical properties are perfectly tuned to their fundamentally out-of-equilibrium biological function. While both individual proteins and the resulting cellular behaviors are well characterized, understanding the relationship between these two scales remains a major challenge in both physics and cell biology.

We will bridge this gap through **multiscale models of the emergence of *active* material properties in the experimentally well-characterized actin cytoskeleton**. We will thus investigate unexplored, **strongly interacting nonequilibrium regimes**. We will develop a complete framework for cytoskeletal activity by separately studying all three fundamental processes driving it out of equilibrium: actin filament assembly and disassembly, force exertion by branched actin networks, and the action of molecular motors. We will then recombine these approaches into a unified understanding of complex cell motility processes.

To tackle the cytoskeleton's disordered geometry and many-body interactions, we will design new nonequilibrium self-consistent methods in statistical mechanics and elasticity theory. Our findings will be validated through simulations and close experimental collaborations.

Our work will break new ground in both biology and physics. In the context of biology, it will establish a new framework to understand how the cell controls its architecture and mechanics through biochemical regulation. On the physics side, it will set up new paradigms for the emergence of original out-of-equilibrium collective behaviors in an experimentally well-characterized system, addressing the foundations of existing macroscopic "active matter" approaches.

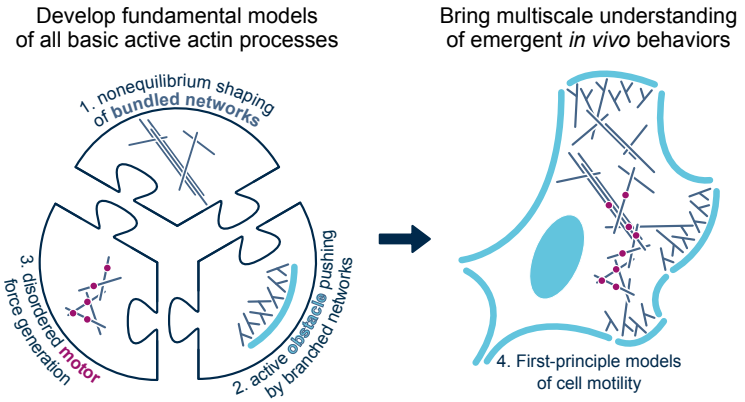

4.1 Introduction

Motion and forces are essential characteristics of living systems, present all the way from the level of the organism to its subcellular constituents. Virtually all of these biological forces are produced at the nanometer scale, where energy-consuming protein machines self-assemble and exert forces, thus maintaining biological matter out of equilibrium. This endows living matter with unusual collective properties, including spontaneous motion, pattern formation and the active generation of forces, through which it performs biological functions as diverse as cell motility, embryonic morphogenesis or muscle contraction. However, **how the cell controls the emergence of these *collective* behaviors through the regulation of its *individual* constituents is poorly understood**.

To the physicist, these out-of-equilibrium materials are part of a new class that has come to be known as "active matter" [36], and whose best characterized instance is the actin cytoskeleton. The actin cytoskeleton is a network of the semiflexible biopolymer actin that underlies the mechanical properties of virtually all animal cells. It performs many of the cell's mechanical duties, including motility and division. Its dysfunctions cause cancer, vascular disease and chronic inflammation. *In vivo*, it assumes a large range of microscopic organizations, from dense amorphous actin networks to well-organized bundled arrays. These versatile assemblies are very dynamic, and constantly evolve under the influence of nonequilibrium actin polymerization and depolymerization as well as of force-exerting molecular motors.

Due to the complexity of their internal interactions, **there is no consensus model for active actin networks**. The most widely used framework, termed "active gels" [9], adopts a radically phenomenological approach, describing the cytoskeleton as a viscoelastic continuum without reference to its microscopic constituents. Despite having yielded valuable insights into cellular behaviors, active gel theories involve many adjustable parameters and rest on some questionable assumptions, not least the one that the cytoskeleton is only weakly out of equilibrium. In contrast, at the single-filament level, the worm-like chain model is regarded as an excellent description of actin's mechanics. Large-scale fiber network models based on it have recently made substantial progress, but are still largely limited to *equilibrium* (passive) situations [43]. Moreover, these models do not describe the effect of the entanglements and internal stresses that arise in a dynamic, self-renewing cytoskeleton. **A new framework to understand the effects of microscopic interactions within the dense, nonequilibrium cytoskeleton is thus needed to overcome the limitations of current approaches.**

In this project, we will develop rigorous, generic models to bridge the gap between the microscopic and the macroscopic in the actin cytoskeleton. Our approach crucially relies on recent experimental findings as well as on close collaborations with leading experimental groups pioneering novel *in vitro* techniques. We will focus on the $\approx$ 10-100 nm length scale where cytoskeletal constituents interact, and where they can be described as simple geometrical objects. In contrast with many previous approaches, **our models will fully recognize that emergence in the cytoskeleton can only be understood by *simultaneously* taking into account its strongly interacting and fundamentally out-of-equilibrium character**. We will approach these systems by developing new nonequilibrium self-consistent methods in statistical mechanics and elasticity theory supported by numerical simulations.

4.2 Research goals

Rather than focusing on individual cellular processes as in most of the existing literature, **we will aim for a *systematic* understanding of cytoskeletal activity**, with a focus on understanding robust, universal scaling laws. We will thus separately study all three processes known to drive the cytoskeleton out of equilibrium: actin's polymerization-depolymerization dynamics, which shapes the morphology of crosslinked actin networks (Sec. 4.2.1), the force-exerting growth of branched actin networks against an obstacle (Sec. 4.2.2), and the exertion of internal forces by myosin molecular motors (Sec. 4.2.3). Finally, we will demonstrate the power of this systematic approach by applying our new insights to outstanding problems in cell motility, where the interplay between different types of cytoskeletal activity plays a crucial role (Sec. 4.2.4).

4.2.1 Shaping of crosslinked networks by actin polymerization dynamics

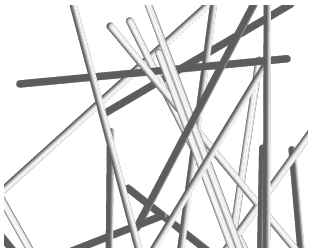

Actively polymerizing actin gets stuck in nonequilibrium, entangled states.

Rationale. Networks of actin filaments held together by crosslinking proteins largely dictate passive and active cytoskeletal mechanics. Their properties are determined by their microstructure, ranging from isotropic gels of single filaments to networks of thick, crosslinked actin bundles. These are commonly regarded as equilibrium structures [109] controlled by the crosslinkers' nature and concentration [110]. In a recent article, we have however shown through experiments and theory that this morphology is determined by its assembly kinetics, demonstrating a nonequilibrium structure [111] displaying slow glassy relaxation [112]. Based on these results, we will **propose a new paradigm for crosslinked actin structure based on kinetically trapped nonequilibrium states** actively driven by actin's nonequilibrium polymerization and disassembly. This represents a **fundamental change of perspective on cytoskeletal organization in the absence of molecular motors**. In collaboration with the Gardel lab (U. of Chicago, experiments), we will use the original properties (see, *e.g.*, Ref. [113]) of the resulting **glassy active matter phases** to explain cytoskeletal behaviors.

Approach. Our previous work and preliminary simulations suggest that bundled networks are stabilized through steric constraints (entanglements) between their filaments. We will thus first describe the network microstructure through a minimal model of diffusing, entangling impenetrable rods. If two filaments touch, they align and coalesce into a bundle unless this coalescence is prevented by entanglements. Inspired by *in vitro* experiments, rods will grow over time, inducing increasing entanglements and kinetic arrest. We will predict the amount of bundling in the final state through nonequilibrium kinetic theory and simulations.

In vivo, filaments are actively being severed and depolymerized concomitant with their polymerization. We will extend our approaches to assess how entanglements are resolved by these nonequilibrium processes, and will predict the phase behavior of the resulting steady states. We will investigate the influence of filament flexibility, as well as of varying concentrations of realistic crosslinkers imposing specific relative filament orientations. Our new concepts will thus allow us to revisit the substantial experimental literature on the subject, and to characterize the buildup of internal network stresses. We will finally use these results to investigate the viscoelastic response of bundled networks, focusing on how the cell regulates the filaments' dynamics to fluidize the network and keep a tight leash on liquid *vs.* solid behavior in the cytoskeleton.

Goal 1 targets (†indicates experimental verification provided through collaborations)

1.1 Predictions for the microstructure (mesh size...) of irreversibly growing bundled networks†

1.2 Phase diagram for the nonequilibrium steady-states of bundled networks of dynamic filaments†

1.3 Predictions for the influence of filament growth conditions on linear and nonlinear viscoelasticity†

4.2.2 Adaptive mechanics of branched networks

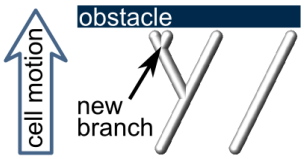

Branched networks grow and branch against obstacles.

Rationale. When exerting a force against an obstacle, typically the cell membrane, actin filaments polymerize into specialized branched networks. There, new branches are nucleated off the side of existing filaments in contact with the obstacle (see illustration) by protein complex Arp2/3. Our current understanding of the resulting force relies on variants of the celebrated "ratchet model" [114], which describes how filaments touching the obstacle push it away as actin monomers are added at their tips. This mechanism requires the underlying branched network to orient its filaments towards the obstacle while resisting a mechanical load. Internal filament deformations *within* the network crucially influence these processes [115], inextricably linking the rigidity of branched network to their force-exerting ability [116]. Unfortunately, current models [43] dramatically fail at accounting for this rigidity, predicting that branched networks are infinitely

soft ("isostatic") due to the small coordination of their branching points. As a result, they predict very large, uncoordinated ("nonaffine") bending displacements of the filaments inside these networks.

To explain this crucial component of cell motility, **we will develop a new approach to fiber network elasticity. Our formalism will be based on the mechanical constraints induced by entanglement resulting from large nonaffine internal deformations** (see illustration). This will enable us to elucidate the biochemical regulation of actin force generation in collaboration with the du Roure/Heuvingh group at ESPCI [117].

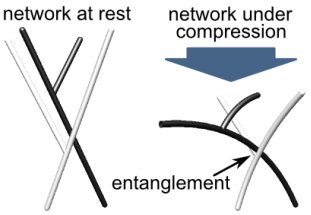

Branched network bend and entangle under stress.

Approach. We will first design lattice-based growth models to determine to what extent neighboring actin "trees" intertwine depending on their growth parameters (branching rate, *etc.*)—a crucial factor in determining the density of potential entanglements. Interestingly, an analogy with branching random walks suggests a possible phase transition causing a dramatic increase in entanglement density. Using these results, we will model the passive linear and nonlinear elasticity of branched networks as a prerequisite for our subsequent nonequilibrium investigations. We will develop a self-consistent ("effective medium") formalism to determine the number of entanglements within the network, and verify its results with simulations. The basic notion of our approach is that denser entanglements yield a stiffer network, hence limiting the amount of internal nonaffine filament deformations and thus the formation of further entanglements.

As branched networks grow against an obstacle, their internal structure and mechanics are influenced by the applied stress, which tends to bend growing filaments, thus generating entanglements and internal network stresses. It is also finely controlled by biochemical regulators, many of which bind to the actin in a way dependent on its mechanical state. Using our sound mechanical framework, we will model this interplay between mechanics and biochemistry to predict the networks stiffness, nonlinear elastic behavior and force-velocity relationship as a function of its history of applied stress and biochemical environment. Additionally, we will consider viscoelastic and plastic deformations of the branched networks under applied force due to branch detachment as studied macroscopically by the ESPCI and Théry (Hôpital Saint-Louis) groups, and at the single-molecule level by the Romet-Lemonne group (Institut Jacques Monod).

Goal 2 targets ([†]indicates experimental verification provided through collaborations)

2.1 Numerically validated predictions for the entanglement topology of neighboring trees

2.2 Predictions for the linear and nonlinear elasticity of passive branched networks[†]

2.3 Prediction of the effect of actin growth regulators on viscoelasticity and force-velocity relationship[†]

4.2.3 Macroscopic stress generation by motors

Rationale. Perhaps the best-known role of the actin cytoskeleton is to exert contractile forces that make the cell deform and move. These forces are generated by microscopic myosin molecular motors, which induce a translating motion of actin filaments. While this simple mechanism straightforwardly generates macroscopic contraction in our highly organized striated muscle, we have recently shown that it is not sufficient to describe contraction in disordered one-dimensional actomyosin bundles. In these more complex geometries, motors exert both pulling and pushing forces [118], and we have shown through theory and experiments that actin's nonlinear elastic response is required to favor the latter over the former [119, 22, 26]. **By questioning the universality of the muscle-like contraction paradigm, our novel approach has started to redefine a cornerstone of our understanding of cell motility.** Turning to biologically relevant two- and three-dimensional actin networks, we have shown in two studies that *local* violations of the pushing/pulling symmetry can induce *some* contraction in linear elastic media [48, 120]. These single-motor effects are

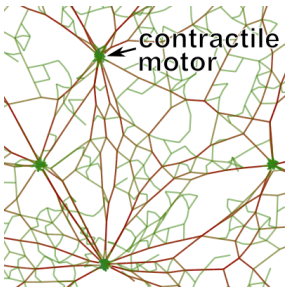

Actin deformation and flows enhance force generation by motors.

however small compared to the forces measured in real networks. **We hypothesize that this difference is due to cooperative, self-organizing effects in realistic nonlinear, viscoelastic networks**. We will investigate these effects with the Murrell group (Yale University), whose micromechanical experiments allow unprecedented control and resolution over two-dimensional actomyosin contractility.

Approach. We will first investigate the role of nonlinear network elasticity in enhancing microscopic motor forces in discrete fiber networks, as well as through continuum nonlinear elasticity theory. These highly localized motor forces will induce localized nonlinear deformations resulting in a strong stress amplification as studied in our current work. The extent of this amplification will depend on the size of the nonlinearly deformed region, which increases with increasing motor force. This effect will be particularly dramatic in recently studied, cytoskeleton-like, strongly nonlinear depleted fiber networks [43]. The preliminary data presented in Sec. 2.7 demonstrates that much remains to be understood in this ares, including the enhanced dipole amplification presented in Fig. 2.13(c), (d), (f) and (g). We believe that such effects could account for cooperative stress generation as observed in experiments [121].

As actin networks reorganize viscoelastically over minutes, we will investigate whether such rearrangements might generically cause disordered actomyosin assemblies to self-organize into more efficient contractility-generating structures. We will supplement our model with transient crosslinkers as well as use continuum hydrodynamic descriptions to describe the possible alignment of actin filaments around discrete motors into striated-muscle-like structures. We will also investigate to what extent viscous dissipation within the network might screen the motor forces and yield inefficient force transmission. These findings will be further validated through detailed numerical models using existing simulation packages. Our analysis will not only uncover the microscopic origin of cytoskeletal contractility, but will also help identify the optimal network parameters depending on the intended function, thus shedding light on the *raison d'être* of the wide variety of actomyosin contractile structures found *in vivo*.

Goal 3 targets ([†]indicates experimental verification provided through collaborations)

3.1 Prediction of the amplitude of contractile strains and stresses depending on network parameters[†]

3.2 New mechanisms for actomyosin self-organization predicting the time evolution of contractility[†]

4.2.4 Putting the pieces back together: applications to cell motility

Rationale. As our individual models for the three fundamental active mechanisms take shape, we will reach for our most ambitious objective. After taking the cytoskeleton apart in goals 1-3, we will put the pieces back together and analyze real cellular processes from our well-established first principles. Beyond the new insights it will yield into crucial *in vivo* behaviors, this goal has the potential to **validate our approach as the first universal, predictive description of the actin cytoskeleton**.

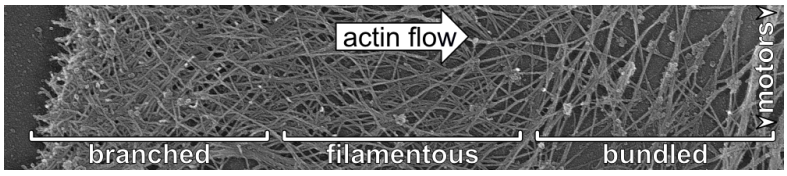

Actin microstructure is dynamically modulated during cell motility (fibroblast, adapted from http://www.cellimagelibrary.org/images/24801).

Approach. We will start our analysis with the well-studied example of the cell front, which combines crosslinked and branched networks with motor activity and for which ample biochemical information is available. Going beyond coarse-grained models [9], we will quantitatively account for the dynamic modulation of the actin microstructure at the cell front (see illustration). We will next investigate whether our models explain recently observed oscillatory behaviors proposed to play a role in navigating complex environments [122]. Finally, we will connect the microscopic with the macroscopic to predict the effect of the plethora of well-characterized biochemical factors affecting motile cell morphology and function [123].

Beyond this well-known type of motility, cells under physiological conditions adapt to their environment, and recent studies reveal that their whole motile machinery undergoes dramatic reconfigurations in response to purely physical stimuli. These include geometrical changes in their adhesive environment (Théry

lab, Hôpital Saint-Louis) or the mere compression between glass plates, which causes the cell to switch between three very different, well-defined morphologies [124]. We will investigate the mechanisms through which physical stresses induce local reconfigurations of the actomyosin cytoskeleton causing these global transitions, as well as physical reasons for the existence of well-separated, distinct cytoskeletal steady-states.

Goal 4 targets

4.1 Comparisons of our models with published data on cell front morphology, mechanics and dynamics

4.2 Putative models of the transitions between different types of motility under spatial constraints

4.3 Novelty and impact

While the cytoskeleton has attracted much theoretical attention both at the microscopic and the macroscopic level, understanding the relationship between the two scales has remained a challenging task. While strongly interacting [125] and nonequilibrium [21] regimes have previously been modeled separately, recent experimental advances have revealed that the interplay between these two aspects is crucial in shaping the collective behaviors of the actin cytoskeleton. To understand these biologically relevant properties, **we will for the first time design and solve generic models combining strong interactions between cytoskeletal components with their nonequilibrium, self-driven physics.**

Our generic models will open new avenues for research in **biophysics** as a reliable base for descriptions of a plethora of specific cellular processes in the spirit of goal 4.2.4. **Soft matter physics** will benefit from our critical insights into the foundations of active matter theories, as well as from opportunities to better connect these models to experiments. Our study of entanglements in extremely low-coordinated *branched* networks will prompt further investigations of their role in widely studied *crosslinked* networks, where large internal filament displacements are also expected in many regimes. Our understanding of active glassy fiber networks trapped out of equilibrium by entanglements will be applicable beyond living systems, and **nonequilibrium statistical mechanics** could draw inspiration from these general concepts and study them in simplified frameworks. We will enable **Fundamental biology** to identify situations where cellular behaviors differ from our simple physical predictions, which would point towards undiscovered biochemical regulators of cellular function. Finally, the spectacular control achieved over actin by experimentalists has made it into an **engineering** tool for biomimetic materials and microfabrication [126]. A better theoretical understanding of the determinants of its microstructure will help improve our control of these processes.

Appendix A

Publications

Stars denote equal contributions. Click on the title of published articles to access them online.

22. *Fiber networks amplify active stress*
P. Ronceray, C. Broedersz, **M. Lenz**
arXiv:1507.05873 and submitted (2015)

21. *Compression of ESCRT-III spiral springs drives membrane deformation*
N. Chiaruttini, L. Redondo-Morata, A. Colom, F. Humbert, **M. Lenz***, S. Scheuring*, A. Roux*
Cell, in press (2015)

20. *Forcing cells into shape: the mechanics of actomyosin contractility*
M. Murrell, P. Oakes, **M. Lenz**, M. L. Gardel *Nat. Rev. Mol. Cell Biol.* **16**, 486 (2015)

19. *A balance between membrane elasticity and polymerization energy sets the shape of clathrin coats*
M. Saleem, S. Morlot, A. Hohendahl, J. Manzi, **M. Lenz***, A. Roux* *Nat. Commun.* **6**, 6249 (2015)

18. *Connecting local active forces to macroscopic stress in elastic media*
P. Ronceray, **M. Lenz** *Soft Matter* **11**, 1597 (2015)

17. *Geometrical origins of contractility in disordered actomyosin networks*
M. Lenz *Phys. Rev. X* **4**, 041002 (2014)

16. *Dynamical tunneling with Bose-Einstein condensates in magnetic microtraps*
M. Lenz, S. Wüster, C. J. Vale, N. R. Heckenberg, H. Rubinsztein-Dunlop, C. A. Holmes, G. J. Milburn, M. J. Davis *Phys. Rev. A* **88**, 013635 (2013)

15. *Thick filament length and isoform composition determine properties of self-organized contractile units in actomyosin bundles*
T. Thoresen, **M. Lenz**, M. L. Gardel *Biophys. J.* **104**, 655 (2013)

14. *Membrane shape at the edge of the dynamin helix sets location and duration of fission*
S. Morlot, V. Galli, M. Klein, N. Chiaruttini, J. Manzi, F. Humbert, L. Dinis, **M. Lenz**, G. Cappello, A. Roux *Cell* **151**, 619 (2012)

13. *Assembly kinetics determine the architecture of α-actinin-crosslinked F-actin networks*
T. T. Falzone, **M. Lenz**, D. R. Kovar, M. L. Gardel *Nat. Commun.* **3**, 861 (2012)

12. *Contractile units in disordered actomyosin bundles arise from F-actin buckling*
M. Lenz, T. Thoresen, M. L. Gardel, A. R. Dinner *Phys. Rev. Lett.* **108**, 238107 (2012)

11. *Requirements for contractility in disordered cytoskeletal bundles*
M. Lenz, M. L. Gardel, A. R. Dinner *New J. Phys.* **14**, 033037 (2012)

10. *Reconstitution of contractile actomyosin bundles*
T. Thoresen, **M. Lenz**, M. L. Gardel *Biophys. J.* **100**, 2698 (2011)

9. *Deformation of dynamin helices damped by membrane friction*
S. Morlot*, **M. Lenz***, J. Prost, J.-F. Joanny, A. Roux *Biophys. J.* **99**, 3580 (2010)

8. *Polymerization of human MIP-1 chemokines (CCL3 and CCL4) and clearance of MIP-1 by human insulin degrading enzyme*
   M. Ren*, Q. Guo*, L. Guo, **M. Lenz**, H. Xu, A. R. Dinner, A. B. Schilling, W.-J. Tang
   EMBO. J. **29**, 3952 (2010)

7. *Actin cross-linkers and the shape of stereocilia*
   M. Lenz, J. Prost, J.-F. Joanny *Biophys. J.* **99**, 2423 (2010)

6. *A reaction-diffusion model of the cadherin-catenin system: A possible mechanism for contact inhibition and implications for tumorigenesis*
   M. Basan, T. Idema, **M. Lenz**, J.-F. Joanny, T. Risler *Biophys. J.* **98**, 2770 (2010)

5. *Membrane curvature controls dynamin polymerization*
   A. Roux, G. Koster, **M. Lenz**, B. Sorre, J.-B. Manneville, P. Nassoy, P. Bassereau
   Proc. Natl. Acad. Sci. U.S.A. **107**, 4141 (2010)

4. *Mechanical requirements for membrane fission: common facts from various examples*
   M. Lenz, S. Morlot, A. Roux *FEBS Lett.* **583**, 3839 (2009)

3. *ATP-Dependent nonequilibrium mechanics of red blood cells*
   T. Betz, **M. Lenz**, J.-F. Joanny, C. Sykes *Proc. Natl. Acad. Sci. U.S.A.* **106**, 15320 (2009)

2. *Membrane buckling induced by curved filaments*
   M. Lenz, D. J. G. Crow, J.-F. Joanny *Phys. Rev. Lett.* **103**, 038101 (2009)

1. *Mechanochemical action of the dynamin protein*
   M. Lenz, J. Prost, J.-F. Joanny *Phys. Rev. E* **78**, 011911 (2008)

References

[1] Andrew G Szent-Györgyi. The early history of the biochemistry of muscle contraction. *J. Gen. Physiol.*, 123(6):631–641, June 2004.

[2] F S Fay, K Fujiwara, D D Rees, and K E Fogarty. Distribution of alpha-actinin in single isolated smooth muscle cells. *J. Cell Biol.*, 96(3):783–795, March 1983.

[3] L P Cramer, M Siebert, and T J Mitchison. Identification of novel graded polarity actin filament bundles in locomoting heart fibroblasts: implications for the generation of motile force. *J. Cell Biol.*, 136(6):1287–1305, March 1997.

[4] Ana Carvalho, Arshad Desai, and Karen Oegema. Structural memory in the contractile ring makes the duration of cytokinesis independent of cell size. *Cell*, 137(5):926–937, May 2009.

[5] Ohad Medalia, Igor Weber, Achilleas S Frangakis, Daniela Nicastro, Gunther Gerisch, and Wolfgang Baumeister. Macromolecular architecture in eukaryotic cells visualized by cryoelectron tomography. *Science*, 298(5596):1209–1213, November 2002.

[6] A B Verkhovsky, T M Svitkina, and G G Borisy. Myosin II filament assemblies in the active lamella of fibroblasts: their morphogenesis and role in the formation of actin filament bundles. *J. Cell Biol.*, 131(4):989–1002, November 1995.

[7] Yvonne Aratyn-Schaus, Patrick W. Oakes, and Margaret L. Gardel. Dynamic and structural signatures of lamellar actomyosin force generation. *Mol. Biol. Cell*, 22(8):1330–1339, April 2011.

[8] Guillaume Salbreux, Guillaume Charras, and Ewa Paluch. Actin cortex mechanics and cellular morphogenesis. *Trends Cell Biol.*, 22(10):536–545, August 2012.

[9] Jean-François Joanny and Jacques Prost. Active gels as a description of the actin-myosin cytoskeleton. *HFSP J.*, 3(2):94–104, September 2009.

[10] F C MacKintosh and A J Levine. Nonequilibrium mechanics and dynamics of motor-activated gels. *Phys. Rev. Lett.*, 100(1):018104, January 2008.

[11] Shigehiko Yumura. Myosin ii dynamics and cortical flow during contractile ring formation in dictyostelium cells. *J. Cell Biol.*, 154(1):137–146, July 2001.

[12] Andrew G. Clark, Kai Dierkes, and Ewa K. Paluch. Monitoring actin cortex thickness in live cells. *Biophys. J.*, 105(3):570–580, August 2013.

[13] Erin L. Barnhart, Kun-Chun Lee, Kinneret Keren, Alex Mogilner, and Julie A. Theriot. An adhesion-dependent switch between mechanisms that determine motile cell shape. *PLoS Biol.*, 9(5):e1001059, May 2011.

[14] Theo Odijk. Stiff chains and filaments under tension. *Macromolecules*, 28(20):7016–7018, September 1995.

[15] Barak Gilboa, David Gillo, Oded Farago, and Anne Bernheim-Groswasser. Bidirectional cooperative motion of myosin-II motors on actin tracks with randomly alternating polarities. *Soft Matter*, 5(11):2223–2231, June 2009.

[16] Michael Murrell and Margaret L Gardel. F-actin buckling coordinates contractility and severing in a biomimetic actomyosin cortex. *Proc. Natl. Acad. Sci. U.S.A.*, 109(51):20820–20825, December 2012.

[17] Marina Soares e Silva, Martin Depken, Björn Stuhrmann, Marijn Korsten, Fred C Mackintosh, and Gijsje H Koenderink. Active multistage coarsening of actin networks driven by myosin motors. *Proc. Natl. Acad. Sci. U.S.A.*, 108(23):9408–9413, June 2011.

[18] Poul M Bendix, Gijsje H Koenderink, Damien Cuvelier, Zvonimir Dogic, Bernard N Koeleman, William M Brieher, Christine M Field, L Mahadevan, and David A Weitz. A quantitative analysis of contractility in active cytoskeletal protein networks. *Biophys. J.*, 94(8):3126–3136, April 2008.

[19] Daisuke Mizuno, Catherine Tardin, C F Schmidt, and F C Mackintosh. Nonequilibrium mechanics of active cytoskeletal networks. *Science*, 315(5810):370–373, January 2007.

[20] Nilushi L Dasanayake, Paul J Michalski, and Anders E Carlsson. General mechanism of actomyosin contractility. *Phys. Rev. Lett.*, 107(11):118101, September 2011.

[21] T B Liverpool and M C Marchetti. Bridging the microscopic and the hydrodynamic in active filament solutions. *Europhys. Lett.*, 69(5):846–852, March 2005.

[22] Todd Thoresen, Martin Lenz, and Margaret L Gardel. Reconstitution of contractile actomyosin

bundles. *Biophys. J.*, 100(11):2698–2705, June 2011.

[23] Anne-Cécile Reymann, Rajaa Boujemaa-Paterski, Jean-Louis Martiel, Christophe Guérin, Wenxiang Cao, Harvey F Chin, Enrique M De La Cruz, Manuel Théry, and Laurent Blanchoin. Actin network architecture can determine myosin motor activity. *Science*, 336(6086):1310–1314, June 2012.

[24] K Kruse and F Jülicher. Actively contracting bundles of polar filaments. *Phys. Rev. Lett.*, 85(8):1778–1781, August 2000.

[25] Karsten Kruse and Franck Jülicher. Self-organization and mechanical properties of active filament bundles. *Phys. Rev. E*, 67(5):051913, May 2003.

[26] Todd Thoresen, Martin Lenz, and Margaret L Gardel. Thick filament regulation of contractility in self-organized actomyosin bundles. *Biophys. J.*, 104(3):655–665, 2013.

[27] H Kojima, A Ishijima, and T Yanagida. Direct measurement of stiffness of single actin filaments with and without tropomyosin by in vitro nanomanipulation. *Proc. Natl. Acad. Sci. U.S.A.*, 91(26):12962–12966, December 1994.

[28] Steven S Rosenfeld, Jun Xing, Li-Qiong Chen, and H Lee Sweeney. Myosin IIB is unconventionally conventional. *J. Biol. Chem.*, 278(30):27449–27455, July 2003.

[29] Gijsje H Koenderink, Zvonimir Dogic, Fumihiko Nakamura, Poul M Bendix, Frederick C MacKintosh, John H Hartwig, Thomas P Stossel, and David A Weitz. An active biopolymer network controlled by molecular motors. *Proc. Natl. Acad. Sci. U.S.A.*, 106(36):15192–7, September 2009.

[30] Jose Alvarado, Michael Sheinman, Abhinav Sharma, Fred C. MacKintosh, and Gijsje H. Koenderink. Molecular motors robustly drive active gels to a critically connected state. *Nat. Phys.*, 9:591, August 2013.

[31] H. Isambert and A. C. Maggs. Dynamics and rheology of actin solutions. *Macromolecules*, 29(3):1036–1040, January 1996.

[32] Wilbur A. Lam, Ovijit Chaudhuri, Ailey Crow, Kevin D. Webster, Tai-De Li, Ashley Kita, James Huang, and Daniel A. Fletcher. Mechanics and contraction dynamics of single platelets and implications for clot stiffening. *Nat. Mater.*, 10:61–66, 2011.

[33] H P Ehrlich. Wound closure: evidence of cooperation between fibroblasts and collagen matrix. *Eye*, 2:149–157, 1988.

[34] Chauying J. Jen and Larry V. Mclntire. The structural properties and contractile force of a clot. *Cell Motil.*, 2:445–455, 1982.

[35] F. Jülicher, K. Kruse, J. Prost, and J.-F. Joanny. Active behavior of the cytoskeleton. *Phys. Rep.-Rev. Sec. Phys. Lett.*, 449(1–3):3–28, September 2007.

[36] M. C. Marchetti, J. F. Joanny, S. Ramaswamy, T. B. Liverpool, J. Prost, Madan Rao, and R. Aditi Simha. Hydrodynamics of soft active matter. *Rev. Mod. Phys.*, 85:1143, July 2013.

[37] Yair Shokef and Samuel A. Safran. Scaling laws for the response of nonlinear elastic media with implications for cell mechanics. *Phys. Rev. Lett.*, 108(17):178103, April 2012.

[38] D A Head, A J Levine, and F C MacKintosh. Mechanical response of semiflexible networks to localized perturbations. *Phys. Rev. E*, 72(6):061914, 2005.

[39] Rose Loughlin, Rebecca Heal, and François Nd́ĺec. A computational model predicts xenopus meiotic spindle organization. *J. Cell Biol.*, 191(137):1239–1249, December 2010.

[40] Erdinc Atilgan, Denis Wirtz, and Sean X Sun. Morphology of the lamellipodium and organization of actin filaments at the leading edge of crawling cells. *Biophys. J.*, 89(5):3589–3602, 2005.

[41] Jie Zhu and Alex Mogilner. Mesoscopic model of actin-based propulsion. *PLoS Comput. Biol.*, 8(11):e1002764, November 2012.

[42] Ulrich S. Schwarz and Samuel A. Safran. Physics of adherent cells. *Rev. Mod. Phys.*, 85(3):1327, August 2013.

[43] C P Broedersz and F C MacKintosh. Modeling semiflexible polymer networks. *Rev. Mod. Phys.*, 86:995–1036, July-September 2014.

[44] Nilushi L Dasanayake and Anders E Carlsson. Stress generation by myosin minifilaments in actin bundles. *Phys. Biol.*, 10(3):036006, June 2013.

[45] A E Carlsson. Contractile stress generation by actomyosin gels. *Phys. Rev. E*, 74(5 Pt 1):051912, Nov 2006.

[46] C P Broedersz and F C MacKintosh. Molecular motors stiffen non-affine semiflexible polymer networks. *Soft Matter*, 7:3186–3191, 2011.

[47] A. S. Abhilash, Brendon M. Baker, Britta Trappmann, Christopher S. Chen, and Vivek B. Shenoy. Remodeling of fibrous extracellular matrices by contractile cells: Predictions from discrete fiber network simulations. *Biophys. J.*, 107(8):1829–1840, October 2014.

[48] Pierre Ronceray and Martin Lenz. Connecting local active forces to macroscopic stress in elastic media. *Soft Matter*, 11(8):1597–1605, January 2015.

[49] J. D. Eshelby. The continuum theory of lattice defects. *Solid State Phys.*, 3:79–144, 1956.

[50] M. Sheinman, C. P. Broedersz, and F. C. MacKintosh. Nonlinear effective-medium theory of disordered spring networks. *Phys. Rev. E*, 85(2):021801, February 2012.

[51] Chase P Broedersz, Xiaoming Mao, Tom C Luben-

sky, and Frederick C MacKintosh. Criticality and isostaticity in fibre networks. *Nat. Phys.*, 7:983–988, December 2011.

[52] C. P. Broedersz, M. Sheinman, and F. C. MacKintosh. Filament-length-controlled elasticity in 3D fiber networks. *Phys. Rev. Lett.*, 108(7):078102, February 2012.

[53] Cornelis Storm, Jennifer J Pastore, F C MacKintosh, T C Lubensky, and Paul A Janmey. Nonlinear elasticity in biological gels. *Nature*, 435(7039):191–4, May 2005.

[54] Joël Lemière, Matthias Bussonnier, Timo Betz, Cécile Sykes, and Kevin Carvalho. Cell-sized liposome doublets reveal active cortical tension build up. manuscript currently in review and attached to this submission for the reviewers' consideration, April 2015.

[55] Kimihide Hayakawa, Hitoshi Tatsumi, and Masahiro Sokabe. Actin filaments function as a tension sensor by tension-dependent binding of cofilin to the filament. *J. Cell Biol.*, 195(5):721–727, November 2011.

[56] W Helfrich. Elastic properties of lipid bilayers: theory and possible experiments. *Z. Naturforsch. (C)*, 28(11):693–703, November-December 1973.

[57] Martin Lenz, Sandrine Morlot, and Aurélien Roux. Mechanical requirements for membrane fission: Common facts from various examples. *FEBS Lett.*, 583(23):3839–3846, December 2009.

[58] Toku Kanaseki and Ken Kadota. The "vesicle in a basket": A morphological study of the coated vesicle isolated from the nerve endings of the guinea pig brain, with special reference to the mechanism of membrane movements. *J. Cell Biol.*, 42(1):202–220, July 1969.

[59] B M Pearse. Clathrin: a unique protein associated with intracellular transfer of membrane by coated vesicles. *Proc. Natl. Acad. Sci. U.S.A.*, 73(4):1255–1259, April 1976.

[60] R A Crowther and B M Pearse. Assembly and packing of clathrin into coats. *J. Cell Biol.*, 91(3):790–797, February 1981.

[61] Tom Kirchhausen. Bending membranes. *Nat. Cell Biol.*, 14:906–908, 2012.

[62] Marijn G. J. Ford, Barbara M. F. Pearse, Matthew K. Higgins, Yvonne Vallis, David J. Owen, Adele Gibson, Colin R. Hopkins, Philip R. Evans, and Harvey T. McMahon. Simultaneous binding of ptdins(4,5)p2 and clathrin by ap180 in the nucleation of clathrin lattices on membranes. *Science*, 291(5506):1051–1055, February 2001.

[63] Philip N. Dannhauser and Ernst J. Ungewickell. Reconstitution of clathrin-coated bud and vesicle formation with minimal components. *Nat. Cell Biol.*, 14:634–639, 2012.

[64] Jeanne C. Stachowiak, Eva M. Schmid, Christopher J. Ryan, Hyoung Sook Ann, Darryl Y. Sasaki, Michael B. Sherman, Phillip L. Geissler, Daniel A. Fletcher, and Carl C. Hayden. Membrane bending by protein–protein crowding. *Nat. Cell Biol.*, 14:944–949, 2012.

[65] Alexander Fotin, Yifan Cheng, Piotr Sliz, Nikolaus Grigorieff, Stephen C Harrison, Tomas Kirchhausen, and Thomas Walz. Molecular model for a complete clathrin lattice from electron cryomicroscopy. *Nature*, 432(7017):573–579, December 2004.

[66] Corinne J. Smith, Nikolaus Grigorieff, and Barbara M.F. Pearse. Clathrin coats at 21 å resolution: a cellular assembly designed to recycle multiple membrane receptors. *EMBO J.*, 17(17):4943–4953, September 1998.

[67] G P Vigers, R A Crowther, and B M Pearse. Three-dimensional structure of clathrin cages in ice. *EMBO J.*, 5(3):529–534, March 1986.

[68] J. Heuser and T. Kirchhausen. Deep-etch views of clathrin assemblies. *Journal of Ultrastructure Research*, 92(1–2):1–27, July-August 1985.

[69] Harvey T. McMahon and Emmanuel Boucrot. Molecular mechanism and physiological functions of clathrin-mediated endocytosis. *Nat. Rev. Mol. Cell Biol.*, 12:517–533, August 2011.

[70] Jez G Carlton and Juan Martin-Serrano. Parallels between cytokinesis and retroviral budding: a role for the ESCRT machinery. *Science*, 316(5833):1908–1912, June 2007.

[71] Albert J Jin, Kondury Prasad, Paul D Smith, Eileen M Lafer, and Ralph Nossal. Measuring the elasticity of clathrin-coated vesicles via atomic force microscopy. *Biophys. J.*, 90(9):3333–3344, May 2006.

[72] Sandrine Morlot, Valentina Galli, Marius Klein, Nicolas Chiaruttini, John Manzi, Frédéric Humbert, Luìs Dinìs, Martin Lenz, Giovanni Cappello, and Aurélien Roux. Membrane shape at the edge of the dynamin helix sets location and duration of the fission reaction. *Cell*, 151(3):619–629, October 2012.

[73] Benoît Sorre, Andrew Callan-Jones, John Manzi, Bruno Goud, Jacques Prost, Patricia Bassereau, and Aurĺien Roux. Nature of curvature coupling of amphiphysin with membranes depends on its bound density. *Proc. Natl. Acad. Sci. U.S.A.*, 3(109):173–178, January 2011.

[74] Evan Evans, Howard Bowman, Andrew Leung, David Needham, and David Tirrell. Biomembrane templates for nanoscale conduits and networks. *Science*, 273(5277):933–935, 1996.

[75] Tobias Baumgart, Samuel T. Hess, and Watt W. Webb. Imaging coexisting fluid domains in biomembrane models coupling curvature and line tension. *Nature*, 425(6960):821–824, 2003.

[76] Ralph Nossal. Energetics of clathrin basket assem-

bly. *Traffic*, 2(2):138–147, January 2001.

[77] Wouter K. den Otter and Wim J. Briels. The generation of curved clathrin coats from flat plaques. *Traffic*, 12(10):1407–1416, October 2011.

[78] Soheil Aghamohammadzadeh and Kathryn R. Ayscough. Differential requirements for actin during yeast and mammalian endocytosis. *Nature Cell Biology*, 11:1039 – 1042, 2009.

[79] Steeve Boulant, Comert Kural, Jean-Christophe Zeeh, Florent Ubelmann, and Tomas Kirchhausen. Actin dynamics counteract membrane tension during clathrin-mediated endocytosis. *Nat. Cell Biol.*, 13:1124–1131, 2011.

[80] H Y Naim, D T Dodds, C B Brewer, and M G Roth. Apical and basolateral coated pits of mdck cells differ in their rates of maturation into coated vesicles, but not in the ability to distinguish between mutant hemagglutinin proteins with different internalization signals. *J. Cell Biol.*, 129(5):1241–1250, 1995.

[81] Gerrit J K Praefcke and Harvey T McMahon. The dynamin superfamily: universal membrane tubulation and fission molecules? *Nat. Rev. Mol. Cell Biol.*, 5(2):133–147, February 2004.

[82] Sanja Sever, Hanna Damke, and Sandra L Schmid. Garrotes, springs, ratchets, and whips: Putting dynamin models to the test. *Traffic (Oxford, U. K.)*, 1(5):385–392, May 2000.

[83] Yen-Ju Chen, Peijun Zhang, Edward H Egelman, and Jenny E Hinshaw. The stalk region of dynamin drives the constriction of dynamin tubes. *Nat. Struct. Mol. Biol.*, 11(6):574–575, June 2004.

[84] Dganit Danino, Kwan-Hoon Moon, and Jenny E Hinshaw. Rapid constriction of lipid bilayers by the mechanochemical enzyme dynamin. *J. Struct. Biol.*, 147(3):259–267, May 2004.

[85] Joshua S. Chappie, Jason A. Mears, Shunming Fang, Marilyn Leonard, Sandra L. Schmid, Ronald A. Milligan, Jenny E. Hinshaw, and Fred Dyda. A pseudoatomic model of the dynamin polymer identifies a hydrolysis-dependent powerstroke. *Cell*, 147(1):209–222, September 2011.

[86] Katja Faelber, York Posor, Song Gao, Martin Held, Yvette Roske, Dennis Schulze, Volker Haucke, Frank Noé, and Oliver Daumke. Crystal structure of nucleotide-free dynamin. *Nature*, 477:556–560, September 2011.

[87] Marijn G. J. Ford, Simon Jenni, and Jodi Nunnari. The crystal structure of dynamin. *Nature*, 477(7366):561–566, September 2011.

[88] Sharon M Sweitzer and Jenny E Hinshaw. Dynamin undergoes a GTP-dependent conformational change causing vesiculation. *Cell*, 93(6):1021–1029, June 1998.

[89] Aurélien Roux, Katherine Uyhazi, Adam Frost, and Pietro De Camilli. GTP-dependent twisting of dynamin implicates constriction and tension in membrane fission. *Nature*, 441:528–531, May 2006.

[90] J E Hinshaw and S L Schmid. Dynamin self-assembles into rings suggesting a mechanism for coated vesicle budding. *Nature*, 374(6518):190–192, 1995.

[91] K Takei, P S McPherson, S L Schmid, and P De Camilli. Tubular membrane invaginations coated by dynamin rings are induced by GTP-γS in nerve terminals. *Nature*, 374(6518):186–190, March 1995.

[92] Yonathan Kozlovsky and Michael M Kozlov. Membrane fission: model for intermediate structures. *Biophys. J.*, 85(1):85–96, July 2003.

[93] Martin Lenz, Jacques Prost, and Jean-François Joanny. Mechanochemical action of the dynamin protein. *Phys. Rev. E*, 78(1):011911, July 2008.

[94] Sandrine Morlot, Martin Lenz, Jacques Prost, Jean-François Joanny, and Aurélien Roux. Deformation of dynamin helices damped by membrane friction. *Biophys. J.*, 99(11):3580–3588, December 2010.

[95] Thomas Slagsvold, Krupa Pattni, Lene Malerod, and Harald Stenmark. Endosomal and non-endosomal functions of ESCRT proteins. *Trends Cell Biol.*, 16(6):317–326, June 2006.

[96] Phyllis I Hanson, Robyn Roth, Yuan Lin, and John E Heuser. Plasma membrane deformation by circular arrays of ESCRT-III protein filaments. *J. Cell Biol.*, 180(2):389–402, January 2008.

[97] Yuan Lin, Lisa A Kimpler, Teresa V Naismith, Joshua M Lauer, and Phyllis I Hanson. Interaction of the mammalian endosomal sorting complex required for transport (ESCRT) III protein hSnf7-1 with itself, membranes, and the AAA+ ATPase SKD1. *J. Biol. Chem.*, 280(13):12799–12809, April 2005.

[98] Sara Ghazi-Tabatabai, Suraj Saksena, Judith M Short, Ajaybabu V Pobbati, Dmitry B Veprintsev, R Anthony Crowther, Scott D Emr, Edward H Egelman, and Roger L Williams. Structure and disassembly of filaments formed by the ESCRT-III subunit Vps24. *Structure*, 16(9):1345–1356, 2008.

[99] Suman Lata, Guy Schoehn, Ankur Jain, Ricardo Pires, Jacob Piehler, Heinrich G Gottlinger, and Winfried Weissenhorn. Helical structures of ESCRT-III are disassembled by VPS4. *Science*, 321(5894):1354–1357, September 2008.

[100] Thomas Wollert, Christian Wunder, Jennifer Lippincott-Schwartz, and James H Hurley. Membrane scission by the ESCRT-III complex. *Nature*, 458(7235):172–177, March 2009.

[101] Shujuan Pan, Ruoning Wang, Xi Zhou, Guangan He, John Koomen, Ryuji Kobayashi, Le Sun, Joe Corvera, Gary E Gallick, and Jian Kuang. Involvement of the conserved adaptor protein alix in actin cytoskeleton assembly. *J. Biol. Chem.*,

281(45):34640–34650, November 2006.

[102] Milton Abramowitz and Irene A Stegun. *Handbook of Mathematical Functions*. Number 55 in Applied Mathematics Series. National Bureau of Standards, Washington D. C., 1972.

[103] Elyes Mabrouk, Damien Cuvelier, Françoise Brochard-Wyart, Pierre Nassoy, , and Min-Hui Li. Bursting of sensitive polymersomes induced by curling. *Proc. Natl. Acad. Sci. U.S.A.*, 106(18):7294–7298, May 2009.

[104] Andrew Callan-Jones, Octavio Eduardo Albarran Arriagada, Gladys Massiera, Vladimir Lorman, and Manouk Abkarian. Red blood cell membrane dynamics during malaria parasite egress. *Biophys. J.*, 103(12):2475–2483, 2012.

[105] Martin Lenz, Daniel J G Crow, and Jean-François Joanny. Membrane buckling induced by curved filaments. *Phys. Rev. Lett.*, 103(3):038101, July 2009.

[106] Suraj Saksena, Ji Sun, Tony Chu, and Scott D Emr. ESCRTing proteins in the endocytic pathway. *Trends Biochem. Sci.*, 32(12):561–573, December 2007.

[107] Gur Fabrikant, Suman Lata, James D Riches, John A G Briggs, Winfried Weissenhorn, and Michael M Kozlov. Computational model of membrane fission catalyzed by ESCRT-III. *PLoS Comput. Biol.*, 5(11):e1000575, November 2009. submitted to PNAS, sent to Jean-François by Kozlov.

[108] Anil G Cashikar, Soomin Shim, Robyn Roth, Michael R Maldazys, John E Heuser, and Phyllis I Hanson. Structure of cellular ESCRT-III spirals and their relationship to HIV budding. *eLife*, 3:e02184, 2014.

[109] C. J. Cyron, K. W. Müller, K. M. Schmoller, A. R. Bausch, W. A. Wall, and R. F. Bruinsma. Equilibrium phase diagram of semi-flexible polymer networks with linkers. *Europhys. Lett.*, 102(3):38003, May 2013.

[110] O. Lieleg, K. M. Schmoller, M. M. A. E. Claessens, and A. R. Bausch. Cytoskeletal polymer networks: Viscoelastic properties are determined by the microscopic interaction potential of cross-links. *Biophys. J.*, 96(11):4725–4732, June 2009.

[111] Tobias T Falzone, Martin Lenz, David R Kovar, and Margaret L Gardel. Assembly kinetics determine the architecture of α-actinin crosslinked F-actin networks. *Nat. Commun.*, 3:861, May 2012.

[112] O Lieleg, J Kayser, G Brambilla, L Cipelletti, and A R Bausch. Slow dynamics and internal stress relaxation in bundled cytoskeletal networks. *Nat. Mater.*, 10:236–242, January 2011.

[113] Yaouen Fily and M. Cristina Marchetti. Athermal phase separation of self-propelled particles with no alignment. *Phys. Rev. Lett.*, 108(23):235702, June 2012.

[114] C S Peskin, G M Odell, and G F Oster. Cellular motions and thermal fluctuations: the brownian ratchet. *Biophys. J.*, 65(1):316–324, July 1993.

[115] Viviana I. Risca, Evan B. Wang, Ovijit Chaudhuri, Jia Jun Chia, Phillip L. Geissler, and Daniel A. Fletcher. Actin filament curvature biases branching direction. *Proc. Natl. Acad. Sci. U.S.A.*, 109(8):2913–2918, February 2012.

[116] Sapun H. Parekh, Ovijit Chaudhuri, Julie A. Theriot, and Daniel A. Fletcher. Loading history determines the velocity of actin-network growth. *Nat. Cell Biol.*, 7(12):1219–1223, December 2005.

[117] Thomas Pujol, Olivia du Roure, Marc Fermigier, and Julien Heuvingh. Impact of branching on the elasticity of actin networks. *Proc. Natl. Acad. Sci. U.S.A.*, 109(26):10364–10369, June 2012.

[118] Martin Lenz, Margaret L Gardel, and Aaron R Dinner. Requirements for contractility in disordered cytoskeletal bundles. *New J. Phys.*, 14:033037, March 2012.

[119] Martin Lenz, Todd Thoresen, Margaret L Gardel, and Aaron R Dinner. Contractile units in disordered actomyosin bundles arise from F-actin buckling. *Phys. Rev. Lett.*, 108(23):238107, June 2012.

[120] Martin Lenz. Geometrical origins of contractility in disordered actomyosin networks. *Phys. Rev. X*, 4:041002, October 2014.

[121] Michael Murrell and Margaret L. Gardel. Actomyosin sliding is attenuated in contractile biomimetic cortices. *Mol. Biol. Cell*, 25(12):1845–1853, June 2014.

[122] Jun Allard and Alex Mogilner. Traveling waves in actin dynamics and cell motility. *Curr. Opin. Cell Biol.*, 25(1):107–115, February 2013.

[123] Chris Bakal, John Aach, George Church, and Norbert Perrimon. Quantitative morphological signatures define local signaling networks regulating cell morphology. *Science*, 316(5832):1753–1756, June 2007.

[124] Yan-Jun Liu, Maël Le Berre, Franziska Lautenschlaeger, Paolo Maiuri, Andrew Callan-Jones, Melina Heuzé, Tohru Takaki, Raphaël Voituriez, and Matthieu Piel. Confinement and low adhesion induce fast amoeboid migration of slow mesenchymal cells. to appear in Cell, 2015.

[125] David C. Morse. Tube diameter in tightly entangled solutions of semiflexible polymers. *Phys. Rev. E*, 63(3):031502, February 2001.

[126] Rémi Galland, Patrick Leduc, Christophe Guérin, David Peyrade, Laurent Blanchoin, and Manuel Théry. Fabrication of three-dimensional electrical connections by means of directed actin self-organization. *Nat. Mater.*, 12:416—421, 2013.